

TEMPERATURE INSENSITIVE
MICROMECHANICAL RESONATORS

A DISSERTATION
SUBMITTED TO THE DEPARTMENT OF MECHANICAL
ENGINEERING
AND THE COMMITTEE ON GRADUATE STUDIES
OF STANFORD UNIVERSITY
IN PARTIAL FULFILLMENT OF THE REQUIREMENTS
FOR THE DEGREE OF
DOCTOR OF PHILOSOPHY

Renata Melamud
December 2008

UMI Number: 3343929

Copyright 2009 by
Melamud, Renata

All rights reserved.

INFORMATION TO USERS

The quality of this reproduction is dependent upon the quality of the copy submitted. Broken or indistinct print, colored or poor quality illustrations and photographs, print bleed-through, substandard margins, and improper alignment can adversely affect reproduction.

In the unlikely event that the author did not send a complete manuscript and there are missing pages, these will be noted. Also, if unauthorized copyright material had to be removed, a note will indicate the deletion.

UMI[®]

UMI Microform 3343929

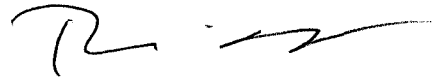
Copyright 2009 by ProQuest LLC.

All rights reserved. This microform edition is protected against unauthorized copying under Title 17, United States Code.

ProQuest LLC
789 E. Eisenhower Parkway
PO Box 1346
Ann Arbor, MI 48106-1346

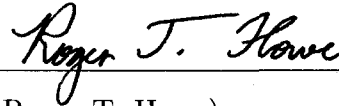
© Copyright by Renata Melamud 2009
All Rights Reserved

I certify that I have read this dissertation and that, in my opinion, it is fully adequate in scope and quality as a dissertation for the degree of Doctor of Philosophy.



(Dr. Thomas W. Kenny) Principal Adviser

I certify that I have read this dissertation and that, in my opinion, it is fully adequate in scope and quality as a dissertation for the degree of Doctor of Philosophy.



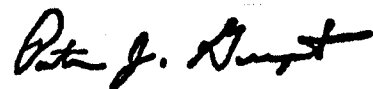
(Dr. Roger T. Howe)

I certify that I have read this dissertation and that, in my opinion, it is fully adequate in scope and quality as a dissertation for the degree of Doctor of Philosophy.



(Dr. William D. Nix)

Approved for the University Committee on Graduate Studies.



Abstract

Most modern electronic devices use frequency references based on quartz crystal resonators. The difficulty of miniaturizing the current quartz crystal resonator packaging technology provides an opportunity for wafer-scale packaged micromachined silicon resonators to displace quartz resonators in the frequency reference market. However, the higher temperature sensitivity of silicon's material properties results in higher frequency variation and limits the ability of silicon resonators to compete with quartz crystal resonators in ultra-high precision applications.

This work describes the design, fabrication, and testing of composite resonators made of single-crystal silicon with a silicon dioxide coating. These composite resonators have a temperature sensitivity of less than 4% that of silicon resonators, which makes them comparable to quartz crystal resonators. Single-anchor, flexural-mode, double-ended tuning fork and ring resonators were designed in the frequency range of 700 kHz to 1.3 MHz. The minimum achieved frequency variation is 200 parts per million over a -55 C to 125 C temperature range. The frequency-temperature behavior of the resonator exhibits quadratic temperature dependence with a quadratic temperature coefficient of frequency of approximately -20 parts per billion per C² and a turnover temperature at which the linear temperature coefficient of frequency is zero. This turnover temperature can be designed to be at the desired operating temperature, which is attractive for integration with active temperature compensation methods.

The resonators were packaged using a modified wafer-scale encapsulation technology described by Candler et al. in *Journal of Microelectromechanical Systems* in

2006. The MEMS-first, CMOS-compatible, packaging process yields composite resonators which are hermetically sealed in a low pressure environment, exhibit quality factors of 10,000 to 30,000, and have sub-mm³ volume. In conjunction with active temperature compensation schemes, this technology enables silicon-based frequency references to meet the needs of high-precision applications at a reduced size.

Acknowledgement

This work would not be possible without the mentors, advisers, colleagues, friends, and family who have shaped my path to Stanford and through Stanford and have been instrumental in supporting me.

It is without a doubt that the one person who has had the greatest and most lasting influence on my career path is my adviser, Tom Kenny. He often gave me all the answers and the freedom to figure them out on my own. Thanks for being as good a role model and mentor as anyone could hope for [20, 34].

The Kenny Group is a diverse group of people who really brought a sense of community and camaraderie to the lab. I am thankful to Rob Candler, Matt Hopcroft, Bongsang Kim, Saurabh Chandorkar, and Manu Agarwal for their guidance in all things academic and life which has been and will be indispensable to me. I would also like to thank my labmates Matt Messana, Andrew Graham, Hyungkyu Lee, Chandra Mohan Jha, Jim Salvia, Gaurav Bahl, Violet Qu, Shingo Yoneoka, Wes Smith, Shasha Wang, Yoonjin Won and Kevin Lohner. Their insights, discussions, feedback, and willingness to help has been invaluable. Thank you to Ginel Hill and Dan Soto for providing an escape from resonators.

I've benefited greatly from the spirit of collaboration at Stanford which breaks the boundaries of labs, departments, and schools. The friendliness and helpfulness of the students of Dr. Roger Howe's group and Dr. Beth Pruitt's group have enriched my experiences. In particular I would like to thank Mariam Ziaei-Moayyed, J Provine, Roozbeh Parsa, and Alvin Barlian who have often gone out of their way to lend a helping hand.

My interaction with the employees of Bosch Palo Alto Research and Technology

Center (RTC) and SiTime from my first year at Stanford gave me a sense of purpose in the pursuit of this research. Marcus Lutz and Aaron Partridge of Bosch and SiTime provided extraordinary technical expertise and embodied and inspired the spirit of entrepreneurship. A big thank you to Gary Yama of Bosch RTC for his guidance in all things fabrication related and his remarkable generosity and help.

This dissertation would not be possible without the Stanford Nanofabrication Facility and the support and kindness of its staff members and lab members. The fabrication process was helped along by many late night rescues by Eric Perozziello and Robin King. I owe them many favors.

I greatly appreciate the feedback and insights given by Dr. Roger Howe and Dr. William Nix. Thank you to Dr. Reinhold Dauskardt and Dr. Kurt Petersen for their encouragement and feedback during the defense of this dissertation. A special thanks to Dr. Beth Pruitt who has been like a second adviser to me since my first year at Stanford.

This dissertation was preformed with the help of two funding sources. The DARPA Harsh Environment Robust Micromechanical Technology (HERMIT) program provided the motivation and funding for this research. I have also been generously supported by the Gabilan Stanford Graduate Fellowship without which I would not have had a chance to explore.

I am fortunate to have had and made many wonderful friends during my time at Stanford. Each is remarkable and inspiring in their own right. They have made my time at Stanford an unforgettable experience. Thank you to Julie, Keenan, Shad, Nicola, Rohit, Anu, Megan, Morgan, Al, Carla, Dave, Adam, Martin, and Kindra. Thank you to Eric for ensuring early onset of smile wrinkles and a glimpse of a wonderful life.

There are no words to describe my deep gratitude for the love and support of my Mom, Dad, and brother. They have given me the strength to believe in myself and the encouragement to achieve my dreams. This dissertation is dedicated to my parents, none of this would have been possible without their courage.

Contents

Abstract	iv
Acknowledgement	vi
1 Resonators and Frequency References	1
1.1 Quartz Crystal Resonators	3
1.2 Silicon MEMS Resonators	6
1.2.1 Electrostatically Actuated Resonators	8
1.2.2 Frequency	13
1.2.3 Quality Factor	18
1.3 Temperature Dependence	19
1.3.1 Generalized Temperature Coefficients	19
1.3.2 Temperature Coefficients of Frequency	20
1.4 Temperature Compensation Techniques	24
1.4.1 Passive Stress Compensation	25
1.4.2 Passive and Active Electrostatic Compensation	26
1.4.3 Active Oven-Control	26
1.4.4 Active Circuit Compensation	27
1.5 Contribution and Organization	28
2 Theory of Composite Resonators	30
2.1 Frequency Models of Composite Resonators	32
2.1.1 Flexural Modes	32
2.1.2 Extensional Modes	38

2.2	Temperature Dependence of Si-SiO ₂ Composite Resonator	38
2.3	Summary	41
3	Fabrication of Composite Resonators	44
3.1	Thin-film Epi-Seal Fabrication of Composite Resonators	45
3.1.1	Pre-processing	45
3.1.2	Device Definition	46
3.1.3	Sacrificial Release Layer	48
3.1.4	Epitaxial Silicon Encapsulation	49
3.1.5	Device Release	51
3.1.6	Composite Formation	54
3.1.7	Epitaxial Sealing	56
3.1.8	Electrical Interconnect Formation	58
3.1.9	Post-processing	61
3.2	Fabrication Challenges	63
3.2.1	Membrane Buckling	63
3.2.2	Wafer Bowing	65
3.2.3	Plasma Etch Damage and Other Consequences	66
3.2.4	Composite Dimension Uncertainty	69
3.2.5	Miscellaneous Problems and Discussion	70
3.3	Summary	71
3.4	Acknowledgements	71
4	“Zero-TCf” Resonators	72
4.1	Composite Resonator Testing	73
4.2	“Zero-TCf” Composite Resonators	76
4.2.1	Double Ended Tuning Fork Resonators	77
4.2.2	Flexural Mode Ring Resonator	83
4.2.3	Extensional Mode Ring Resonator	86
4.3	Higher Order Effects	88
4.3.1	Effect of Linear Material Properties	90

4.3.2	Effect of Nonlinear Material Properties	92
4.3.3	Extracting Temperature Dependent Properties	93
4.4	Effect of Fabrication Variation	95
4.5	Summary	101
4.6	Acknowledgements	101
5	Stability of Composite Resonators	102
5.1	Short Term Stability	102
5.1.1	Composite Quality Factor	104
5.1.2	Electrostatic Transduction in Composite Resonators	106
5.2	Long Term Stability of Frequency	110
5.2.1	Constant Temperature	110
5.2.2	Effect of Changing Electrostatic Field	115
5.3	Summary	119
5.4	Acknowledgements	120
6	Thin Film Stress Temperature Compensation	121
6.1	Package Level Stresses	122
6.2	Optimization of Thin Film Encapsulation	126
6.2.1	Thin Film Thickness Compensation	131
6.2.2	Resonator Design for Thin Film Compensation	133
6.3	Summary	141
6.4	Acknowledgements	142
7	Conclusion, future directions, and impact	143
7.1	Future Directions	145
7.1.1	Composite Design	145
7.1.2	Composite Fabrication	147
7.1.3	Characterization	150
7.2	Impact	151
A	Solution to Equation of Motion with Electrostatics	155

B Anisotropic Young's Modulus of Silicon	158
C Positive TCE of Silicon Dioxide	162
Bibliography	165

List of Tables

1.1	Elastic Properties of Quartz Crystals.	5
1.2	Elastic Properties of Single Crystal Silicon.	23
B.1	Compliance Coefficients of Single Crystal Silicon.	160
B.2	Young's Modulus and it's temperature coefficients.	160

List of Figures

1.1	Quartz crystal resonator in a wristwatch.	2
1.2	Single-anchor, double-ended tuning fork resonator.	9
1.3	Exaggerated deflection of a single-anchor DETF.	9
1.4	Electrostatic actuation of a beam between two electrodes.	10
1.5	Differential element of flexural mode resonator and electrodes.	11
1.6	Flexural-mode beam and differential element of the beam.	14
1.7	Exaggerated deflection of double-anchor DETF.	17
1.8	Frequency-temperature behavior of three silicon devices.	24
2.1	Composite flexural-mode beam and differential element of the beam.	32
2.2	Possible constructions for symmetric Si-SiO ₂ composites with rectangular cross-section areas.	41
2.3	Ideal composite SiO ₂ thickness.	42
3.1	Schematic of silicon on insulator (SOI) wafer with alignment marks.	46
3.2	Resonator definition.	47
3.3	Resonator trench TEOS refill.	48
3.4	First polycrystalline silicon encapsulation layer.	50
3.5	Vent trenches in first encapsulation layer.	51
3.6	HF Vapor release of resonator.	53
3.7	Silicon dioxide growth and composite formation.	55
3.8	Encapsulated composite resonator.	57
3.9	Electrical feedthrough isolation posts.	59
3.10	Metallization for bondpads and electrical traces.	60

3.11	Photograph of a completed wafer containing more than 3,000 resonators.	62
3.12	Wafer postprocessing and resonator die packaging.	62
3.13	Encapsulation membrane buckling during silicon dioxide growth.	64
3.14	Plasma etch of wafer surface attacks silicon dioxide inside the encapsulation.	66
3.15	Plasma damage in silicon dioxide directly under the vents.	67
3.16	Unintentional silicon growth inside the encapsulation after plasma damage removes silicon dioxide.	68
4.1	Singulated composite resonator die next to 0.9 mm pencil lead.	72
4.2	Test setup for measuring frequency-temperature behavior of composite resonators.	73
4.3	Transimpedance amplification circuit diagram.	74
4.4	Multi-resonator experiment setup.	75
4.5	Frequency response of a 1MHz composite resonator using a network analyzer.	76
4.6	Microscope image of a DETF resonator.	77
4.7	Frequency-temperature behavior of composite DETF resonators with varying bending stiffness ratios.	78
4.8	Linear temperature coefficient of frequency TCf_1 at 25 °C.	79
4.9	Comparison of frequency-temperature behavior of silicon, composite, and quartz resonators.	79
4.10	Linear temperature coefficient of frequency at 25 °C and 100 °C for varying bending stiffness ratios.	80
4.11	Tuning of turnover temperature to be at the desirable operating temperature.	81
4.12	TCf_1 of composite resonators oriented in the $\langle 110 \rangle$ and $\langle 100 \rangle$ directions.	82
4.13	Double ring flexural-mode resonators.	83

4.14	Frequency-temperature behavior of flexural-mode ring resonators with varying bending stiffness ratio.	85
4.15	Double ring extensional-mode resonators.	86
4.16	Frequency-temperature behavior of an extensional mode resonator.	87
4.17	Quadratic temperature coefficient of frequency of composite DETF resonators	89
4.18	Nonlinear dependence of quadratic temperature coefficient on linear material properties.	91
4.19	Ideal ratio versus turnover temperature and fit.	94
4.20	Turnover temperature plotted for lithographically identical <110> oriented DETF resonators.	96
4.21	Variation in the turnover temperature due to variation in the ratio, r.	98
4.22	Oven-control of composite resonator away from turnover temperature leads to reduced frequency stability.	99
4.23	Achievable frequency stability for oven-compensation of composite resonators.	100
5.1	Focused Ion Beam (FIB) opening of resonator cavity to expose resonator to the environment.	105
5.2	Comparison of quality factor measurement for various silicon and composite resonators.	105
5.3	Differential element of composite flexural mode resonator and electrodes.	107
5.4	Improvement in transduction factor after thermal oxidation.	109
5.5	Stability of two Silicon 1.3 MHz DETF.	111
5.6	Stability of two 1.3 MHz DETF with a 0.42 μm SiO_2	112
5.7	Stability of two 1.3 MHz DETF with a 0.33 μm SiO_2	112
5.8	Stability of two 1.1 MHz DETF with a 0.33 μm SiO_2	113
5.9	Stability of two 1.0 MHz DETF with a 0.42 μm SiO_2	113
5.10	Stability of two 770 kHz DETF with a 0.33 μm SiO_2	114
5.11	Stability of three 725 kHz DETF with a 0.42 μm SiO_2	114

5.12	Stability of one 725 kHz DETF with a 0.33 μm SiO_2 .	115
5.13	Fitted frequency response.	116
5.14	Change in frequency versus bias voltage for positive and negative polarity.	117
5.15	Long term stability with bias polarity switching of a silicon DETF and two identical composite DETFs.	118
6.1	Cross section of resonator die epoxied to an IC package.	122
6.2	Schematic of cross section of die with double anchored resonator.	123
6.3	Frequency-temperature behavior of a double-anchored DETF attached to a copper lead frame using epoxy.	124
6.4	Axi-symmetric 2D finite element model of resonator die epoxied to a copper leadframe of a plastic IC package.	125
6.5	Experimental and simulated frequency-temperature behavior of a double-anchored DETF attached to copper lead frame using epoxy.	126
6.6	Schematic of cross section of die with double anchored resonator.	128
6.7	Thin film and substrate force / moment balance.	129
6.8	Ideal thickness of compensation layer.	132
6.9	Measured TCf_1 versus thickness of aluminum thin film compensation layer.	133
6.10	Ideal length to width ratios for compensation using a 1 μm thin film of various biaxial moduli and coefficients of thermal expansion.	134
6.11	Layout of aluminum compensation layer.	135
6.12	Measured frequency change versus temperature for DETFs with various L/w ratios.	136
6.13	The TCf_1 at 25 $^\circ\text{C}$ extracted from measurement in Figure 6.12 compared to analytical model	136
6.14	Low temperature cycling of a 1.1 μm sputtered aluminum film on a $\langle 100 \rangle$ silicon wafer.	137
6.15	High temperature cycling of a 1.1 μm sputtered aluminum film on a $\langle 100 \rangle$ silicon wafer.	138
6.16	Frequency hysteresis in aluminum compensated resonator.	140

6.17	Extracted stress hysteresis in compensating aluminum thin film. . . .	141
7.1	Extensional ring resonator with slots.	146
7.2	Modified vents for thermal oxidation of resonator.	148
7.3	Silicon redeposition on composite resonator.	149
7.4	DETF with integrated thermal isolation and resistive heater.	153
7.5	Progress in passive and active compensation of silicon resonators. . .	154
B.1	Definition of direction cosines.	159
B.2	Direction dependent Young's Modulus, TCE_1 , and TCE_2 of Silicon. .	161

Chapter 1

Resonators and Frequency References

The knowledge and tracking of the passage of time is fundamental to the processes and systems that occur in everyday life. A time measurement device has long been sought to subdivide natural periodic events into smaller time segments. Modern electronic devices also require a timekeeping device to operate - a rhythm by which to coordinate its actions. Unlike the ancient systems of timekeeping, such as sundials or pendulums, electronic devices require an electronic periodic signal by which to operate. This rhythm is typically expressed as a periodic voltage signal. A device that provides this continuous signal is called a frequency reference. Frequency references are essential to most electronic devices we use: clocks, microwaves, cell phones, computers, thermostats, televisions, alarm systems, automobiles, and many other consumer, industrial, and military devices.

There are several ways to make an electronic frequency reference. One of the most common ways is to use a mechano-electro-transduction device that converts mechanical vibration into a periodic electrical signal. A resonator is a mechanical device that vibrates at some characteristic frequency. It can be made out of different materials and can have different form factors. The archetypal example of a resonator is a musician's tuning fork which vibrates at a known frequency corresponding to a note with a particular pitch. A tuning fork that is made from a quartz crystal is one of

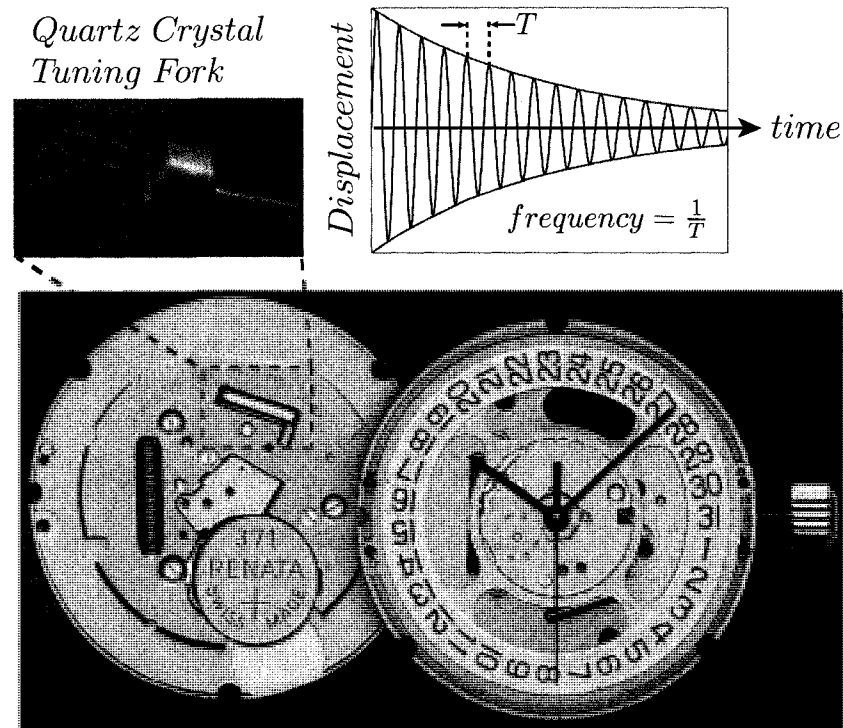


Figure 1.1: Wristwatches use a quartz crystal tuning fork as a frequency reference. The tuning fork is packaged in a metal can to protect it from environmental contaminants. (Bottom) Components of a Swisstime watch [84]. (Top Left) Quartz crystal tuning fork outside of package [66]. (Top Right) Decaying vibration of tuning fork when not part of an oscillator.

the most commonly used frequency references in modern electronics (see Figure 1.1). Crystalline quartz is a piezoelectric material whose vibration results in the generation of a periodic electric potential across the crystal.

Due to energy losses, the vibration of the resonator decays with time (Figure 1.1). To avoid this, the resonator is designed as part of a larger system known as an oscillator. The function of the oscillator is to continuously maintain the vibration of the resonator. If the frequency of the resonator is known and the number of cycles is counted then through a simple relationship the passage of time can be calculated:

$$Time = \frac{\#cycles}{frequency} \quad (1.1)$$

An oscillator that produces a stable frequency output can be used as a frequency reference. Frequency stability is generally described in parts per million (ppm). A 1000 ppm variation is equivalent to a 0.1% change in the frequency. As a rough order of magnitude, if a clock's frequency drifts by 1000 ppm in a day, this would result in almost a 1.5 minute error. Since the frequency of the resonator is sensitive to temperature changes, to be applicable for consumer electronics applications, the stability of the resonator must be below 200 ppm over approximately a 0 °C to 70 °C temperature range. To be useful for many military or industrial applications, it is necessary for the stability to be better than 2 ppm over an even larger temperature range [90, 89].

Great technological advances are possible with the development of high stability frequency references that are very small in size ($< 1 \text{ mm}^3$) and have low power consumption, especially in portable electronics applications [69]. Silicon micro-machining techniques have been developed to produce exceptionally small mechanical structures, on the order of fractions to hundreds of micrometers ($1 \times 10^{-6} \text{ m}$) [74, 38]. For this reason, MEMS researchers have been interested in using silicon micromachining to make silicon resonators as frequency references. Replacing the quartz crystal with silicon as the resonator material provides a unique opportunity for an integrated semiconductor and frequency reference solution.

1.1 Quartz Crystal Resonators

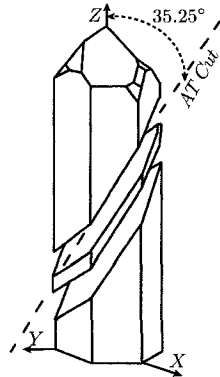
There were approximately 10 billion quartz crystal resonators sold in 2007 - a \$3.2 billion market [14]. From ubiquitous and inexpensive consumer electronics applications, such as USB sticks and wrist watches, to high value military and industrial systems, such as satellites, the quartz crystal provides an oscillating signal that acts as a timing pulse for integrated circuits. Approximately 80% of modern electronic devices have two systems: a silicon integrated circuit providing the functionality of

the device and a quartz crystal frequency reference that provides the circuit with a timing signal [14].

Frequency references based on crystalline quartz have become a dominant technology for several reasons [90, 89]:

1. The quartz crystal is a piezoelectric material that couples the mechanical and electrical domains. As the quartz crystal vibrates, the strain in the crystal results in the formation of an electric field across the crystal, making quartz crystals a natural choice for a frequency reference. Metal electrodes are typically deposited on the surface of the crystal to transmit the oscillating voltage.
2. When operating in a low pressure environment, the quartz crystal minimally dissipates vibrational energy.
3. In the mid-20th century it was discovered that the vibration of particular cuts of the quartz crystal had opposing temperature coefficients of stiffness [31]. Certain cuts had negative temperature coefficients while other orientations had positive temperature coefficients (see Table 1.1). By optimizing the orientation of the cut through the quartz crystal, temperature insensitive cuts that had less than 200ppm variation over a -55 °C to 125 °C range, were discovered.
4. Great care was taken to properly package the quartz crystal resonator to reduce the “aging” phenomenon. Aging is described by the International Radio Consultative Committee as “systematic changes in frequency with time due to internal changes.” Aging could be due to contamination within the package or stress changes due to the electrodes or leads connected to the resonator. To minimize aging, quartz crystals are hermetically packaged in a vacuum sealed metal can (see Figure 1.1).

Electronic circuit compensation is used to further improve the temperature-frequency stability. The temperature-compensated crystal oscillator (TCXO) uses a thermistor network and a varactor that is put in series with the crystal. The system is calibrated such that the varactor has a temperature dependence trend that



Elastic Constants (GPa)		Temperature Coefficients (ppm/°C)	
c_{11}	86	TCc_{11}	-46.5
c_{12}	5.1	TCc_{12}	-3300
c_{13}	10.5	TCc_{13}	-700
c_{14}	18.3	TCc_{14}	-900
c_{33}	107	TCc_{33}	-205
c_{44}	59	TCc_{44}	-166
c_{66}	41	TCc_{66}	+164

Table 1.1: Elastic Properties of Quartz Crystals. The anisotropic stiffness constants and the temperature coefficients (TC) of the stiffness constants are given. (Left) Image of a quartz crystal with the popular AT-Cut. [8, 67]

is opposite of the quartz crystal. The resulting output signal is compensated to less than 10 ppm. To achieve better than 0.1 ppm stability, the oven-controlled crystal oscillator (OCXO) was developed. This bulky system combines the resonator with a temperature sensor and heater. The heater maintains the temperature of the resonator and driving circuits at a constant elevated temperature, regardless of the ambient temperature. This system can consume several Watts of power and can be several centimeters along each dimension.

One of the main sources of error in the TCXO and the OCXO systems is imprecise thermometry due to the physical separation between the resonator and temperature sensor or temperature sensitive circuit. One of the most recent developments in improving the temperature-frequency stability makes use of the different temperature dependencies of different modes within a single quartz crystal resonator. The different temperature dependencies allows the formation of a beat frequency with a high temperature sensitivity. The beat frequency is used as the resonator's self-temperature sensor. In the microcomputer-compensated crystal oscillator (MCXO), the micro-controller makes use of the beat frequency to generate a digitally compensated frequency [91].

Over the last couple decades, advances in silicon processing have allowed silicon circuits to shrink exponentially. These advancements have to a large extent stemmed

from improved lithography allowing for finer features and thus reduced transistor size. Quartz crystals have also realized moderate levels of size reduction. Next generation crystal oscillators will achieve volumes of less than 1.5mm^3 [28]. However, the packaging of quartz crystals will become the major barrier to further size reduction without a paradigm shift in the fabrication and packaging of the resonators. Today, quartz crystals continue to be packaged in metal cans, requiring careful insertion of the quartz crystals, attachment to electrical leads, and hermetic sealing. Since quartz can not be integrated into semiconductor processing, the dual semiconductor - quartz oscillator systems will persist. A fundamental change can occur only by making resonators that are compatible with semiconductor processing.

1.2 Silicon MEMS Resonators

There are several attributes that allow silicon resonators to compete with and outperform quartz crystal resonators. Using micromachining techniques, silicon resonators can be batch fabricated in small form factors allowing large volume manufacturing. Tens of thousands of resonators can be made on a single 8" wafer. This allows silicon resonators to be cost competitive with quartz resonators. However, the major breakthroughs that will put silicon resonators one step ahead of quartz crystals come from advances in wafer-scale and wafer-level packaging of the resonators. Using thin-film encapsulation [50, 22] and wafer-bonding techniques [46], researchers have shown that these batch packaging methods have yielded hermetically sealed parts with improved aging characteristics - within 3 ppm/year. If thin-film encapsulation is used, the footprint of the package remains at the size of the device. This allows unprecedented reduction in the size of a hermetically sealed resonator. Kim et al. [50] and Candler et al. [22] showed hermetically sealed devices with a volume of less than 1mm^3 that have the potential to be reduced even further. It is essential that high integrity packaging methods yield silicon resonators with aging characteristics on par or better than quartz crystal resonators. Inexpensive quartz crystal oscillators age approximately 5-10 ppm/year [87].

In making CMOS-integrated silicon resonators, a debate is ongoing as to whether

the manufacturing flow should be “MEMS-first” or “MEMS-last”. In the “MEMS-last” technique, the CMOS circuits are fabricated first, ensuring that pristine single-crystal-wafers are used in tightly process controlled semiconductor foundries [45]. The MEMS is then fabricated through a series of deposition and etching steps. Although this method guarantees the integrity of the CMOS-circuits, it limits the thermal budget of subsequent MEMS processing to under 450 °C or lower, due to the melting temperature of certain materials. This limitation results in using polycrystalline or amorphous materials for the MEMS structure and limits the packaging to low-temperature methods such as wafer-bonding. The use of wafer-bonding packaging increases the footprint of the package and calls into question the ability to be size-competitive with subsequent generations of quartz crystal resonators. In the “MEMS-first” approach, the resonators can be built from single-crystal silicon wafers and could be subjected to high temperature (> 1000 °C), low-pressure packaging processes that results in exceptionally clean, hermetic packaging. “MEMS-first” processes are under scrutiny by CMOS-foundries due to the difficulty of ensuring CMOS-integrity on pre-processed wafers. However, in 2008, Taiwan Semiconductor Manufacturing Co Ltd (TSMC), one of the largest CMOS foundries, began opening the door for MEMS development in their foundries [65].

Kim [50] and Candler [22] addressed the problem of silicon resonator aging by developing high-integrity hermetic packaging, “epi-seal”, of pristine single-crystal silicon resonators. The devices showed no sign of surface contamination or fatigue at room temperature operation. The package proved permeable only to small gas molecules, such as hydrogen and helium, and only at higher temperatures (100 °C) [49]. However, aging is just a part of the total drift that a resonator can exhibit. Environmental effects, such as frequency changes due to temperature, can limit the usability of the device. Unlike quartz crystals, there is no orientation of the silicon crystal that results in temperature-insensitive resonators. Over -55 °C to 125 °C, the silicon resonator exhibits a more than 5000 ppm frequency variation - an order of magnitude greater than quartz crystal resonators.

MEMS researchers have employed electronic based compensation techniques, similar to those described in section 1.1 on quartz crystal resonators, and have achieved

higher levels of temperature-frequency stability. Some of these techniques will be described in later sections. In a laboratory setting, it was shown that the temperature of the silicon resonator can be maintained to within ± 0.1 ppm in an oven controlled scheme [36]. However, none of the schemes have successfully achieved OCXO levels of temperature stability due to the very high temperature-sensitivity of silicon.

In the following sections, a foundation is established for analyzing the frequency and temperature dependence of a silicon resonator. Methods for temperature compensation are described and a way forward is paved for developing silicon-based resonators that have inherent frequency stability comparable to quartz crystal resonators.

1.2.1 Electrostatically Actuated Resonators

One of the straightforward ways to create a mechano-electro-transduction silicon resonator is to use electrostatic actuation and sensing. An electrostatic transduction system contains the moving element that is separated by an initial electrostatic gap, g , from a series of stationary electrodes. Typically, a potential difference between the moving structure and electrodes is established by biasing the moving element with a voltage source, V_{Bias} . The electric field does work on the charges that develop on the surfaces of the structures, thereby applying a force to the moving structure. If an alternating electric field is established, the moving structure responds by vibrating at the frequency of the alternating electric field. The moving structure will experience the largest displacement when the frequency of the electric field is matched to the natural frequency of the moving structure.

Figure 1.2 shows an electrostatically actuated, single-anchor, double-ended tuning fork (DETF) resonator, which is the basis of most of the work presented. The mode of operation is the anti-symmetric flexural mode where the beams vibrate out of phase (see Figure 1.3). The DETF is electrostatically actuated and sensed using electrodes placed on either side of the beam. A small amplitude AC voltage source is applied on the outer two input electrodes forcing the beams into motion. A DC bias source, V_{Bias} , is applied to the resonator. This bias source amplifies the force of actuation.

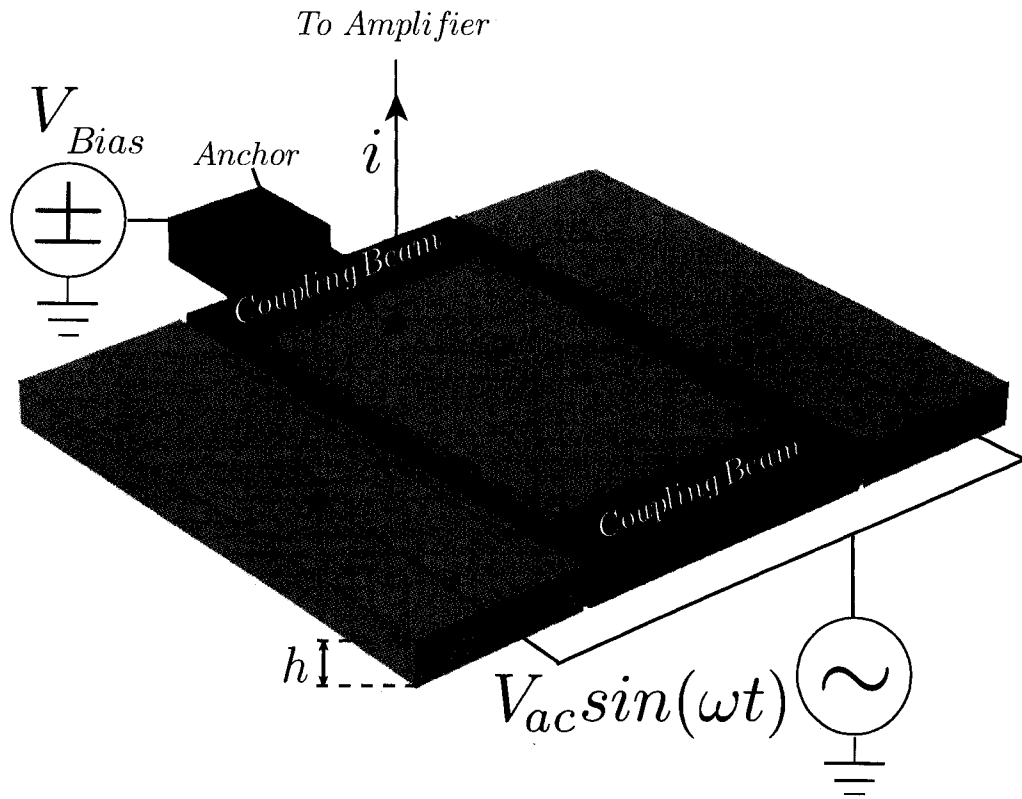


Figure 1.2: Single-anchor, double-ended tuning fork resonator.

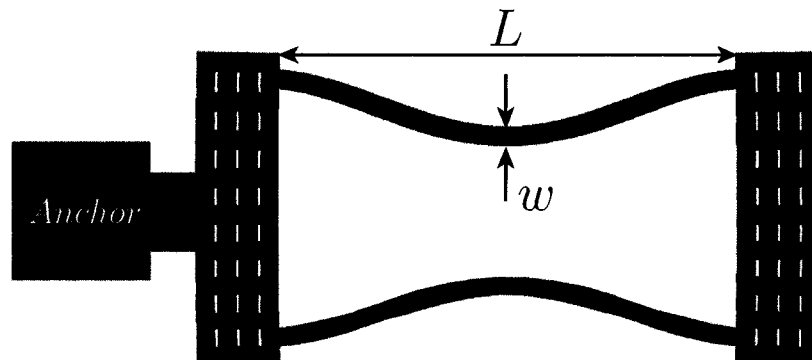


Figure 1.3: Exaggerated deflection of a single-anchor DETF.

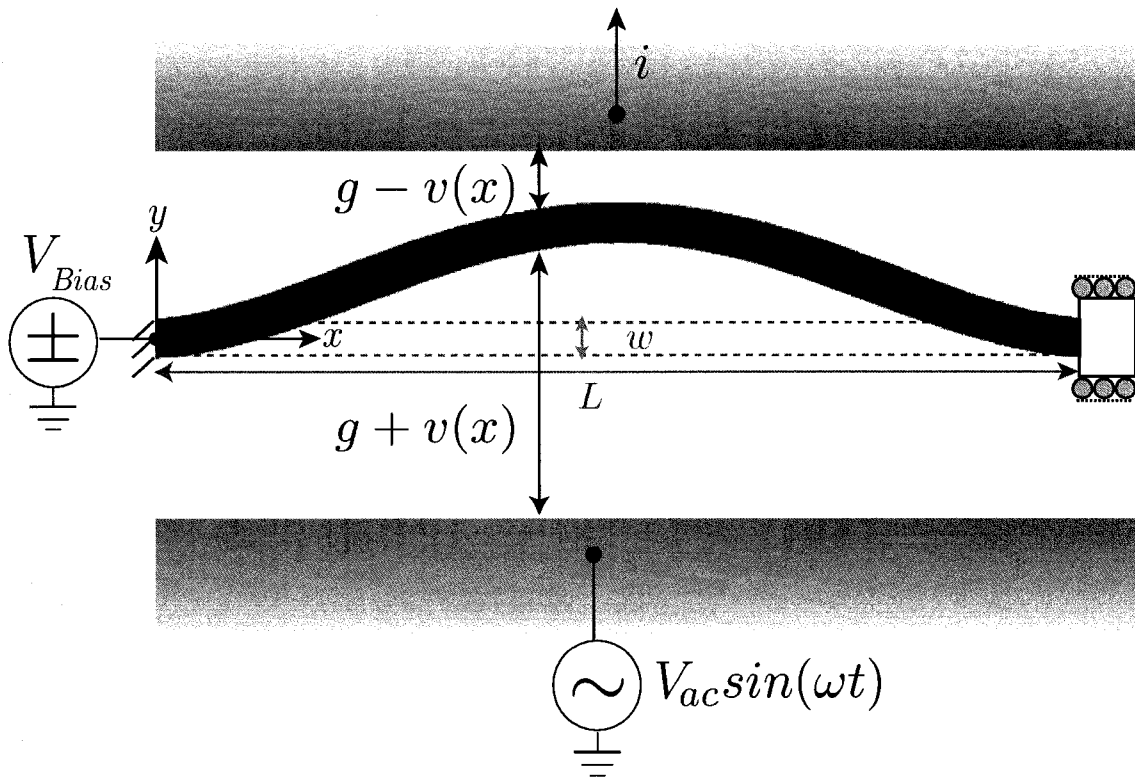


Figure 1.4: Electrostatic actuation of a beam between two electrodes.

As the beams vibrate, their vibration is sensed by an inner output electrode.

This system can be described as two slender beams between two rigid coupling beams. If the coupling beams are assumed to be perfectly rigid, then the vibration of the DETF can be simplified to that of a beam in flexure-mode vibration. The boundary conditions on the slender vibrating beams can be modeled as clamped-guided. The guided behavior is the result of one of the coupling beams being free to move, a consequence of having a single anchor. The implication is that the vibrating beam will not hold axial loads as it is free to expand and contract during vibration. Figure 1.4 shows the simplified model of the DETF with a clamped-guided beam separated by a gap, g , from an input electrode and an output electrode. As the beam vibrates, the y -direction displacement, $v(x)$, modifies the gap between the beam and electrodes. For small deflections, this system can be modeled as a moving parallel

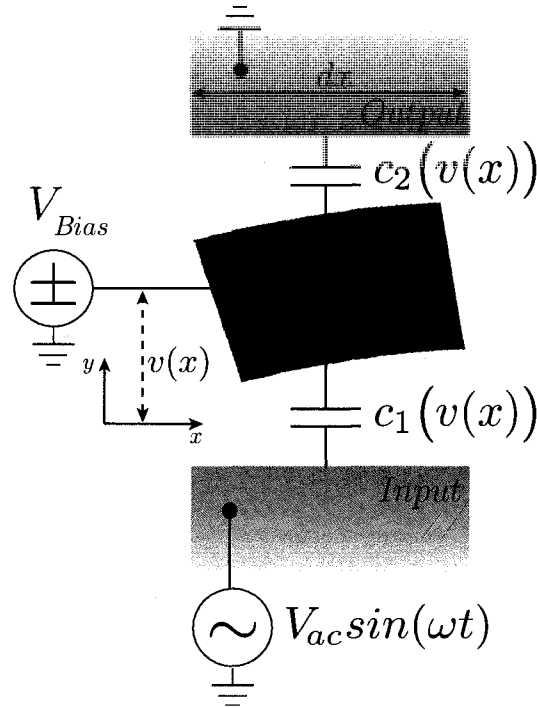


Figure 1.5: Differential element of flexural mode resonator and electrodes.

plate capacitor system with an electrostatic area $A_e = hL$ where L is the length of the beam and h is the dimension of the beam not shown in the figure.

To determine the electrostatic force, we consider a differential element of length dx shown in Figure 1.5. The capacitance of the beam and each electrode is inversely proportional to the changing gap. Simple Taylor expansions describe the differential element capacitance between a conductive beam and the surrounding electrodes:

$$c_1(v) = \frac{\epsilon_o h}{g + v(x)} dx = \frac{\epsilon_o h}{g} \sum_{n=0}^{\infty} \left(-\frac{v(x)}{g} \right)^n dx \quad (1.2)$$

$$c_2(v) = \frac{\epsilon_o h}{g - v(x)} dx = \frac{\epsilon_o h}{g} \sum_{n=0}^{\infty} \left(\frac{v(x)}{g} \right)^n dx \quad (1.3)$$

The electrostatic force is determined by the change in energy stored by the capacitor with displacement. Since the bias voltages do not change with displacement and

$V_{ac} \ll V_{Bias}$ this simplifies to:

$$f_e(v) = \frac{1}{2} \frac{\partial c_1(v)}{\partial v} \left(V_{Bias} - V_{ac} \sin(\omega t) \right)^2 + \frac{1}{2} \frac{\partial c_2(v)}{\partial v} V_{Bias}^2 \quad (1.4)$$

$$f_e(v) \approx \frac{1}{2} \frac{\partial}{\partial v} \left(c_1(v) + c_2(v) \right) V_{Bias}^2 - \frac{\partial c_1(v)}{\partial v} V_{Bias} V_{ac} \sin(\omega t) \quad (1.5)$$

If the Taylor expansion formulation of the capacitance is used in equation 1.5, then the equation is simplified to:

$$f_e(v) = \frac{\epsilon_0 h}{g^2} V_{Bias}^2 \sum_{n=1}^{\infty} 2n \left(\frac{v(x)}{g} \right)^{(2n-1)} dx - \frac{\epsilon_0 h}{g^2} V_{Bias} V_{ac} \sin(\omega t) \sum_{n=1}^{\infty} n \left(\frac{v(x)}{g} \right)^{(n-1)} dx \quad (1.6)$$

There are several things to note regarding equation 1.5 and 1.6 their role in the analysis of the system:

1. There are two factors that complicate the analysis of the electrostatically actuated system. The inversely proportional dependence of the capacitance on the gap between the beam and electrode results in a non-linear electrostatic force. Furthermore, since the displacement, v , is a function of x , the electrostatic force varies along the length of the beam.
2. The first term of the forcing function in equation 1.6 does not have a time dependence and is only a function of displacement. As we will see in section 1.2.2, this term puts the system into a positive feedback loop; as the displacement increases (i.e. the electrostatic gap shrinks), the electrostatic force increases. Consequently, the displacement dependence of the force results in an effective “softening” of the system. As a result, the frequency of the beam will depend on the bias voltage as well as the capacitance of the system.
3. For completeness it is useful to note the total force on the beam. This can be

derived by integrating equation 1.5 over the length of the beam. However, a road block is encountered since the displacement profile is not known *a priori*. To fully solve for the force, the differential equation of motion must be modeled using a finite element software or finite difference techniques [13]. However, a rough approximation can be made since the displacement of the beam is assumed to be very small. For $v(x) = 0$, the total force on the beam reduces to:

$$\begin{aligned} F_e &= \int_0^L f_e(v(x) = 0) dx \\ &= \frac{\varepsilon_0 h L}{g^2} V_{Bias} V_{ac} \sin(\omega t + \pi) \end{aligned} \quad (1.7)$$

The vibration of the beam is electrostatically sensed by monitoring the capacitance change between the beam and the output electrode:

$$i = \int_0^L \frac{\partial c_1(v)}{\partial t} V_{Bias} \quad (1.8)$$

In the following sections we will mathematically describe the frequency of vibration and some of the effects that can influence the frequency of vibration.

1.2.2 Frequency

To determine the vibration of the beam, we will use an Euler-Bernoulli formulation. By summing the forces and moments on a differential element (Figure 1.6) we can determine the equation of motion [76]:

$$\rho A \frac{\partial^2 v}{\partial t^2} + \frac{\partial^2 M}{\partial x^2} - P \frac{\partial^2 v}{\partial x^2} = f_e(v) \quad (1.9)$$

where for small deflections

$$M = B \frac{\partial^2 v}{\partial x^2} \quad (1.10)$$

and

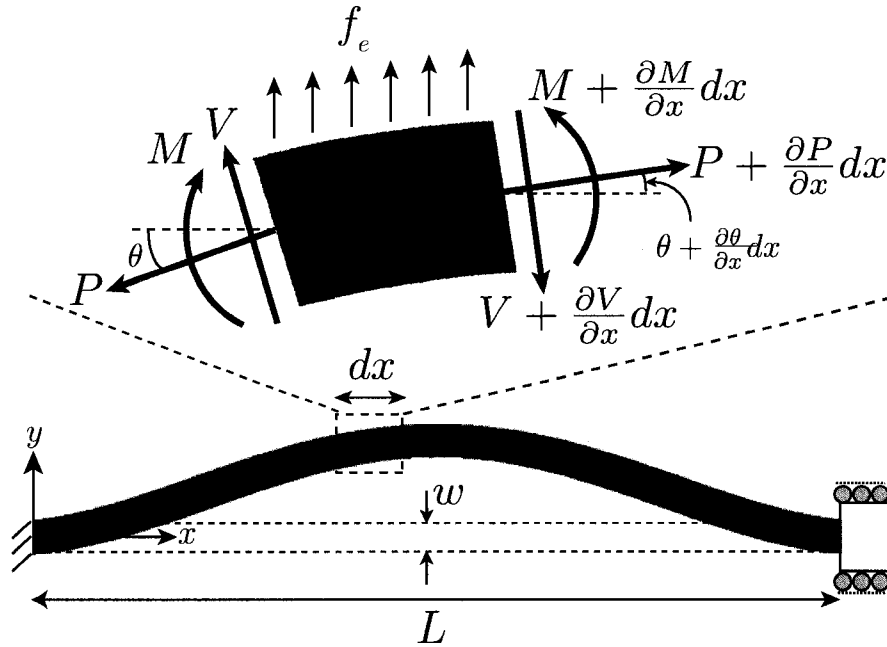


Figure 1.6: Flexural-mode beam and differential element of the beam.

$$B = EI \tag{1.11}$$

In the equations above, v is the displacement in the y -direction, ρ is the density, A is the cross sectional area of the beam (i.e. hw), M is the internal moment, P is the internal axial load, f_e is the electrostatic force on the element, and the derivatives are taken with respect to time, t , and the direction x . The bending stiffness, B , is defined as the Young's Modulus, E , multiplied by the 2nd moment of inertia, I . For a beam with a rectangular cross-section, $I = \frac{hw^3}{12}$, where h is the height of the beam and the width, w , is the dimension in the direction of vibration.

To solve this equation the following boundary conditions are useful:

$$\begin{aligned}
v(x = 0) &= 0 \\
\frac{\partial v}{\partial x}(x = 0) &= 0 \\
v(x = L) &= 0 \\
\frac{\partial v}{\partial x}(x = L) &= 0
\end{aligned} \tag{1.12}$$

The implication of the guided boundary condition is that the axial load, P , must be zero. The natural frequency of the structure can be determined by setting the forcing function, f_e , to zero and solving for the homogeneous solution to the equation:

$$\rho A \frac{\partial^2 v}{\partial t^2} + B \frac{\partial^4 v}{\partial x^4} = 0 \tag{1.13}$$

The resulting flexural-mode natural frequency of this beam is just a function of material properties and dimensions:

$$f_n = \frac{\beta^2}{2\pi} \sqrt{\frac{B}{mL^3}} \tag{1.14}$$

In equation 1.14, β is the flexural-mode constant and $m = \rho AL$ is the total mass of the beam. For the first mode of a clamped-clamped beam $\beta = 4.73$.

Effects of Electrostatics

The homogeneous solution described in the previous section assumes that the force is not displacement dependent. However, as seen in section 1.2.1, the electrostatic force depends on the displacement of the vibrating structure relative to the electrode. For very small displacements, $v(x) \ll g$, the electrostatic force can be simplified by only considering the first, non-time dependent, term in the Taylor expansion of the electrostatic force in equation 1.6:

$$\rho A \frac{\partial^2 v}{\partial t^2} + B \frac{\partial^4 v}{\partial x^4} = \frac{2\epsilon_0 h}{g^3} V_{Bias}^2 v \tag{1.15}$$

An analytical solution to equation 1.15 can be found by rewriting it as:

$$\rho A \frac{\partial^2 v}{\partial t^2} + B \frac{\partial^4 v}{\partial x^4} - \frac{k_e}{L} v = 0 \quad (1.16)$$

where

$$k_e = \frac{2\varepsilon_o A_e}{g^3} V_{Bias}^2 \quad (1.17)$$

In equation 1.17, k_e is often referred to as the electrostatic spring stiffness, V_{Bias} is the applied bias voltage, ε_o is the permittivity of free space, A_e is the electrostatic area (hL), and g is the electrostatic gap. Appendix A shows the complete solution to equation 1.16 using the method of separation of variables. The frequency corresponding to the modified equation can be written in terms of the natural frequency found in equation 1.14:

$$f = f_n \sqrt{1 - r_e} \quad (1.18)$$

where

$$r_e = \frac{1}{(2\pi)^2} \frac{k_e}{m} \frac{1}{f_n^2} \quad (1.19)$$

Because the electrostatic force is attractive, it acts as a positive feedback system, increasing as the electrostatic gap decreases. The positive feedback system presents itself in the form of a negative electrostatic spring in equation 1.16, k_e , that reduces the effective stiffness of the system. This results in the reduction of the frequency of vibration. The magnitude of reduction depends on the non-dimensional ratio, r_e , which is effectively a ratio of the frequency associated with the electrostatic spring and the natural frequency of the beam.

In the present analysis we have ignored some of the higher order terms that would capture nonlinearities in the system. These higher order terms are present not only in the nonlinear electrostatic forcing function, but also when describing nonlinear behavior of the beam under large amplitudes of vibration [47]. The consideration of these terms is complex, but important in the study of modulation of noise in the system [3]. The present and subsequent analysis ignore these nonlinearities under the assumption of very small beam deflections. Furthermore, experiments were performed with care to avoid operating in strongly nonlinear regimes.

Effect of Axial Loads

The presence of axial loads is important to consider particularly for vibrating structures with boundary conditions that restrict axial expansion and contraction. This is possible in DETF structures that have multiple anchors which constrain displacement (Figure 1.7). For a double anchored DETF structure, the additional boundary conditions must be considered:

$$\begin{aligned} u(x=0) &= 0 \\ u(x=L) &= 0 \end{aligned} \tag{1.20}$$

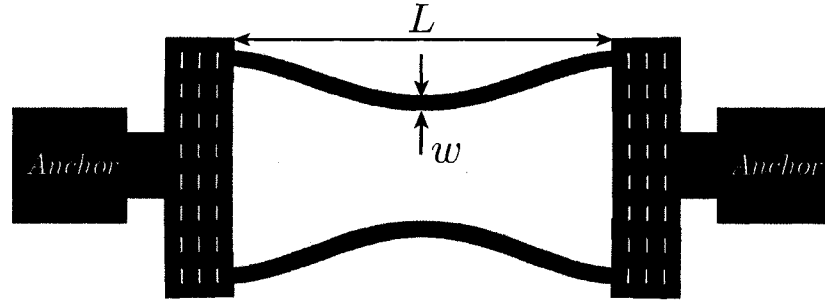


Figure 1.7: Exaggerated deflection of double-anchor DETF.

In equation 1.20, u is the displacement in the x direction. The vibration of the double anchored DETF can be modeled as a clamped-clamped beam. A closed form solution for the frequency of a clamped-clamped beam with the inclusion of axial load, P , does not exist. However, approximations can be found in Blevins [12].

$$f = f_n \sqrt{1 + r_b} \tag{1.21}$$

where

$$r_b = \frac{P}{P_b} \tag{1.22}$$

and

$$P_b = \frac{(2\pi)^2 EI}{L^2} \quad (1.23)$$

When axial stresses are present, the mechanism for frequency shifting is similar to that of a guitar string. As the tension in the guitar string is increased, the frequency of the guitar string increases as well.

We can combine the effects of axial loads and electrostatics into a single equation describing the modification of natural frequency as:

$$f = f_n \sqrt{(1 - r_e)(1 + r_b)} \quad (1.24)$$

1.2.3 Quality Factor

Quality factor is a measure of energy loss in an oscillatory system. It is related to the damping in the system and thus how quickly a resonator will ring down under a given impulse. Higher quality factors help to reduce the motional resistance of the resonator and increase the current output of the resonator. Quality factor is defined as the ratio of the energy stored to energy lost in a given cycle of oscillation:

$$Q = 2\pi \frac{\text{Energy stored}}{\text{Energy lost per cycle}} \quad (1.25)$$

The most intuitive mechanism of energy loss is through collision with gas molecules, also known as air damping. Mechanisms such as thermoelastic dissipation (TED) [21] and Akheiser effect (AKE) [23] capture energy lost due to global and local phonon interaction, respectively. Other mechanisms, such as surface effects [94] and anchor loss [72, 11] can also contribute to energy loss. All of these mechanisms can be combined together to represent the total Quality factor as a function of the quality factors due to each mechanism.

$$\frac{1}{Q_{Total}} = \frac{1}{Q_{Air}} + \frac{1}{Q_{TED}} + \frac{1}{Q_{AKE}} + \frac{1}{Q_{Anchor}} + \frac{1}{Q_{Surface}} \quad (1.26)$$

Equation 1.26 indicates that the total quality factor will be dominated by the mechanism with the lowest quality factor. When devices are operated in air, the

dominant mechanism is usually air damping. This is particularly true for resonators with low frequencies. However, the DETF presented in this work were all packaged in a low-pressure environment, < 1 Pa. The dominant energy loss mechanism in this situation has been previously found to be thermoelastic dissipation [21].

1.3 Temperature Dependence

The temperature of a substance is an indication of the amount of energy stored by the atoms in the substance. As temperature is increased, the atoms have higher vibrational energy and move away from each other. The expansion of the atomic bonds is characterized by the coefficient of thermal expansion, α . This dimensional change is usually also accompanied by a reduction in the stiffness of the atomic bonds. The consequence is that most materials will not only expand with increasing temperature, but will also become more compliant.

In this section the effect of material properties and dimensions on the frequency behavior are examined. Other mechanisms, such as effect of electrostatic actuation and axial loads, can also dictate the final temperature dependence of a resonator.

1.3.1 Generalized Temperature Coefficients

To determine the temperature dependence of vibration, we will first develop the concept of generalized temperature coefficients. Consider a generic function g that depends on the temperature, T . Using Taylor expansion, the function can be described as the infinite sum of derivatives of function g about a reference temperature T_o where $g_o = g(T_o)$.

$$g(T) = g_o \left(1 + \sum_{n=1}^{\infty} TCg_n \Big|_{T_o} (T - T_o)^n \right) \quad (1.27)$$

where

$$TCg_n = \frac{1}{n!} \frac{\partial^n g}{\partial T^n} \quad (1.28)$$

In equation 1.28, $T C g_n$ is the n th-order temperature coefficient of g . It is important to note that if g is a polynomial of order k , then the summation from $n = 1$ to k in equation 1.27 will perfectly capture the behavior of the polynomial. In the subsequent sections we will find that the first and second order coefficients are sufficient for capturing the dominant temperature-frequency behavior.

The generalized temperature coefficients can be used to capture the temperature dependencies of material properties and dimensions. To illustrate this, we consider a generic beam of initial length L_o . If the temperature of the beam is increased, the beam expands to a length of L . The first-order temperature coefficient of L is the coefficient of thermal expansion, α .

$$TCL_1(T_o) = \left. \frac{1}{L_o} \frac{\partial L}{\partial T} \right|_{T_o} = \alpha(T_o) \quad (1.29)$$

The second-order temperature coefficient of L captures the temperature dependence of the coefficient of thermal expansion:

$$TCL_2(T_o) = \left. \frac{1}{2L_o} \frac{\partial^2 L}{\partial T^2} \right|_{T_o} = \left. \frac{1}{2} \frac{\partial \alpha}{\partial T} \right|_{T_o} \quad (1.30)$$

To simplify viewing of equations, the evaluation of temperature coefficients is assumed to be at a specified temperature. In other-words, the reader should assume that $TCL_1 = TCL_1(T)$ where T is the relevant temperature based on the context. When temperature coefficient calculations are performed, the the variables are taken at the specified temperature.

1.3.2 Temperature Coefficients of Frequency

Applying the concepts from the previous sections to determine the temperature coefficients of frequency for a single material beam in flexural-mode. Substituting equations 1.14, 1.19, 1.22 and 1.23 into equation 1.24, taking the appropriate derivatives, and simplifying, the linear temperature coefficient of frequency is:

$$TCf_1 = \frac{(\alpha + TCE_1) - \alpha(r_b - r_e) + \left(\frac{1}{P_b} \frac{\partial P}{\partial T}\right) - 2r_e \left(\frac{1}{V_{Bias}} \frac{\partial V_{Bias}}{\partial T}\right)}{2(1 + r_b - r_e)} \quad (1.31)$$

Equation 1.31 assumes that the coupling between the axial loads and the electrostatic spring stiffness is very weak. In other words, $r_b \ll 1$ and $r_e \ll 1$; therefore, $r_b r_e \ll 1$ can be neglected.

The dependence of axial load on temperature, $\frac{\partial P}{\partial T}$, and dependence of bias voltage on temperature, $\frac{\partial V_{Bias}}{\partial T}$, are two user-defined control parameters that can be used to adjust the temperature coefficient of frequency. In section 1.4, we will see how these control parameters can be used to make a “zero-TCF” resonators.

There are several consequences of equation 1.31 that are worth considering when the controls are not used, i.e. $\frac{\partial P}{\partial T} = 0$, $\frac{\partial V_{Bias}}{\partial T} = 0$.

1. If the effects of electrostatic actuation and axial loading of the beam are ignored ($r_e = 0, r_b = 0$), equation 1.31 simplifies to:

$$TCf_1 = \frac{TCE_1 + \alpha}{2} \quad (1.32)$$

This result is equal to the temperature coefficient of the natural frequency described by equation 1.14. This is an important result showing that the temperature dependence of the natural frequency is just a function of material properties.

2. If the resonator is electrostatically actuated but cannot sustain axial loads (i.e. $r_b = 0$), as in the case of a single-anchored DETF:

$$TCf_1 = \frac{(\alpha + TCE_1) + \alpha r_e}{2(1 - r_e)} \quad (1.33)$$

The non-dimensional ratio r_e has the effect of “pulling” the frequency and thereby changing the temperature coefficient of frequency. For example, note that from equation 1.18:

$$\frac{1}{1 - r_e} = \frac{f_n^2}{f^2} \quad (1.34)$$

Electrostatic actuation shifts the frequency of the resonator, $f < f_n$, and increases the temperature coefficient of frequency.

Higher Order Temperature Coefficients

Higher order temperature dependencies of the frequency can also be found by taking the second and higher derivatives of frequency. However, the full descriptions can be lengthy and are best performed by a computer. If terms with higher powers are ignored (i.e. $TCE_2 \gg TCE_1^2$), then the quadratic temperature coefficient of frequency of a single-anchored DETF reduces to:

$$TCf_2 = \frac{2TCE_2 + \frac{\partial \alpha}{\partial T}(1 + r_e)}{4(1 - r_e)} \quad (1.35)$$

In equation 1.35, TCE_2 is the quadratic temperature coefficient of Young's Modulus. Since the temperature dependence of Young's Modulus tends to be much greater than the coefficient of thermal expansion, it is found that the error from ignoring the higher order terms can be approximated as $-TCE_1^2/8$.

Effect of Damping on the Temperature Coefficients

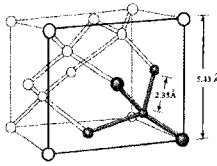
In the previous sections, the equations of motion did not include the effects of damping, and thus the effect of quality factor on the frequency of vibration. The damped frequency of vibration is related to the undamped frequency of vibration through [76]:

$$f_d = f\sqrt{1 - \zeta^2} \quad (1.36)$$

In equation 1.36, ζ is the damping ratio and is related to the quality factor of the resonator by $\zeta = \frac{1}{2Q}$. The TCf will therefore depend on the temperature dependence of quality factor [52].

$$Q(T) = Q_o \left(\frac{273 + T_o}{273 + T} \right)^\gamma \quad (1.37)$$

Where Q_o is the quality factor at temperature T_o in Celsius. Taking the temperature derivatives of equation 1.36, we find:



Elastic Constants (GPa)		Temperature Coefficients			
		Linear (ppm/°C)		Quadratic (ppb/°C ²)	
c_{11}	165.64	$TC_{c_{11},1}$	-74.87	$TC_{c_{11},2}$	-45.14
c_{12}	63.94	$TC_{c_{12},1}$	-99.46	$TC_{c_{12},2}$	-53.95
c_{44}	79.51	$TC_{c_{44},1}$	-57.98	$TC_{c_{44},2}$	-20.59

Table 1.2: Elastic Properties of Single Crystal Silicon. [15]

$$TCf_d = \frac{\gamma}{(273 + T)} \frac{1}{(1 - 4Q^2)} + TCf \quad (1.38)$$

For a silicon resonator, γ is generally found to be $0.5 < \gamma < 4$. For high quality factors, the effect of quality factor on frequency can be much less than parts per billion.

Temperature Dependence of Silicon Flexural Mode Resonators

Silicon is an elastically anisotropic material. As such, the single material constant, Young's Modulus, cannot be used to describe the elastic properties of the material. The Young's Modulus can only be applied in the idealized circumstance where the stress state is described by a single-directional component. This is the case for a flexural-mode beam under uni-axial bending and/or normal compression or tension. The Young's Modulus in the $\langle 100 \rangle$ direction can be described as the inverse of the S_{11} compliance. Appendix B provides an in depth discussion of the changes in Young's Modulus and its temperature derivatives as a function of direction within the silicon crystal. The use of the Young's Modulus in this dissertation assumes that the appropriate direction has been chosen to evaluate the Young's Modulus. Most of the experiments use $\langle 110 \rangle$ direction oriented beams.

For a beam made out of silicon, the linear temperature coefficient of Young's Modulus is a large negative number that will dominate any of the dimensional changes due to the coefficient of thermal expansion. The TCE of a beam oriented in the $\langle 110 \rangle$ directions is approximately -63.8 ppm/°C[16].

The quadratic temperature coefficient of frequency will depend on higher order

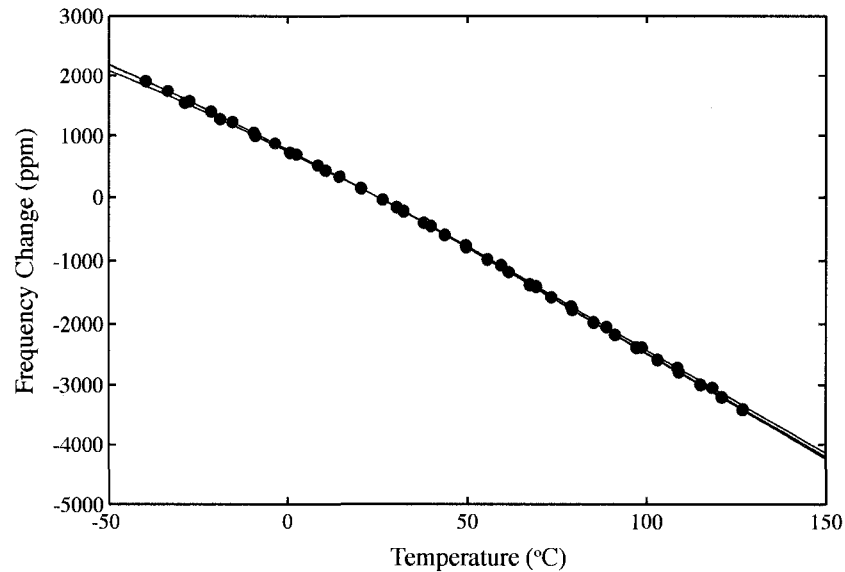


Figure 1.8: Frequency-temperature behavior of three silicon devices.

temperature dependencies. From literature values found at room temperature, the linear and quadratic temperature coefficients of frequency at 25 °C are approximately $-30.5 \text{ ppm}/^\circ\text{C}$ and $-26.5 \text{ ppb}/^\circ\text{C}^2$, respectively.

A measurement of three silicon resonators indicates that the measured value is comparable to the expected value with the linear and quadratic temperature coefficients of frequency at 25 °C of $-31.4 \text{ ppm}/^\circ\text{C}$ and $-26.4 \text{ ppb}/^\circ\text{C}^2$, respectively. Over approximately a 150 °C temperature range, the frequency of the silicon resonator shifted by approximately 4500 ppm. This level of variation is unacceptable for most applications.

1.4 Temperature Compensation Techniques

The methods used to compensate silicon microelectromechanical resonators can be categorized as being passive or active. The primary difference is whether the compensation method consumes power in order to perform the compensation function.

Active temperature compensation methods employ a open or closed loop control

schemes to maintain the frequency of the resonator constant. Some techniques combine information about the current temperature of the resonator with a previously performed calibration. The purpose of the calibration is usually to perform an open loop control of frequency by control of a parameter to which the frequency is sensitive. Active compensation methods tend to consume additional power because of the control circuitry and their effectiveness is directly related to the thermometry used in the sensing of the resonator's temperature.

Passive compensation methods do not require knowledge of the current temperature of the resonator. These compensation methods are based on design of the resonator geometry and materials. Since the techniques do not require control electronics they do not consume additional power.

1.4.1 Passive Stress Compensation

In chapter 1 section 1.2.2 the effect of axial loads on frequency of a flexural-mode beam was described. It was found that axial tension or compression would lead to an increase or reduction in the frequency of the resonator, respectively. One of the ways to passively compensate temperature dependent frequency changes is to design beam structures in which axial stresses are induced. Thermal axial stresses can be designed to induce tension in the beams to directly counter the decrease in frequency due to temperature. The use of thermal stresses in the beam model typically involves use of materials with different coefficients of thermal expansion as well as multiple anchors to transmit the stresses. This methodology is generally limited to beams in flexural mode. The design of thermal stresses becomes tricky, if not infeasible, when introduction of unintentional stresses, such as during packaging, are considered.

Chapter 6 will describe one way to simply induce thermal stress into the process described in this dissertation. A frequency variation of 200 ppm is achieved over a 0 °C to 100 °C range. Other researchers have also used this method to compensate [39], achieving 200 ppm variation in the 25 °C to 105 °C range.

1.4.2 Passive and Active Electrostatic Compensation

In chapter 1 section 1.2.2, it was shown the act of electrostatically actuating resonators can modify the frequency of vibration. The degree to which the frequency is modified depends on the magnitude of the potential in the electrostatic gap as well as several dimensional parameters such as the electrostatic gap and area.

The ability to tune these parameters over temperature provides two methods of compensation. The most straightforward is active compensation by changing the bias voltage applied to the resonator depending on the temperature. As temperature increases, the frequency of the resonator would tend to decrease. However, if the bias voltage is decreased appropriately, making the frequency increase, the two effects can be cancelled [33]. This method was shown to reduce the frequency variation to 27 ppm in the 25 °C to 125 °C range.

Passive compensation using the electrostatic effect is possible by designing the electrostatic gap to change with temperature. At constant bias voltage, as the gap increases, the frequency increases. Hsu and Nguyen [40] developed a structure where the gap would increase with temperature such that the frequency decrease with temperature would be cancelled. This method used a silicon beam and a gold electrode. Since gold expands much more than silicon it was designed to provide large change in gap between the electrode and beam. Although the bias voltage did not change over temperature, it acts as an amplification factor. The proper magnification factor is determined by calibrating over temperature and varying bias voltages. A frequency variation of 17.8 ppm was achieved in the 25 °C to 105 °C range.

1.4.3 Active Oven-Control

Active temperature control uses a heater to maintain the temperature of the resonator at a constant elevated temperature. As previously discussed, this methodology has been applied to oven-controlled quartz crystal oscillators (OCXO). Although the OCXO achieves superb levels of frequency stability (< 0.01 ppm), the large power consumption makes the OCXO ill-suited for use in portable electronics applications. One of the biggest advantages of applying this approach for silicon resonators is the

ability to integrate the heater with the silicon resonator on the wafer. Integration would allow miniaturization of the heater as well as reduction of the power consumption by reducing the thermal mass to just the heater and resonator.

The method has been successfully demonstrated in reducing the frequency sensitivity of silicon resonators by several orders of magnitude while only using tens of milliwatts of power for heating ([68], [37], [44]). However, this level of improvement does not achieve OCXO level of frequency stability due to the high temperature sensitivity of silicon. For example, with approximately a -30 ppm/ $^{\circ}\text{C}$ temperature coefficient of frequency for silicon resonators, to achieve less than 0.01 ppm frequency variation would require temperature control of 0.0003 $^{\circ}\text{C}$. This level of control is currently not feasible with external thermometry.

1.4.4 Active Circuit Compensation

Another method for temperature compensation is to avoid changing the frequency of the resonator and to use a programmed circuit to output a “fixed” frequency. The concept is to do a pre-calibrated multiplication of the resonator’s frequency based on a temperature sensor measurement and a fractional-N phase locked loop. The advantage is that no complex control of the frequency of the resonator is needed. The method depends on a full understanding of the frequency of the resonator over temperature and the accuracy of the temperature sensor used as the input to the multiplication circuitry. As such, the accuracy of the compensation depends on the resolution and accuracy of the temperature sensor. The additional circuitry for compensation not only consumes power, but also adds noise. Two start ups focusing on commercialization of silicon MEMS resonators, SiTime [82] and Discera [25], use this type of active circuit compensation. Both companies are currently distributing MEMS resonator based oscillators with less than ± 50 ppm frequency variations over a -40 $^{\circ}\text{C}$ to 85 $^{\circ}\text{C}$ temperature range.

1.5 Contribution and Organization

In this dissertation a new passive compensation method is developed that allows silicon-based resonators to achieve comparable frequency-temperature sensitivity to quartz crystal resonators. Unlike previous passive compensation schemes, this method does not rely on the use of thermal stress induced in the resonator to temperature-compensate. The compensating mechanism is created by using materials with different temperature coefficients of Young's Modulus to create a composite structure whose overall temperature dependence is nulled. Silicon, which has a negative temperature coefficient of Young's Modulus, is combined with Silicon Dioxide, which has a positive temperature coefficient of Young's Modulus, in a manner that results in frequency-temperature insensitive resonators.

This methodology has several key advantages that make it a viable solution to the frequency-temperature problem in silicon resonators. Since the compensation mechanism is not stress dependent, the design of the resonator is not limited to just flexural mode beam resonators. Furthermore, the compensated resonators can be designed with a single anchor, thus isolating them from packaging stresses. One of the biggest advantages of this methodology is that the resonators can be designed into a previously developed and commercially proven [82] "epi-seal" process which has been shown to yield stable silicon resonators. In this dissertation, a modified "epi-seal" process is developed that results in hermetically sealed, temperature-insensitive composite resonators. The modified process retains the benefits of the "epi-seal" MEMS-first approach, such as hermetically vacuum-level sealed resonators in a CMOS-compatible process with the option of subsequent CMOS integration.

The organization of this work is as follows:

Chapter 2 develops the theory of composite resonator frequency and temperature dependence for flexural and extensional mode resonators. Several compositions of silicon and silicon dioxide are considered and the ideal geometry that will lead to "zero-TCf" resonators is developed.

Chapter 3 presents the modified "epi-seal" process which results in hermetically encapsulated silicon dioxide coated single-crystal silicon resonators. The process is

described in detail as well as major challenges that were overcome to obtain a high-yield process.

Chapter 4 presents the measured frequency-temperature behavior of three types of composite resonators: (1) a flexural mode, single-anchored, double ended tuning fork resonator (2) a flexural “wine-glass” mode ring resonator, and (3) an extensional mode ring resonator. “Zero-TCF” resonators are demonstrated in which the linear temperature coefficient of frequency is cancelled. The resulting higher order quadratic behavior is characterized.

Chapter 5 examines other important characteristics of the composite resonator such as quality factor and electrostatic transduction factor. Measurements of long-term frequency behavior at constant temperature are presented. The effects of electrostatic charging of the silicon-dioxide compensating layer are observed and discussed.

Chapter 6 returns to the subject of temperature compensation using thermal stress for silicon-only resonators. A method for inducing thermal stress as a post-processing step on the original “epi-seal” process is demonstrated. Hermetically sealed silicon resonators are temperature compensated by employing a thin film in the final metalization layer. An aluminum thin film is shown to compensate to the same level of frequency variation as the composite resonator methodology. However, thermal hysteresis in the thin film is shown to be a major drawback and stress evolution in the thin film is extracted from frequency measurements.

Chapter 7 concludes with major accomplishments and future direction.

Chapter 2

Theory of Composite Resonators

Undesirable temperature dependent frequency changes in silicon resonators are predominantly due to the negative temperature coefficient of Young's Modulus of silicon. This type of behavior is expected in resonators fabricated out of most materials currently available. As the temperature of a material increases, the average energy in the vibrational modes of the lattice increases. The relationship between energy and interatomic separation is not perfectly symmetric around the energy minimum in the interatomic potential. The asymmetry in the potential leads to an increase in the average interatomic spacing with temperature; this increase with temperature is usually described by the coefficient of thermal expansion. The dimensional change is typically accompanied by an increase in the compliance of the material, resulting in a negative temperature coefficient of Young's Modulus.

Crystalline quartz, a crystalline form of SiO_2 , is a material predominantly used in resonators for frequency references. It exhibits both positive and negative temperature coefficients of the elastic constants. This discover results in several cuts of the quartz crystal which exhibit temperature insensitive behavior. It is serendipitous that amorphous silicon dioxide, one of the most commonly used materials in the semiconductor industry, exhibits a positive temperature coefficient of Young's Modulus. Several measurements of the temperature dependence of Young's modulus of silicon dioxide have been performed starting early in the 20th century (see Appendix C) [27, 79, 81, 63, 83]. Different methods have been used to measure the temperature

dependent Young's Modulus of bulk and thin film SiO_2 . Some of the findings are through indirect measurements, and as such there is a bit of uncertainty regarding the TCE of thermally grown SiO_2 . From literature values, it is approximated that the linear TCE of silicon dioxide is approximately $183 \text{ ppm}/^\circ\text{C} \pm 29 \text{ ppm}/^\circ\text{C}$. Little information has been found about the quadratic temperature coefficient of Young's Modulus of silicon dioxide. Lynun and Torbin [61] reports values for an ultrasonically measured fused quartz rod of approximately $-137 \text{ ppb}/^\circ\text{C}^2$. Following the formulation of Chapter 1, section 1.3.2, if a resonator was manufactured out of only silicon dioxide, its linear TCf would be approximately a positive $91 \text{ ppm}/^\circ\text{C}$.

One of the earliest uses of silicon dioxide for temperature compensation was demonstrated by Parker and Schulz [73] in 1974 by sputtering a SiO_2 layer on YZ LiNbO_3 and YZ LiTaO_3 surface acoustic wave delay lines. Cambon et al. [18] demonstrated a SiO_2 compensated silicon surface acoustic wave delay line with a quadratic temperature coefficient of frequency of $45 \text{ ppb}/^\circ\text{C}^2$. Pang et al. [71] demonstrated a film bulk acoustic resonator composed of Al-ZnO-Al- SiO_2 layers with a linear temperature coefficient of frequency which varies from $-1.6 \text{ ppm}/^\circ\text{C}$ to $-0.4 \text{ ppm}/^\circ\text{C}$ over a 40°C to 110°C temperature range. Recently Shen et al. [81] and Sandberg et al. [79] suggested the use of SiO_2 to temperature compensate flexural-mode resonators.

The combination of silicon and silicon dioxide for the purpose of temperature compensation is explored in this chapter. In considering the various geometries there are several immediate concerns. Will the mismatch in the thermal expansion coefficients of these two materials result in unwanted behavior? Is the amount of oxide necessary to compensate feasible? In the interest of commercial feasibility, how does one incorporate the composite into the "epi-seal" process such that there is minimal modification of the well-established and studied fabrication process?

In the following sections, the theory of frequency and temperature dependence of a composite resonator - a vibrating device composed of multiple materials, is developed. The models are then employed to determine how to construct a resonator such that the contributions of the positive TCE material and negative TCE material are canceled to yield a zero-TCf composite resonator.

2.1 Frequency Models of Composite Resonators

2.1.1 Flexural Modes

Beginning in a similar manner as with a single material beam in Chapter 1 - Figure 2.1 shows a differential element of a generic N-material system. The coordinate system origin is placed such that y is the distance from the mid-plane of the composite beam.

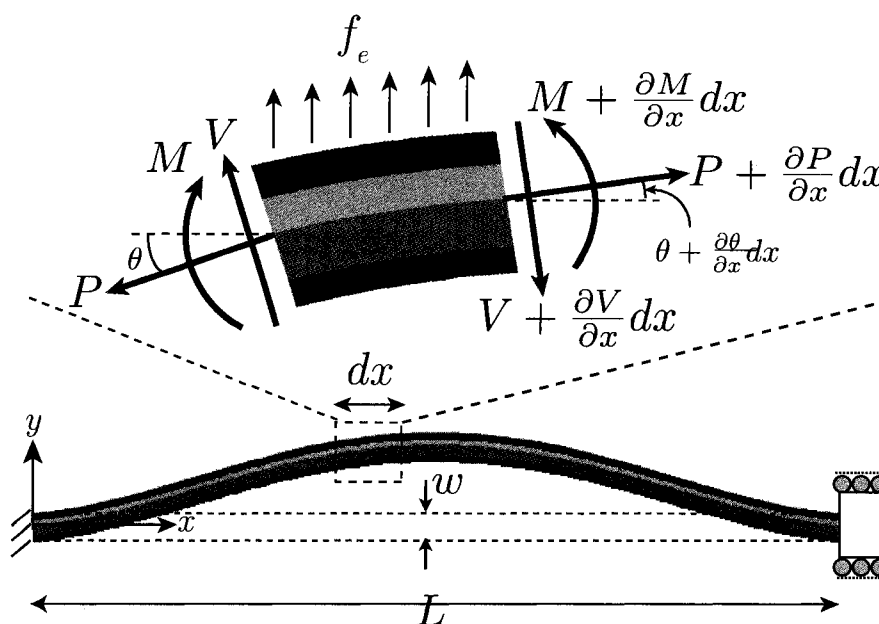


Figure 2.1: Composite flexural-mode beam and differential element of the beam.

The equation of motion for this composite system is similar to the equation of motion of a single material beam:

$$\sum_{n=1}^N \rho_n A_n \frac{\partial^2 v}{\partial t^2} + \frac{\partial^2 M}{\partial x^2} - P \frac{\partial^2 v}{\partial x^2} = f_e(v) \quad (2.1)$$

In equation 2.1, ρ_n and $A_n = wh$ are the density and cross-sectional area of the n -th layer in the composite, respectively. v is the displacement in the y -direction, t

is time, M is the resultant moment, P is the resultant axial load, and f_e is the electrostatic force on the differential element. For this composite structure the resultant axial load, P , and the resultant moment, M , are defined as:

$$P = \sum_{n=1}^N \int_{A_n} (\sigma_{xx})_n dA_n \quad (2.2)$$

$$M = \sum_{n=1}^N \int_{A_n} y(\sigma_{xx})_n dA_n \quad (2.3)$$

In equations 2.2 and 2.3, the resultant axial load and moment in the composite is the linear combination of the loads and moments carried by each layer. The integration occurs over the cross-sectional area of layer n , A_n . Due to the different coefficients of thermal expansion, it is expected that each layer will have a stress distribution of $(\sigma_{xx})_n$ where:

$$(\sigma_{xx})_n = (E_{xx})_n (\varepsilon_{xx}^{elastic})_n \quad (2.4)$$

In equation 2.4, $(E_{xx})_n$ is the Young's Modulus of layer n in the x-direction (see Appendix B), and $(\varepsilon_{xx}^{elastic})_n$ is the elastic strain in layer n in the x-direction.

In the subsequent analysis, the resultant load and moment of equations 2.2 and 2.3, will be shown to be functions of material properties and dimensions. Furthermore, the resultant load and moment will be used in the equation of motion (equation 2.1) to determine the frequency of the composite structure.

Beginning with the assumption that during in-plane vibration of the composite beam, the only non-zero stress component is the σ_{xx} along the x-direction and the other normal and shear stress components are zero. The total x-directional strain in layer n due to stretching and bending is described as:

$$\left(\varepsilon_{xx}^{total}\right)_n = \varepsilon_o + y\kappa \quad (2.5)$$

$$= \frac{\partial u_o}{\partial x} + y \frac{\partial^2 v}{\partial x^2} \quad (2.6)$$

In equations 2.5 and 2.6, $\varepsilon_o = \frac{\partial u_o}{\partial x}$ represents the stretching of the beam's mid plane ($y = 0$) and $\kappa = \frac{\partial^2 v}{\partial x^2}$ is the curvature of the beam.

The total strain in layer n is defined as the combination of elastic strain and thermal strain:

$$\left(\varepsilon_{xx}^{total}\right)_n = \left(\varepsilon_{xx}^{elastic}\right)_n + \left(\varepsilon_{xx}^{thermal}\right)_n \quad (2.7)$$

In equation 2.7, the thermal strain is the strain due only to temperature changes $\left(\varepsilon_{xx}^{thermal}\right)_n = \int_{T_o}^T \alpha_n(T) dT$ and elastic strain is the strain due to applied loads. Since the stress in the beam is dependent on the elastic strain, substituting equation 2.5 into equation 2.7 and rewriting, the elastic strain is:

$$\left(\varepsilon_{xx}^{elastic}\right)_n = \varepsilon_o + y\kappa - \int_{T_o}^T \alpha_n(T) dT. \quad (2.8)$$

The resultant axial load, P , and moment, M , can now be rewritten using equations 2.4 and 2.8 as:

$$P = \sum_{n=1}^N \int_{A_n} \left(E_{xx}\right)_n \left[\varepsilon_o + y\kappa - \int_{T_o}^T \alpha_n(T) dT\right] dA_n \quad (2.9)$$

$$M = \sum_{n=1}^N \int_{A_n} y \left(E_{xx}\right)_n \left[\varepsilon_o + y\kappa - \int_{T_o}^T \alpha_n(T) dT\right] dA_n \quad (2.10)$$

For beams that are have geometric and material symmetry about the midplane ($y = 0$), the following relationship is true:

$$\sum_{n=1}^N \int_{A_n} y \left(E_{xx}\right)_n dA_n = 0 \quad (2.11)$$

For these types of symmetric beams the resultant load and moment simplify such that there is no coupling between midplane stretching and the resultant bending moment and also between curvature of the beam and the axial load:

$$P = \sum_{n=1}^N \int_{A_n} (E_{xx})_n \left[\varepsilon_o - \int_{T_o}^T \alpha_n(T) dT \right] dA_n \quad (2.12)$$

$$M = \sum_{n=1}^N \int_{A_n} y^2 (E_{xx})_n \kappa dA_n \quad (2.13)$$

Since the curvature and material properties are not y -direction dependent quantities, equation 2.13 can further be simplified using the definition for the 2nd moment of inertia of layer n , I_n :

$$I_n = \int_{A_n} y^2 dA_n \quad (2.14)$$

$$P = \sum_{n=1}^N (E_{xx}A)_n \left[\varepsilon_o - \int_{T_o}^T \alpha_n(T) dT \right] \quad (2.15)$$

$$M = \sum_{n=1}^N B_n \kappa = \sum_{n=1}^N (E_{xx}I)_n \kappa \quad (2.16)$$

The simplified expression of the resultant moment indicates that the bending stiffness of a symmetric composite is a linear combination of the bending stiffness of each layer in composite, $B_n = (E_{xx}I)_n$

Substituting equation 2.15 and equation 2.16 into equation 2.1, the equation of motion for a differential element of a symmetric composite beam becomes:

$$\sum_{n=1}^N \rho_n A_n \frac{\partial^2 v}{\partial t^2} + \sum_{n=1}^N B_n \frac{\partial^4 v}{\partial x^4} + \sum_{n=1}^N (E_{xx}A)_n \left[\varepsilon_o - \int_{T_o}^T \alpha_n(T) dT \right] \frac{\partial^2 v}{\partial x^2} = f_e(v) \quad (2.17)$$

Special Case: A single-anchored, symmetric composite DETF

As previously discussed, a single-anchored DETF does not restrict the expansion or contraction of the vibrating beams. As such, the resultant axial load, P , must be equal to zero. The equation of motion for the differential element then becomes:

$$\sum_{n=1}^N \rho_n A_n \frac{\partial^2 v}{\partial t^2} + \sum_{n=1}^N B_n \frac{\partial^4 v}{\partial x^4} = f_e(v) \quad (2.18)$$

Ignoring the effect of electrostatics and using the solution similar to chapter 1, the natural frequency of a flexural mode composite beam is:

$$f_n = \frac{\beta^2}{2\pi} \sqrt{\frac{\sum_{n=1}^N B_n}{mL^3}} = \frac{\beta^2}{2\pi} \sqrt{\frac{\sum_{n=1}^N E_n I_n}{mL^3}} \quad (2.19)$$

where

$$m = \sum_{n=1}^N m_n = \sum_{n=1}^N \rho_n A_n L \quad (2.20)$$

There are several important properties to deduce from the frequency of the single-anchored, symmetric composite beam:

1. A mismatch in the coefficients of thermal expansion will produce a distribution of thermal stresses through the cross-section of the composite. However, since the beams are free to expand and contract, the effect of the thermal stresses is absent from the frequency behavior. This is particularly important to contrast with designs that use multiple materials to purposefully induce thermal stresses in the beams as in section 1.2.2 and 1.4.1.
2. The frequency of the composite structure depends on a linear combination of bending stiffness of each layer in the composite. The influence of the Young's Modulus of layer n on the frequency behavior is modulated by the 2nd Moment of Inertia of layer n . It is careful design of the 2nd Moments of Inertia of each layer that will allow the engineering of the final temperature dependence of the composite.

3. Under the influence of temperature changes, the symmetric composite will undergo expansion and contraction according to an effective coefficient of thermal expansion. By setting equation 2.15 to zero, the midplane strain in the beam, ε_o is found:

$$\varepsilon_o = \frac{\sum_{n=1}^N (E_{xx}A)_n \int_{T_o}^T \alpha_n(T) dT}{\sum_{n=1}^N (E_{xx}A)_n} \quad (2.21)$$

An effective coefficient of thermal expansion can be defined using equation 2.21 as $\varepsilon_o = \alpha_{eff}(T - T_o)$ where:

$$\alpha_{eff} = \frac{\sum_{n=1}^N (E_{xx}A)_n \int_{T_o}^T \alpha_n(T) dT}{\sum_{n=1}^N (E_{xx}A)_n (T - T_o)} \quad (2.22)$$

Equation 2.22 can be used to describe the changes in the length of the beam, L , in equation 2.19. We can also use equation 2.21 to determine the thermal stress in each layer as:

$$(\sigma_{xx})_n = (E_{xx})_n (\alpha_{eff}(T - T_o) - \int_{T_o}^T \alpha_n dT) \quad (2.23)$$

Flexural Mode Ring-Resonators

Flexural mode ring resonators, also referred to as wine-glass mode resonators, are also of interest due to the scalability of their frequency to higher frequency ranges. This is in part possible by scaling to smaller radii. The frequency equation, see equation 2.24, is very similar to the equation of frequency for flexural-mode beam resonators for thin rings whose radius is much larger than the cross-sectional area. In particular, the frequency of both beam and ring resonators is dependent on the bending stiffness. As such, composite flexural mode ring resonators will also depend on the linear combination of bending stiffness of each material portion in the ring.

$$f_n = \sqrt{\frac{18}{5\pi}} \sqrt{\frac{\sum_{n=1}^N (EI)_n}{mR^3}} \quad (2.24)$$

It is important to note that equation 2.24 uses an isotropic Young's Modulus. The flexural mode of a single crystal silicon ring resonator is made complicated by anisotropic elastic properties (Appendix B).

2.1.2 Extensional Modes

The frequency of composite extensional mode bar (equation 2.25) and thin ring resonators (equation 2.26) is also straight forward to develop following [76].

$$f_{bar,extensional} = \frac{1}{4} \sqrt{\frac{\sum_{n=1}^N (EA)_n}{mL}} \quad (2.25)$$

$$f_{ring,extensional} = \frac{1}{\sqrt{2\pi}} \sqrt{\frac{\sum_{n=1}^N (EA)_n}{mR}} \quad (2.26)$$

For the extensional-mode bar resonator, the axial stiffness along a particular direction in the silicon crystal is constant (Appendix B). However, for an extensional-mode ring resonator, the elastic constant changes with orientation along the ring. This effects not only the frequency of the resonator, but also the mode shape.

2.2 Temperature Dependence of Si-SiO₂ Composite Resonators

The natural frequency of the composite can be expressed as a decoupled combination of the frequencies of each portion of the beam following equation 2.19.

$$f_n = \frac{\beta^2}{2\pi} \sqrt{\frac{B_{Si} + B_{SiO_2}}{mL^3}} \quad (2.27)$$

Equation 2.27 can be rewritten as:

$$f_n^2 = \frac{m_{Si}}{m} f_{Si}^2 + \frac{m_{SiO_2}}{m} f_{SiO_2}^2 \quad (2.28)$$

This suggests that the temperature coefficient of frequency of the composite will be a combination of the temperature coefficients of each portion of the beam. Taking the temperature derivative of equation 2.28 and simplifying, we find:

$$TCf_1 = \frac{(TCf_1)_{SiO_2} + r(TCf_1)_{Si}}{1 + r} \quad (2.29)$$

where

$$r = \frac{m_{Si}}{m_{SiO_2}} \frac{f_{Si}^2}{f_{SiO_2}^2} \quad (2.30)$$

and from Chapter 1:

$$TCf_1 = \frac{1}{f} \frac{\partial f}{\partial T} \quad (2.31)$$

Considering the limits of equation 2.29, we find that in the limit as $r \rightarrow 0$, i.e. mostly a silicon dioxide beam, the $TCf_1 \rightarrow (TCf_1)_{SiO_2}$. In the limit as $r \rightarrow \infty$, i.e. mostly a silicon beam, $TCf_1 \rightarrow (TCf_1)_{Si}$.

Equations 2.28 through 2.30 are valid for flexural-mode and extensional mode resonators. Since the ratio, r , is set by the geometry of the resonator, evaluating equation 2.30 yields different expressions for flexural mode and extensional mode:

$$r_{flexural} = \frac{B_{Si}}{B_{SiO_2}} = \frac{E_{Si} I_{Si}}{E_{SiO_2} I_{SiO_2}} \quad (2.32)$$

$$r_{extensional} = \frac{E_{Si} A_{Si}}{E_{SiO_2} A_{SiO_2}} \quad (2.33)$$

The value of r will modulate the temperature dependence of the beam to exhibits behavior between that of a silicon or a silicon dioxide beam. Since the two materials have temperature dependencies with different signs, by choosing r appropriately, the temperature coefficient of frequency for the composite beam can be nulled. Setting the linear temperature coefficient of frequency (TCf_1) in equation 2.29 to zero and

solving for the ideal ratio, r^* :

$$r^*(T) = -\frac{(TCf_1)_{SiO_2}}{(TCf_1)_{Si}} \quad (2.34)$$

Due to the uncertainty of the temperature coefficient of Young's Modulus of silicon dioxide, the ideal ratio at 25 °C is between 2.5 and 3.5. Since $(TCf_1)_{SiO_2}$ and $(TCf_1)_{Si}$ are just a function of material properties, the ideal ratio depends only on the material properties of silicon and silicon dioxide. Note, however, that the material properties change with temperature. As such, the ideal ratio is different at different temperatures. The implication is that since the geometry of the resonator sets the ratio, the linear temperature coefficient of frequency can only be set to zero at a specific temperature.

Different constructions of silicon-silicon dioxide composites is explored to determine which would achieve the ideal ratio with the lowest thickness of silicon dioxide. The purpose being that minimization of the thickness of silicon dioxide would reduce thermal stresses during resonator fabrication and thus reduce processing failures.

Figure 2.2 shows possible constructions for a symmetric Si-SiO₂ composite with a rectangular cross-section. The width (w) and height (h) are chosen such that the area for the silicon portion of the beam is constant ($A_{Si} = hw$). The ideal thickness of silicon dioxide, t^* , to yield a "zero-TCf" resonator for both extensional mode and flexural mode resonators in Figure 2.2 can be found by solving for $r=r^*$ using equations 2.34 and 2.32 or 2.33, respectively. The ideal thickness for a beam resonator of height $h = 20\mu m$ for the various constructions is shown in Figure 2.3. As a rule of thumb, a r^* value of 3 was used to determine ideal thickness.

Depositions and thermal growth of silicon dioxide of more than 1 μm thickness is generally impractical because it is time consuming and could cause significant thermal stresses during fabrication. From Figure 2.3, several constructions cannot be used due to this constraint. The most effective use of silicon dioxide compensation is for a beam in flexural mode which is completely coated (construction A in Figure 2.2). A 10 μm wide flexural-mode beam can be compensated with less than 1 μm of

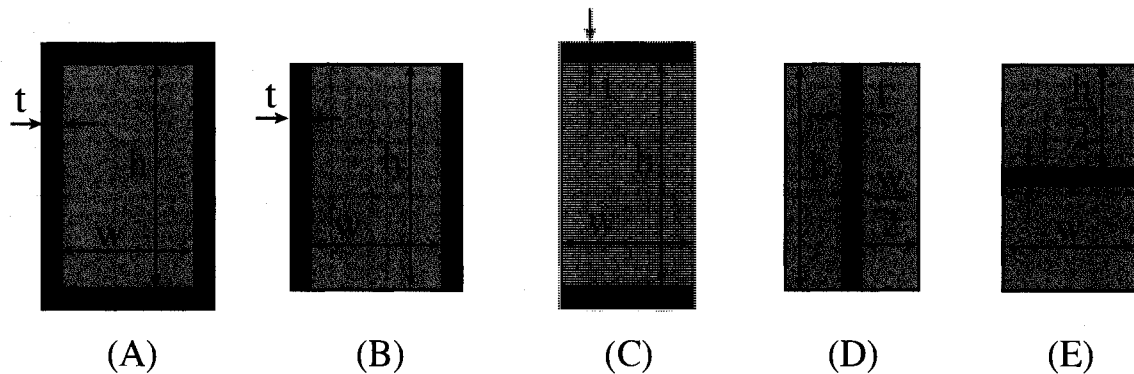


Figure 2.2: Possible constructions for symmetric Si-SiO₂ composites with rectangular cross-section areas.

silicon dioxide. Only very thin, less than $3\mu\text{m}$ wide beams, can be compensated when a coated construction is used in the extensional mode. Note that for constructions C and E in 2.2, the ideal silicon dioxide thickness is the same when operated in flexural or extensional modes. Furthermore, constructions B and D are independent of the height (h).

The coated geometry is ideal since it is also straightforward to fabricate using thermal oxidation. Thermal oxidation allows the formation of high quality silicon dioxide that is also very uniform. The uniformity of thermal growth allows the creation of symmetric composites and reduces variation over the wafer. However, thermal oxidation also results in slightly different growth rates of silicon dioxide on different single crystal silicon crystal plane orientations [75]. This must be taken into account since the thickness of oxide is a critical parameter.

2.3 Summary

In this chapter we developed the theory of vibration and temperature dependence of vibration for symmetric composite resonators. The main motivation was to design a temperature insensitive resonator by using silicon and silicon dioxide, since these two materials have opposing temperature coefficients of Young's Modulus. It was found that the temperature coefficient of frequency of the composite is a weighted

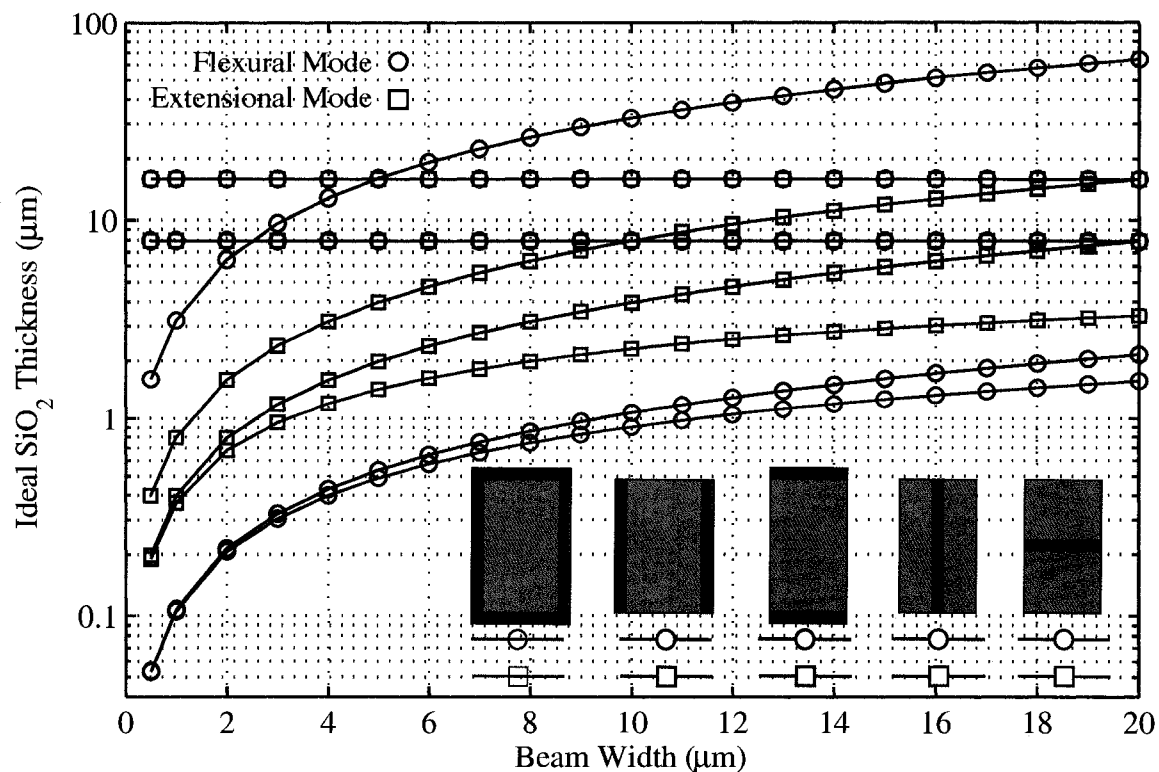


Figure 2.3: Ideal SiO₂ thickness for extensional mode and flexural mode vibrations of constructions shown in Figure 2.2. A height of $h = 20\mu m$ is used.

linear combination of the temperature coefficients of frequency of the silicon portion of the beam and the silicon dioxide portion of the beam. The weighting factor, r , is a non-dimensional ratio that depends on the mode of operation, material properties, and dimensions of the resonator. However, the ideal ratio, r^* , needed to achieve a “zero-TCF” resonator depends on the temperature coefficients of Young’s Modulus of silicon and silicon dioxide.

For a given resonator geometry and mode of vibration, the thickness of oxide necessary to achieve a “zero-TCF” resonator can be found by solving for $r = r^*$. It was found that the most effective way to achieve this compensation is to use a silicon beam coated with silicon dioxide and operated in flexural mode. The use of a thermally oxidized double-ended tuning fork resonator, described in Chapter 1, is a straightforward implementation of this type of compensation. In the next chapter

the fabrication of this composite resonator is described.

Chapter 3

Fabrication of Composite Resonators

Silicon micromachining has the extraordinary capability to create large volumes of precisely defined structures with sub-micrometer precision. However, the advantages of exquisitely small features can be offset by failure or capability loss due to interaction with other small scale effects. Dust, contamination, radiation, and human handling are just some of the mechanisms that can cause failure and drive the need for high quality packaging in micromechanical systems.

Frequency references have the most stringent packaging requirements. Very small changes in mass or stiffness of the resonator can cause large frequency changes. Furthermore, low pressure packaging is needed to decrease air-damping and increase the quality factor of the resonator; especially for flexural mode resonators. The rise of the quartz crystal frequency reference is largely due to the development of highly hermetic packaging methods. Quartz crystal resonators are individually packaged in a metal cans which are vacuum sealed. The low cost through batch fabrication and CMOS integration advantages of silicon resonators would be lost if silicon resonators needed to be packaged similarly to quartz crystal resonators. For this reason, the study of wafer-level packaging techniques has received a great deal of attention.

One successful packaging method is the result of a collaboration between Stanford University and Bosch Research and Technology Center (RTC) in Palo Alto, CA. The

inventors developed an epitaxial silicon thin film, “epi-seal,” encapsulation technology that allowed the resonator to be packaged at the wafer-scale in a hermetic, low pressure environment [50], [22]. The encapsulation technology used a MEMS-first approach briefly described in Chapter 1, Section 1.2. The final packaged devices have a small footprint, were only exposed to CMOS-compatible processing, and have areas of single-crystal silicon to be used for CMOS integration. Using this approach, [50] showed that pressure-sensitive resonators packaged using this technology were stable to within ± 3.1 ppm at room temperature over the period of one year. Solving this critical bottleneck for silicon frequency references spawned SiTime Inc [82], a start-up in Sunnyvale, California focusing on commercialization of silicon frequency references.

The fabrication and packaging of composite resonators is derived from the “epi-seal” technology developed for silicon resonators. This chapter describes the fabrication and “epi-seal” encapsulation of composite “zero-TCf” resonators.

3.1 Thin-film Epi-Seal Fabrication of Composite Resonators

Flexural-mode double-ended tuning fork resonators, as shown in Chapter 1, with varying beam widths were designed. Since there is a large uncertainty in the ideal bending stiffness ratio that would yield a “zero-TCf” resonator, the ratio was set by designing DETF resonators with beam widths varying from $4 \mu\text{m}$ to $8 \mu\text{m}$ in steps of $0.25 \mu\text{m}$. The composite structure was formed by thermally oxidizing the silicon DETF and forming a coating of silicon dioxide of similar thickness on all of the resonators.

3.1.1 Pre-processing

The fabrication begins with a 4 inch diameter single-crystal silicon on a silicon dioxide insulator (SOI) wafer (see Figure 3.1). The wafer is annealed at 1000°C for approximately 24 hours to anneal stresses in the buried silicon dioxide (BOX) insulator layer.

Alignment marks are etched into the surface of the wafer to provide alignment features for the subsequent lithographic steps performed on both stepper and contact mask aligners. Stepper aligners are used because they provide higher resolution lithography. The ASML PAS 5500 stepper can expose features that are as small as $0.4 \mu\text{m}$. Contact aligners are used when features exceed $2 \mu\text{m}$.

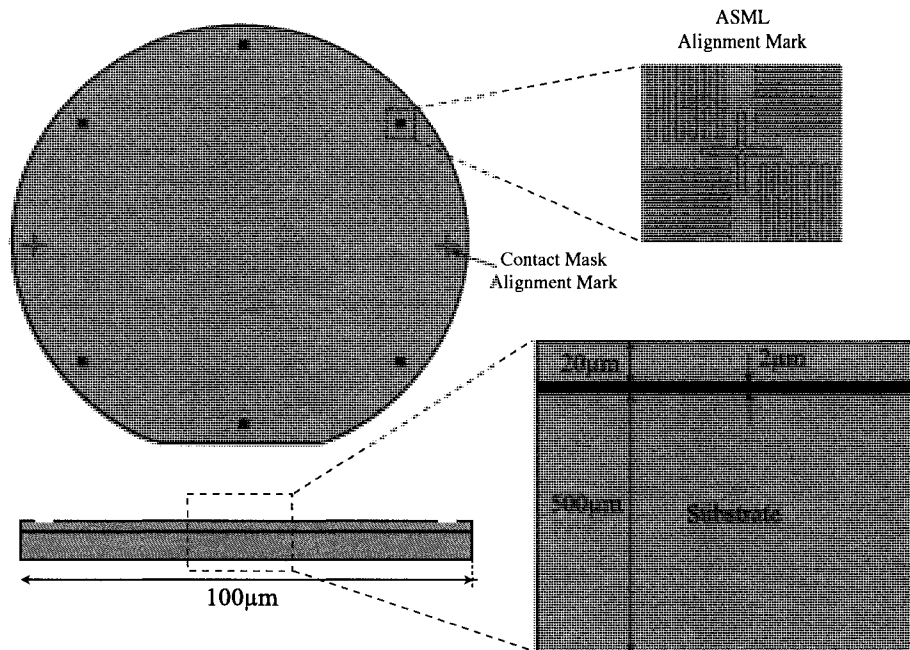


Figure 3.1: Schematic of silicon on insulator (SOI) wafer with alignment marks.

3.1.2 Device Definition

A stepper aligner is used to define the double-ended tuning fork resonator in $1 \mu\text{m}$ of Shipley 3612 photoresist. The desired trench size is $1.5 \mu\text{m}$ and will form the electrostatic gap between the resonator and the electrodes (Figure 3.2). Using the Bosch deep reactive ion etch (DRIE) in an STS etcher, the trenches are etched in the $20 \mu\text{m}$ device layer of the SOI. The Bosch DRIE recipe is used to avoid “footing” problems during an overetch in which plasma ions are deflected from the BOX layer and begin etching sideways into the silicon at the bottom of the trench. A 20%

overetch is done to ensure that all trenches reach the buried silicon dioxide layer.

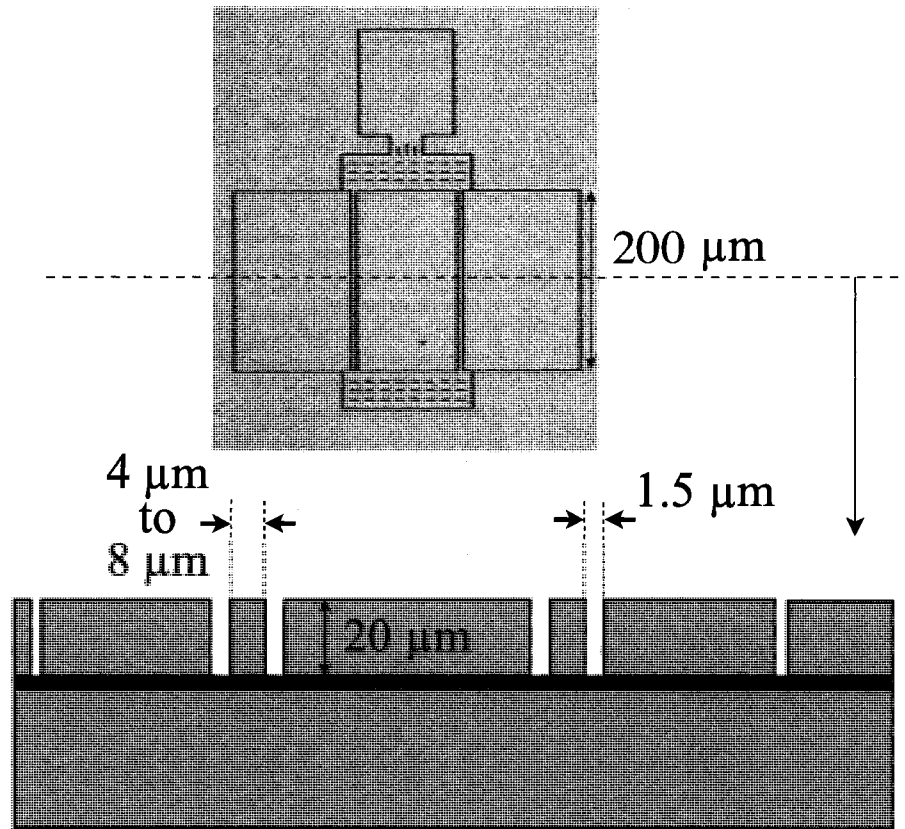


Figure 3.2: (Top) Microscope image of definition of DETF. (Bottom) Schematic of cross section showing two beams between electrodes.

The sidewalls of the trenches that are formed are typically not perfectly parallel. There are several topographical features left by the DRIE etch. The trench is usually wider, which is known as “blow-out”, at the surface of the wafer and tapers toward the buried oxide. There are also “scallops” that are left by the etch-passivation cycle which is common to the Bosch DRIE recipe. SEM measurements of beam widths after DRIE indicate that the width shrinks on average by $0.3 \mu\text{m}$ and has approximately $0.09 \mu\text{m}$ variation across the wafer.

3.1.3 Sacrificial Release Layer

Sacrificial tetraethyl orthosilicate (TEOS) silicon dioxide is deposited in three to four steps with approximately $0.7 \mu\text{m}$ to $0.8 \mu\text{m}$ deposited in each step. After each deposition the silicon dioxide is annealed for 1 hour at 1100°C to relieve stresses and densify the silicon dioxide. If more than $1 \mu\text{m}$ is deposited in one step, the residual stresses in the oxide cause cracking in the thin film. TEOS is used for its conformal deposition with the goal of sealing the trenches with the least amount of oxide. It is desirable to match both the thickness and density of this layer with the buried silicon dioxide layer. After this step the buried silicon dioxide and the TEOS completely surround the resonator beam (Figure 3.3). Both of these layers are sacrificial and will be removed to allow the resonator to vibrate.

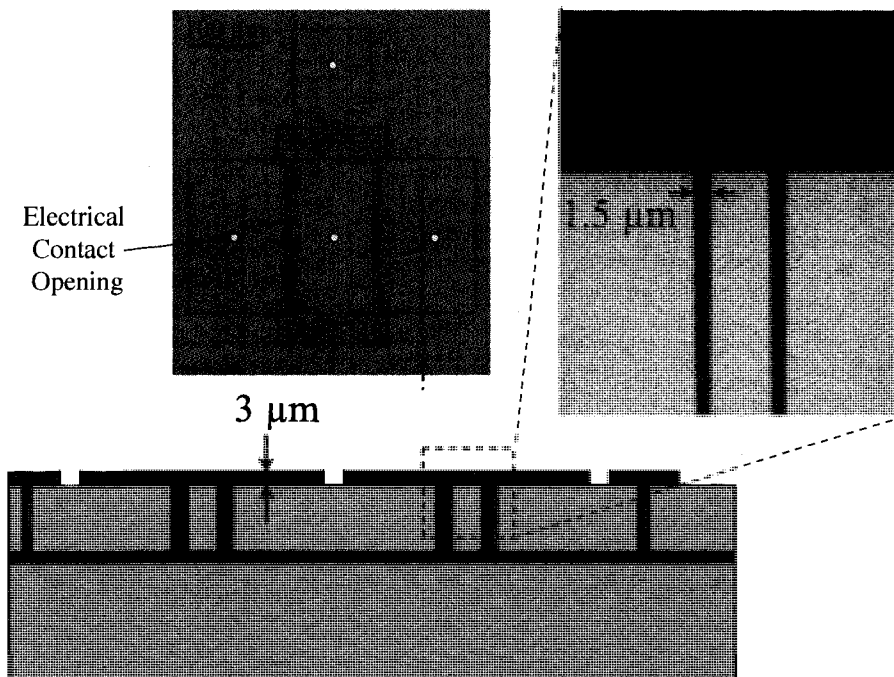


Figure 3.3: (Top-Left) False color microscope image of TEOS re-fill of definition trenches and openings for electrical contact. (Top-Right) False color microscope image of cross-section of definition trench refilled with TEOS sacrificial silicon dioxide. (Bottom) Enlarged cross section schematic.

If a less conformal deposition technique is used, such as low temperature silicon dioxide (LTO) deposition, the thickness of the deposition to seal the trenches would be more as LTO does not deposit on the sidewalls of the trench. To further decrease the thickness of the TEOS deposition, only T-intersections of trenches are allowed. Acute intersections or cross intersections could “blow-out” during lithography and result in larger trenches to re-fill. In addition, the trench is not perfectly re-filled during TEOS deposition. Although silicon dioxide is deposited on the sidewalls of the trenches, a small opening, known as a “key-hole”, is left through the center of the trench.

After deposition, small openings are etched through the TEOS with an AMAT p5000 reactive ion etcher for electrical contacts to the resonator and electrodes. In Figure 3.3, one opening is over the anchor of the resonator. This contact will provide the bias voltage to the resonator. The three other contacts are for the electrodes to provide the input AC voltage and the center electrode contact to measure the resonator response. A contact can also be placed in the field area away from the electrodes and resonator. This contact could be used to bias the device layer and is typically set to ground.

3.1.4 Epitaxial Silicon Encapsulation

This step begins the wafer-scale encapsulation of the resonator. Epitaxial silicon is deposited over the entire wafer at 1080 °C in an AMAT epitaxial reactor. The growth of silicon on top of silicon dioxide results in a layer of polycrystalline silicon. However, the opening in the TEOS sacrificial oxide exposes the single-crystal silicon of the device layer. Silicon growth in the TEOS openings aligns with the underlying crystal and results in growth of single-crystal silicon. If large areas of single-crystal silicon are open away from the resonator-electrode structure, the large area of single-crystal silicon provides an area for subsequent CMOS-integration. The deposited silicon is n-doped to match the doping of the device layer.

Approximately 20 μm of epitaxial silicon is deposited, forming the “1st cap”. This deposition is ten times thicker than the first encapsulation layer deposition of Candler

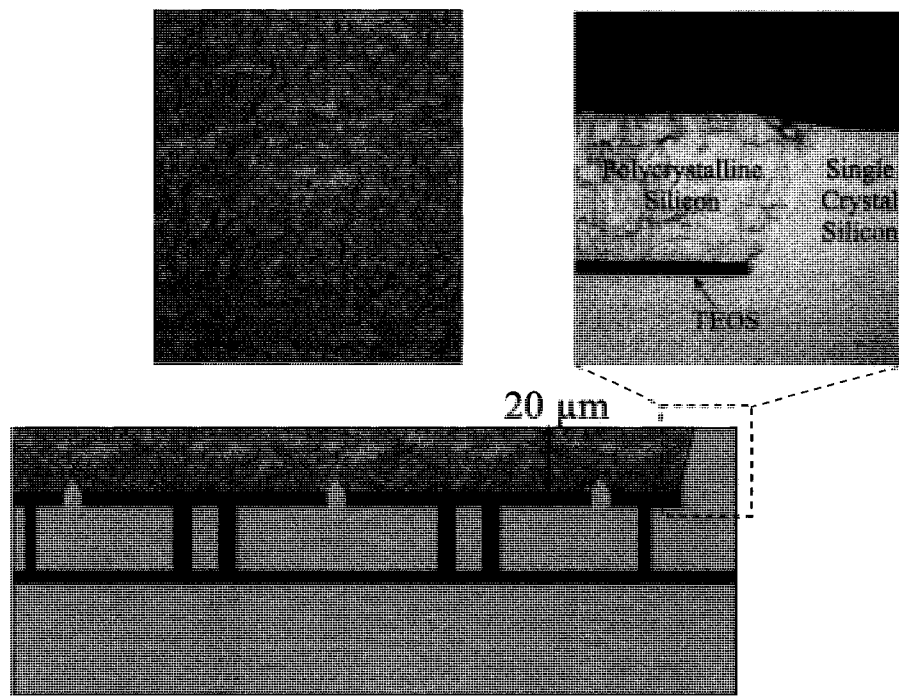


Figure 3.4: (Top-Left) True color microscope image of polycrystalline silicon. (Top-Right) True color microscope image of cross-section of first cap showing polycrystalline and single-crystal epitaxial growth. (Bottom) Enlarged cross section schematic.

et al. [22] to add structural stability during composite formation.

The polycrystalline deposition tends to be rough (see top of Figure 3.4) and thicker than the single-crystal silicon growth. A chemical-mechanical polishing (CMP) step is performed to planarize the surface. This is necessary for two reasons: (1) to planarize the surface to improve subsequent lithography steps, and (2) to reduce infrared (IR) light scattering from rough surfaces when using an IR microscope to monitor device release in the next step. In the original “epi-seal” encapsulation process, this CMP step was not necessary since the difference in thickness of the polycrystalline and single-crystal growth in a $2\ \mu\text{m}$ layer is significantly less.

3.1.5 Device Release

The resonator is now buried under an epitaxial silicon layer and is surrounded by sacrificial silicon dioxide (buried silicon dioxide and TEOS). To release the resonator the sacrificial silicon dioxide around the device must be removed. Small openings in the encapsulation layer, also called “vents”, are etched to provide access to the sacrificial SiO_2 . Vents are typically arrayed holes of $1 \mu\text{m} \times 8 \mu\text{m}$ defined over the resonator in the encapsulation layer (Figure 3.5).

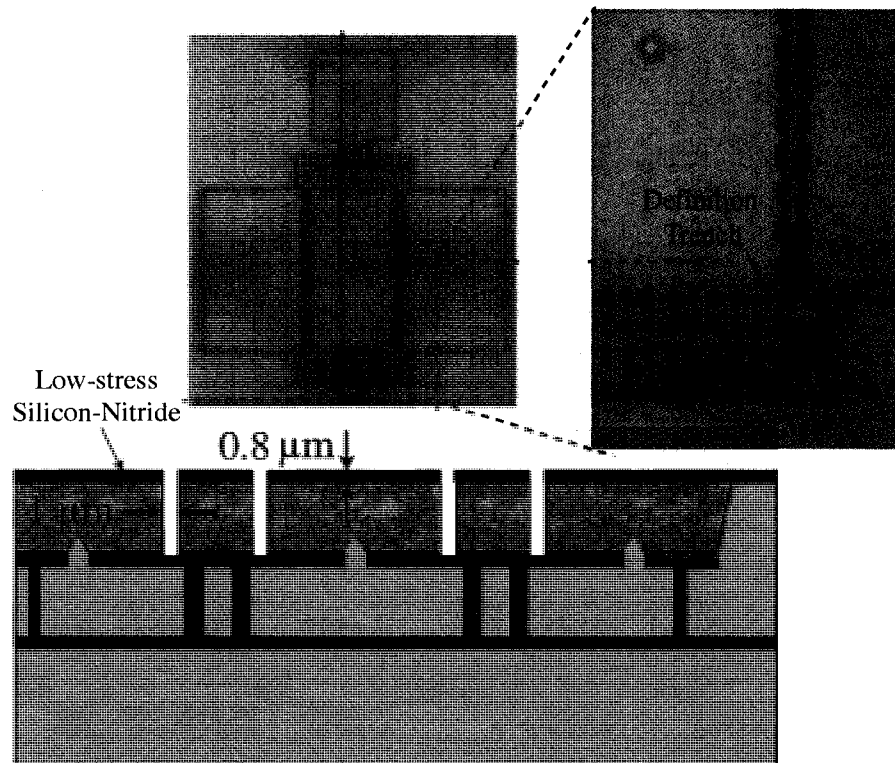


Figure 3.5: (Top-Left) False color IR microscope image of vents and definition layer. (Top-Right) False color higher magnification IR microscope image showing vent and definition trenches. (Bottom) Enlarged cross section schematic.

There are two additional steps prior to the lithographic patterning of the vents. The “vent” mask must be aligned to the now obscured device layer. Two of the six ASML alignment marks are opened by silicon DRIE etching of small holes over the

alignment marks. Note that the alignment marks are protected during this step as they are etched into the silicon device layer and are covered by silicon dioxide during the TEOS trench-refill step. A low-stress silicon nitride of approximately $0.8 \mu\text{m}$ is also deposited. The silicon nitride is useful during the composite formation step as it inhibits growth of silicon dioxide of the encapsulation epitaxial polysilicon on the surface of the wafer (see section 3.1.6). This is typically done during a local oxidation (LOCOS) process [19].

A stepper must be used to lithographically pattern the $1 \mu\text{m}$ vents. The Bosch DRIE process described in the device definition section is used to etch the vents. The etch stops on the TEOS sacrificial oxide. Since wet etching of the sacrificial silicon dioxide could result in stiction, the oxide is etched using vapor hydrofluoric acid with an etch rate of approximately 500 angstroms per minute.

The progression of the etch is obscured by the thick silicon encapsulation. Since silicon is transparent to IR wavelengths, an IR microscope is used to monitor the progress of the etch (Figure 3.6). The TEOS is etched first and an etch-front can be seen using the IR microscope. As the vapor HF reaches a trench, the vapor acid quickly reaches the buried oxide due to the “key-hole” openings from the imperfect conformality of the TEOS deposition. The time delay between etching the TEOS sacrificial oxide and the buried silicon dioxide results in two visible etch fronts. Both etch fronts are monitored during the release, however it is the buried silicon dioxide etch that must be completed to ensure full release of the resonator. Note that the silicon nitride deposited will also etch in hydrofluoric acid although at a much slower rate of 35 angstroms per minute. Since the silicon nitride must be present during the next step, a thick layer of $0.8 \mu\text{m}$ was initially deposited.

Overetch during the release step can be disastrous to the process. As the vapor HF is transported in the “key-holes” of the trenches, the TEOS oxide around the resonators’ anchor and electrodes is also etched. Toward the end of the process, once the resonators are sealed in a low-pressure cavity, the electrical contacts will need to be isolated from each other using a DRIE step. The DRIE step must stop on the deposited TEOS layer. However, if the TEOS deposition is etched during this

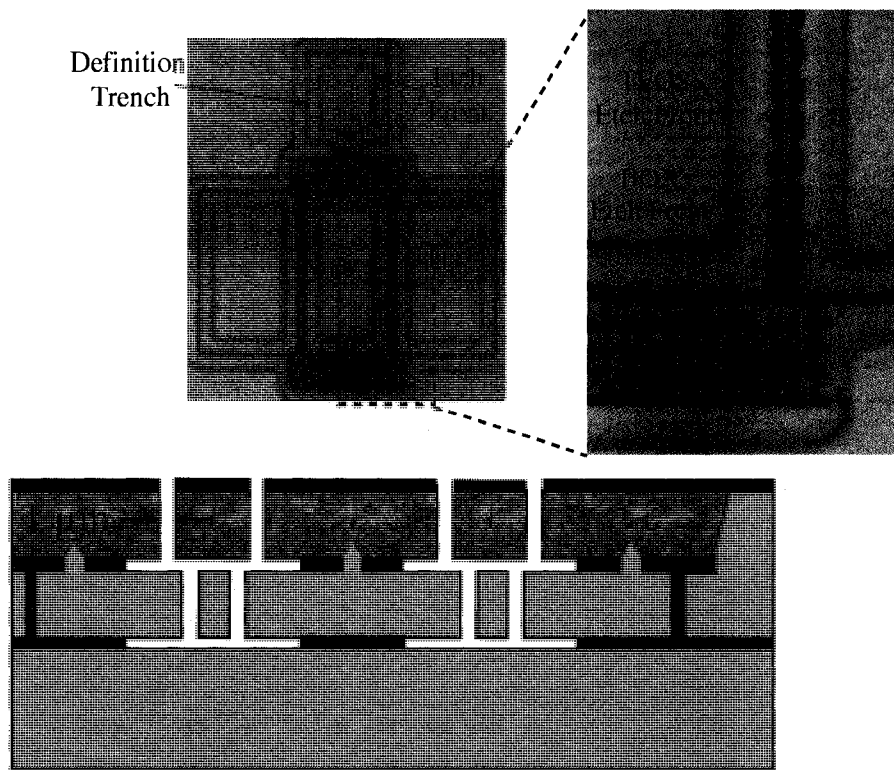


Figure 3.6: (Top-Left) False color IR microscope image of vents, definition trench, and vapor HF etch front. (Top-Right) False color higher magnification IR microscope image showing TEOS etch front and buried silicon dioxide (BOX) etch front. (Bottom) Enlarged cross section schematic.

release step, the DRIE etch will break into the vacuum cavity of the resonator, thus exposing the resonator to environmental conditions (see section 3.1.8). The size of the anchor and electrodes must be carefully chosen such that during the release of the resonator the etch front does not encroach on the electrical contacts in the anchor and electrodes.

Another design consideration is the placement of the vents. Since the release must be carefully controlled, the etch front, including an overetch, is limited to approximately $10\ \mu\text{m}$ from the vent. This places additional restrictions on the size and design of the resonator. For example, the coupling beams in the DETF (see Figure 3.2) are perforated. Vents are designed to overlay the perforation to help transport vapor HF

etchant to the underside of the coupling beam and thus the buried silicon dioxide. The beams of the resonator do not need to be perforated as long as they are less than $10\ \mu\text{m}$ to $12\ \mu\text{m}$ in width. In this case, the trenches defining the beam are sufficient to transport the vapor HF to the buried silicon dioxide.

In the “epi-seal” of silicon resonators, the vents are usually overlaid with beam trenches in the device layer such that the vent is perpendicular to the trench. In this modified process, the vents are positioned parallel to the trench and $1\ \mu\text{m}$ away from the trench on the side of the electrode. In Section 3.2 on fabrication challenges for composite resonators, we will see that positioning vents over the beam has several negative consequences, such as loss of composite symmetry and plasma damage.

The second restriction is on the total span of the released area. Over large perforated areas, such as over the coupling beams, the encapsulation acts a membrane over the released area. The size of the membrane area had to be restricted to $150\ \mu\text{m}$ by $300\ \mu\text{m}$. The restriction was necessary to minimize deflection due to thermal and residual stresses during composite formation. As we will see in the next section, stresses during growth of thermal silicon dioxide could cause a large deflection of this membrane. It is for this purpose that the area of the released membrane is limited and the thickness of the membrane (i.e. first encapsulation) was increased.

3.1.6 Composite Formation

After release of the silicon resonator, the vent holes could be sealed using epitaxial silicon deposition (as will be described in section 3.1.7) similar to the original silicon resonator “epi-seal” process. However, before sealing, thermal oxidation is used to form the composite.

Dry or wet thermal oxidation can be used to form the composite (Figure 3.7). Dry thermal oxidation can take multiple hours, but generally forms silicon dioxide with less defects [75]. Wet thermal oxidation is much faster, growing $0.5\ \mu\text{m}$ in less than one hour. The oxidation time was calculated using the Deal-Grove model ([75]) and fine tuned using test runs. During thermal oxidation every exposed silicon surface will grow thermal oxide. This includes growing thermal oxide on the beams, the

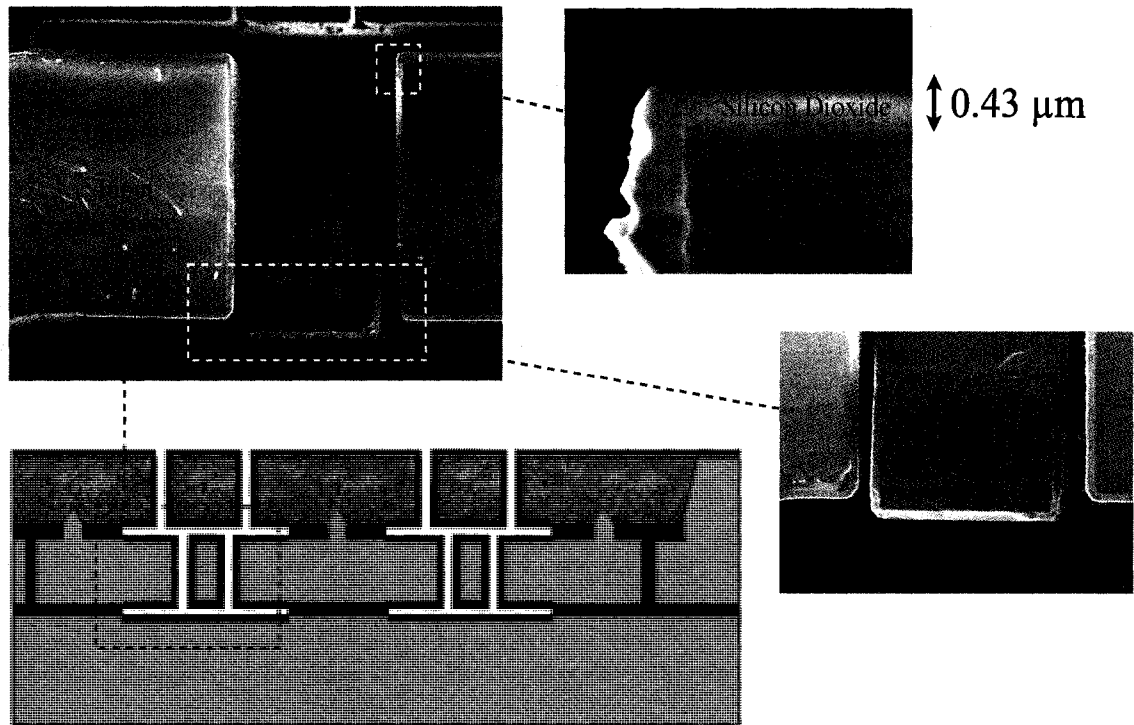


Figure 3.7: (Top-Left) Scanning electron microscope (SEM) image of cross section of resonator beam. (Top-Right) SEM image of corner of electrode showing large variation in silicon dioxide thickness on sidewalls. (Right) SEM image of bottom of the composite beam. (Bottom) Enlarged cross section drawing.

electrodes, and every surface in the cavity. However, the growth on the $\langle 110 \rangle$ plane will be more than on the $\langle 100 \rangle$ plane due to more exposed silicon atoms on the $\langle 110 \rangle$ surface [75]. Since the resonator is buried beneath the encapsulation layer, it is impossible to get a direct measurement of the silicon dioxide grown on the beam. The best approximation is to use a test wafer that follows the resonator through the process. The $\langle 100 \rangle$ silicon dioxide thickness measurement was taken on the test wafer using a Nanospec AFT Model 010-180. The variation in the oxide thickness across the wafer had a standard deviation of less than 50 angstroms. An SEM of a broken test wafer revealed that the oxidation on the top and bottom of the beam is identical within the measurement error. This indicates that thermal oxidation can be used to form a symmetric composite. However, the scallops formed on the trench

sidewalls during DRIE etching were visible after oxidation (see top right of Figure 3.7). The thickness of the sidewall oxide is difficult to determine because of both variation along the sidewall as well as not having direct access to the actual resonators tested. Furthermore, charging of the oxide during scanning electron microscope investigation complicates making a precise measurement.

At the time of oxidation, several microns of silicon dioxide are present on the backside of the wafer from the initial SOI and TEOS depositions (not shown in the schematics). Because of this thick oxide, the backside of the wafer will not see significant oxide growth during the thermal oxidation of composite formation. To avoid wafer bending from a mismatch in silicon dioxide on the front and back of the wafer, silicon nitride was deposited as described in the previous section. Silicon nitride effectively limits diffusion of oxygen and reduces growth of silicon dioxide on the top surface of the wafer.

However, to seal the vent holes after thermal oxidation, the silicon nitride, an electrical insulator, must be removed. Silicon nitride is etched using an AMAT p5000 reactive ion etcher. It was discovered that this etch attacks the silicon dioxide in the cavity directly under the vent. Since this caused problems during the sealing of the resonator (see section 3.2), the composite formation step was broken into two oxidations. The majority of the composite thermal oxide is grown during the first oxidation step. The silicon nitride is then etched with an overetch using AMAT p5000 etcher. A second thermal oxidation grows 1000 Angstroms of oxide. This adds to the total thickness of the composite, however only 1000 angstroms is grown on the top surface of the wafer. A carefully timed dry reactive ion etch is used to remove the thin layer of oxide on the surface. Since the film is thin, this precise etch can be optimized such that the etch is stopped before the silicon dioxide in the cavity is etched.

3.1.7 Epitaxial Sealing

Epitaxial sealing of the vents follows the process for “epi-seal” of silicon resonators. Hydrogen gas at 1080 °C flows through the epitaxial deposition reaction chamber.

This ensures that all organics are removed. In the original “*epi-seal*” process, this step removes the native silicon dioxide on the resonator’s surface, leaving a pristine silicon surface. However, a negligible amount of silicon dioxide is removed from the composite resonator.

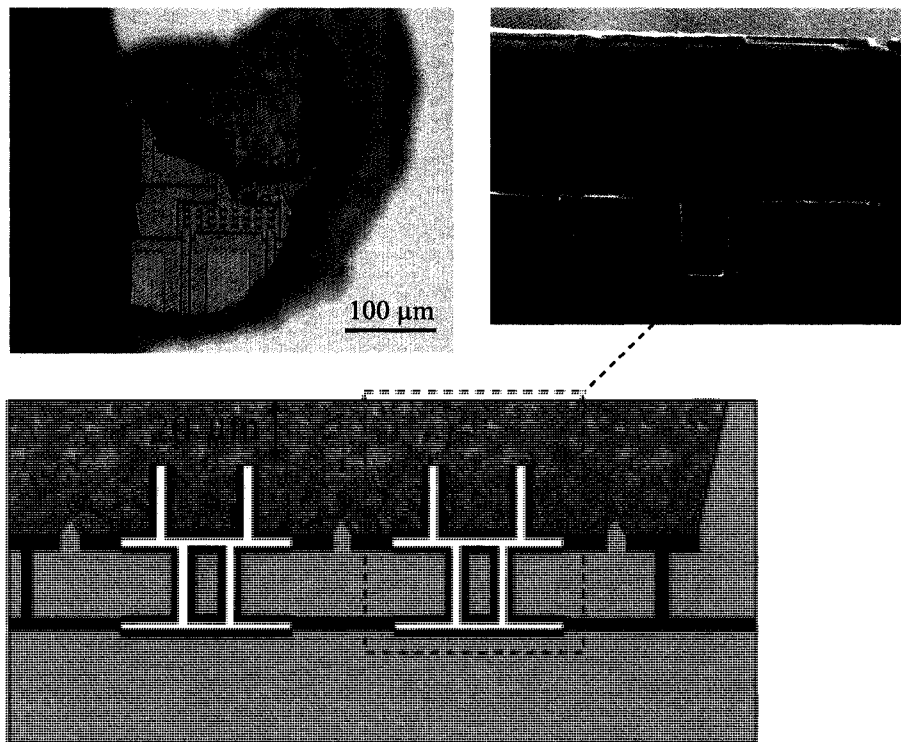


Figure 3.8: (Top-Left) True color microscope image of silicon resonator with a broken encapsulation layer. The resonator appears pink due to the $0.43 \mu\text{m}$ oxidation. (Top-Right) SEM image of cross-section of composite resonator through the beam and encapsulation layer. (Bottom) Enlarged cross section schematic.

A selective epitaxial silicon deposition on silicon, and not silicon dioxide, is used to seal the vents. Selectivity is achieved by flowing hydrochloric (HCl) acid during the sealing step [7]. Silicon that is deposited on silicon dioxide is etched away by the HCl. As silicon is grown on the top surface of the wafer, the vents are sealed. There is an advantage to having the resonator and resonator cavity completely coated in silicon dioxide during the sealing step. Since no silicon is deposited on the resonator,

the risk of shorting the resonator to the electrode due to cavity deposition is negated. In “epi-sealing” silicon resonators, this is a common failure mode. It is for this reason that the vents are usually designed to be smaller than the definition trench width. In the “epi-seal” of composite resonators, this is not necessary.

A total of 20 μm is deposited to seal the vents and provide additional structural integrity to the encapsulation (Figure 3.8). The silicon deposition is also highly n-doped to match the doping of the SOI wafer. The doping is necessary to reduce electrical resistance since the electrical interconnects will be formed through the encapsulation. Hydrogen is used as a carrier gas for the dopant. When the vents are sealed, the primary gas left in the resonator cavity is hydrogen. This hydrogen gas will be diffused through the encapsulation in the last step in the process. Epitaxial silicon sealing provides an exquisitely clean environment for the resonator and forms a hermetic package by having a thick layer of epitaxial silicon, which is a good diffusion barrier to molecules in the environment.

As during the formation of the 1st encapsulation layer, epitaxial silicon deposition will grow polycrystalline silicon on top of polycrystalline silicon and single-crystal silicon (SCS) on top of single-crystal silicon. Large areas of SCS are still available for integration with CMOS after processing. As before, the difference in the growth of polycrystalline silicon and SCS necessitates a second chemical mechanical polishing step to level the surface of the wafer.

3.1.8 Electrical Interconnect Formation

After the “epi-seal,” the resonator is hermetically sealed in a cavity under the surface of the wafer. It is remarkable to note that after the CMP step, the wafer appears as if it were a clean brand-new wafer, although not all areas are SCS. At this point, the electrical contacts to the resonator and electrodes are shorted together through the encapsulation layer. The electrical contacts must be separated by etching “isolation posts” into the encapsulation layer around each contact (Figure 3.9). This step is complicated by several factors: (1) the alignment marks are once again obscured by the encapsulation layer, (2) alignment of the isolation trench layer lithography

is crucial, and (3) a DRIE etch of the isolation posts must etch through $40\ \mu\text{m}$ of epitaxial silicon with an aspect ratio of more than 20:1. To accomplish the high aspect ratio etch, a thin $0.3\ \mu\text{m}$ silicon dioxide hard mask is deposited to avoid “mouse-bites” during the subsequent $40\ \mu\text{m}$ Bosch DRIE etch. Mouse-bites are due to breakdown of the photoresist near a trench which results in locally wider trench openings.

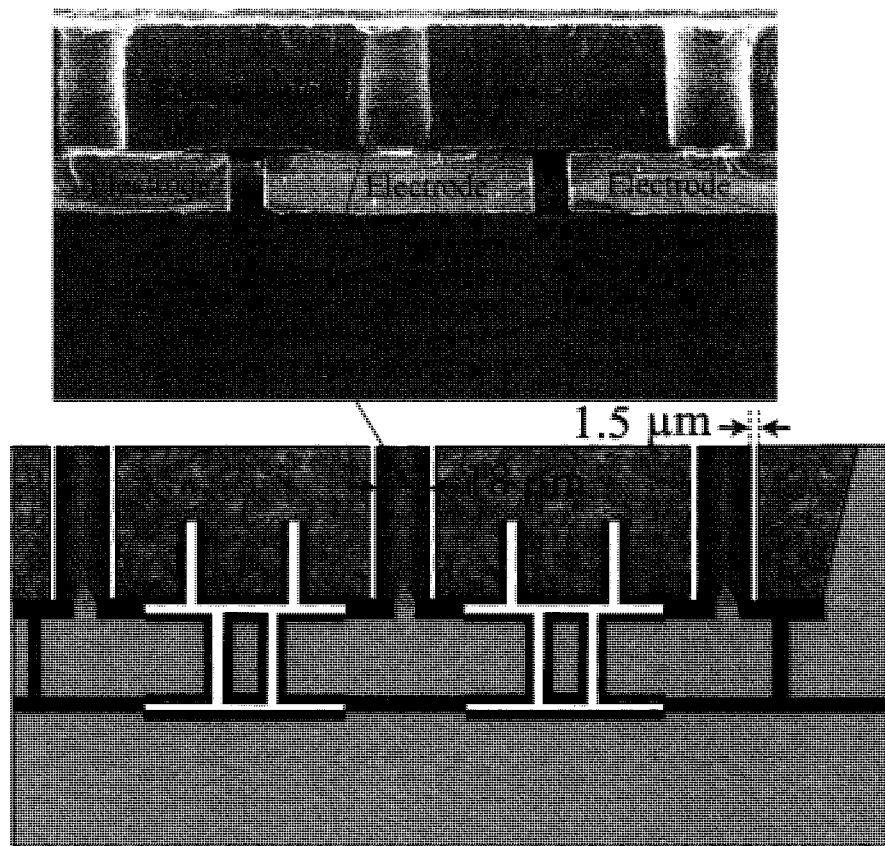


Figure 3.9: (Top) SEM showing cross section of device with three isolation posts making contact to three electrodes in the DETF resonator design. (Bottom) Enlarged cross section schematic.

Following the procedure in section 3.1.5, small openings are made over the two ASML alignment marks using a blind-align lithography step and DRIE. A blind-alignment uses only the location of the wafer flat to align the wafer. However, if a contact aligner must be used, openings of the alignment marks must be done using

a contact aligner with an IR microscope. The IR microscope is necessary to see through the encapsulation at the alignment marks in the definition step. Alignment of the isolation post mask is critical. The isolation post must completely surround the contact made after the trench TEOS re-fill step (see section 3.1.3). Furthermore, the DRIE etch must stop on the TEOS sacrificial oxide layer. If during the release of the resonator, the TEOS sacrificial oxide is severely overetched, the isolation post will not stop on the TEOS. Instead it will break into the resonator's cavity, which was "epi-sealed," causing an irreparable critical failure since the resonator would then be exposed to the environment.

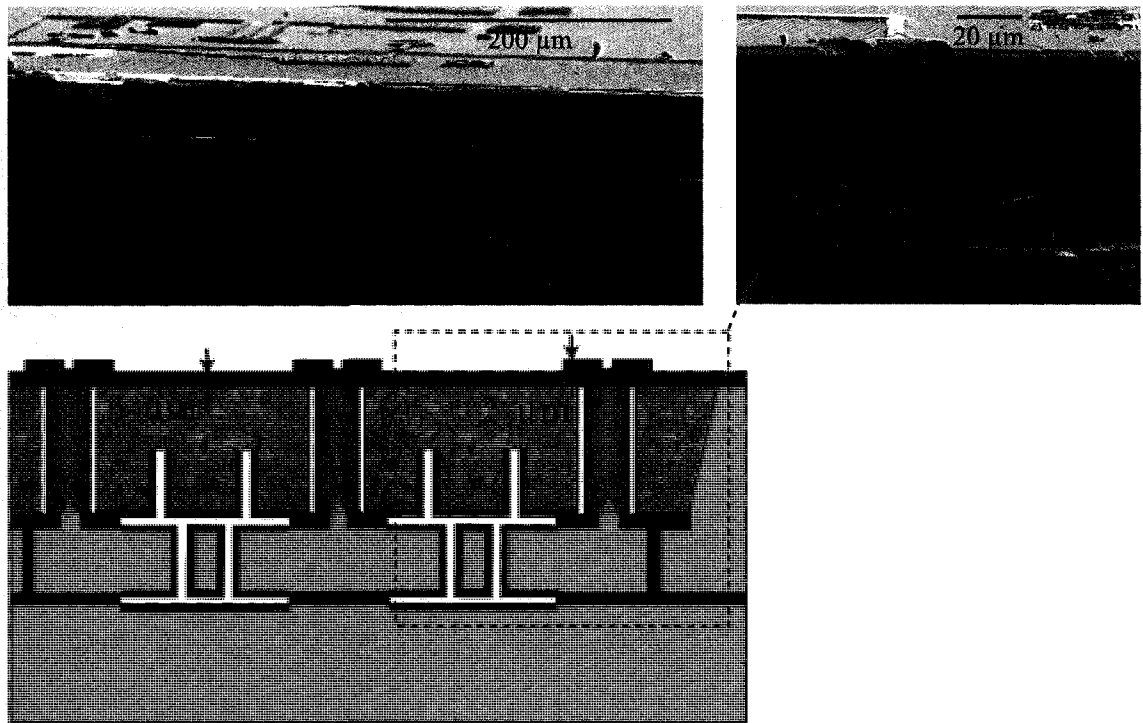


Figure 3.10: (Top Left) SEM showing cross section of device after completion of fabrication. Aluminum traces can be seen on top of the encapsulation. Under the surface of the wafer, there are three electrodes and two cavities where the double ended tuning beams are located. (Top Right) SEM showing cross section through the isolation post and its connection to the electrode. An aluminum trace is shown making contact with the isolation post. (Bottom) Enlarged cross section drawing.

After etching, the isolation posts are electrically isolated. However, before aluminum traces to the interconnects can be formed, the surface must be passivated with silicon dioxide. The passivation silicon dioxide is deposited using low-temperature oxide (LTO) at 450 °C. Approximately 3 μm of LTO is deposited to fully passivate the surface and seal the isolation post trenches. Openings are made in the passivation oxide only over the isolation posts. This alignment is also critical. Approximately 2 μm of 100% Aluminum is sputtered at 40 °C after a short etch is performed in the sputtering chamber to remove native oxide and improve the electrical contact. A dry aluminum etch of the traces and bondpads is preferred as it allows thinner traces to be formed with no “mouse-bites” associated with wet etching.

3.1.9 Post-processing

After the wafer is completed (Figure 3.11), the hydrogen in the resonator cavity is diffused through the encapsulation by placing it in a 400 °C nitrogen environment furnace. The “epi-seal” composite resonator process should not significantly effect the diffusion pathway of hydrogen compared to the “epi-seal” of silicon resonators process since the dominant diffusion path is through the trenches of the isolation trench layer which remain unchanged[51]. After diffusion, the resonators are in a hermetic package at approximately 1 Pa ([50]).

The wafer-level packaging protects the resonator from contaminants in the environment. Harsh post-processing, such as wafer-dicing typically used in semiconductor post-processing, does not damage the resonator. For the DETF devices, higher than 90% yield is found. The yield loss is mostly due to accumulation of small defects during the lengthy processing.

Typically, resonators are designed within an 800 μm by 800 μm area. An additional 100 μm border around the die is allocated as the dicing lane. After dicing, the roughly 1 mm by 1 mm die are epoxied into an open-lid standard IC package. Once glued, 50 μm diameter gold or aluminum wirebonds are used to connect the bondpads on the resonator die to the IC package (see Figure 3.12). The package can

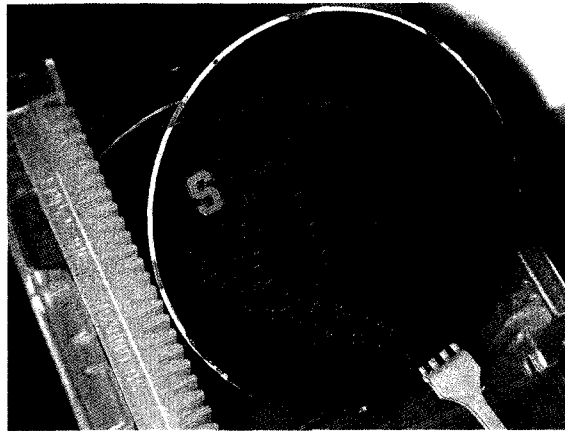


Figure 3.11: Photograph of a completed wafer containing more than 3,000 resonators.

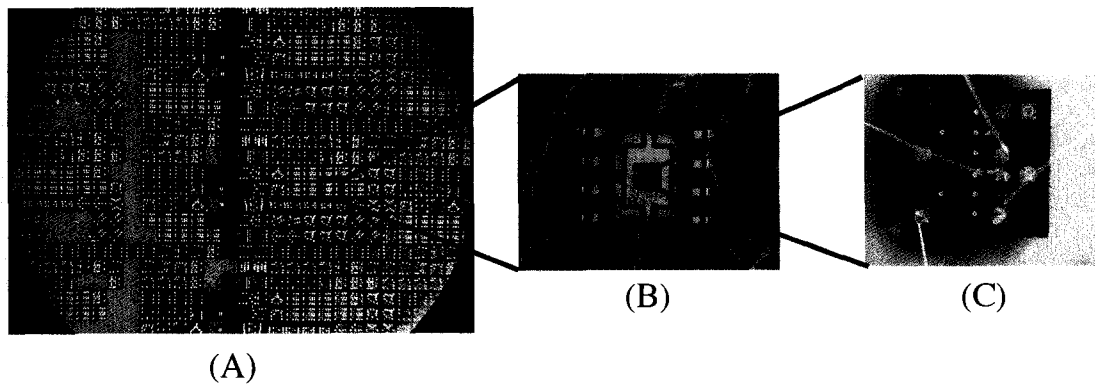


Figure 3.12: (A) 1mm x 1mm die are singulated after wafer dicing. (B) Resonator die is bonded to an open lid IC package. (C) Resonator die is wire-bonded to contacts in IC package.

then be mounted onto a printed circuit board and is ready for testing. Although the fabrication time can be lengthy, taking several months to complete, the final packaged devices are robust and provide a stable environment for testing.

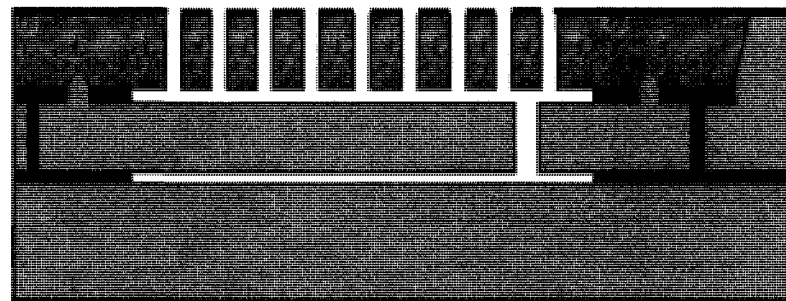
3.2 Fabrication Challenges

Throughout fabrication, there were several new challenges which initially resulted in critical failures. The majority of the the problems were wafer-level, not resonator-level problems. As a result, when many of the issues were overcome or minimized the finished wafers had high part yields.

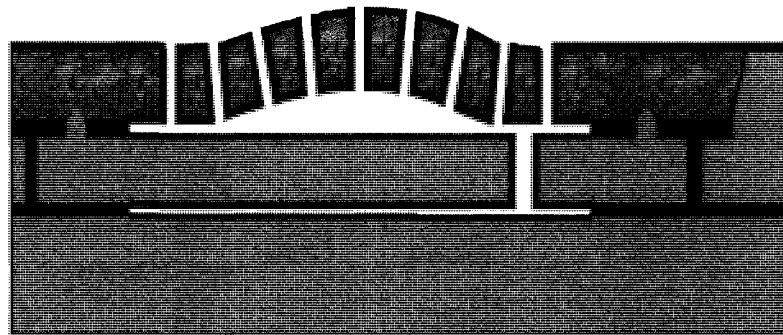
3.2.1 Membrane Buckling

The overarching problems were the result of stresses developed during thermal oxidation to form the composite. The first problem encountered was deformation/buckling of the 1st encapsulation layer during thermal oxidation (Figure 3.13). In the original “epi-seal” of silicon resonators, the 1st encapsulation layer (Figure 3.4) was 2 μm thick. Devices that had large areas, especially larger than the area over the coupling-beams of the DETF, had large encapsulation membranes suspended over the device. After oxidation, membranes that had areas of 800 μm by 800 μm could buckle as much as tens of microns.

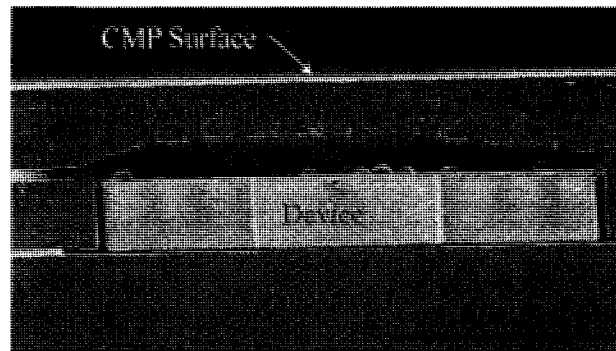
The solution was two-fold: increase the membrane thickness and limit its area. The membrane area can be considered as a circular or rectangular membrane that is clamped on all edges. The deflection of this membrane reduces with the third power of the thickness and the second power of the smallest span length [95]. By increasing the thickness by an order of magnitude and limiting the smaller of the two dimensions of the span to 150 μm , the deflection was reduced by several orders of magnitude.



(A)



(B)



(C)

Figure 3.13: (A) Device with large membrane span prior to thermal oxidation (B) After oxidation the membrane buckles (C) SEM of device with large membrane span. The membrane buckled after oxidation. The device undergoes “epi-seal” and chemical-mechanical polish (CMP).

3.2.2 Wafer Bowing

The second largest problem was wafer curvature after oxidation. Initially, a silicon nitride layer was not used to block oxidation on the top surface of the wafer. Prior to thermal oxidation, the amount of silicon dioxide on the back of the wafer is approximately matched to the buried silicon dioxide and TEOS silicon dioxide near the top of the wafer. However, before thermal oxidation, the silicon of the 1st encapsulation is exposed on the top surface. Since a thick layer of silicon dioxide is exposed on the backside of the wafer, during oxidation only the top surface is oxidized. This causes a slight mismatch in the symmetry of the overall stack. Low stress silicon nitride is deposited to avoid oxidation of the top surface.

Although using silicon nitride to reduce wafer curvature was initially successful in reducing wafer curvature, subsequent fabrication runs found a second factor influencing wafer bow - residual stresses developed in polycrystalline silicon. Residual stresses formed during oxidation of polycrystalline silicon could be due to the diffusion of oxygen along the grain boundaries, especially for long thermal oxidation times associated with dry oxidation and high phosphorous doped layers [48]. The thermal oxidation to form a composite resonator occurs in two steps (Section 3.1.6). In the second step, after the silicon nitride has been plasma etched, a thin thermal oxidation of approximately 1000 angstroms is performed. Note that the second oxidation will grow thermal oxide on the top surface due to the exposed silicon of the 1st encapsulation. Unexpectedly, 1000 Angstroms of oxide caused many of the wafers to bow, making further processing difficult. The wafer bow was particularly harmful on wafers with large areas of polycrystalline silicon. The polycrystalline silicon area is defined after the TEOS sacrificial silicon dioxide etch which forms the electrical contacts. The designer has the option of also removing all TEOS that is not covering the device. During the 1st epitaxial silicon deposition (Section 3.1.4), polycrystalline silicon grows on top of the TEOS. Limiting the TEOS area will also limit the polycrystalline silicon area. Note however, that during TEOS deposition, silicon dioxide is deposited on both the front and the back of the wafer. If a large portion of TEOS silicon dioxide is removed from the front of the wafer, it might be necessary to remove a similar portion from the back of the wafer.

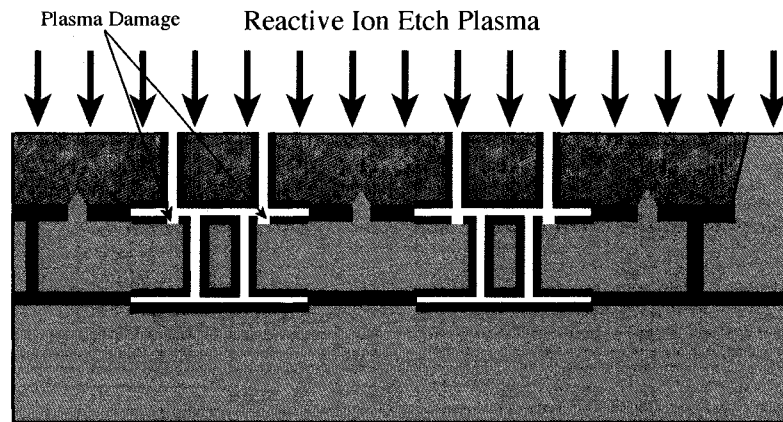


Figure 3.14: During the plasma damage of the silicon-nitride layer, the directional plasma moves through the vents in the membrane and etches the silicon dioxide directly under the vents.

3.2.3 Plasma Etch Damage and Other Consequences

After the first thermal oxidation, a plasma etch is used to remove the approximately $0.4 \mu\text{m}$ of silicon nitride on the top surface of the wafer (Figure 3.14). During oxidation it is believed that the very top layer of the silicon nitride becomes silicon oxy-nitride. Precise plasma etching of this layer is difficult due to a lack of etch uniformity - the center of the wafer tends to be etched faster than the edges- and lack of a precise etch end-point detector. Since it is crucial that a silicon surface is exposed for the subsequent “epi-seal” step, the silicon nitride etch will almost certainly be overetched. As a consequence of this overetch, the directed plasma will enter through the vent holes and bombard the thermally grown silicon dioxide inside the resonator cavity directly under the vents. When overetched, the silicon dioxide over the vent can be completely removed, leaving an exposed silicon surface. Figure 3.15 shows the plasma damage on the resonator due to the directional plasma etch. Note that an isotropic etch is more harmful as it will remove the thermal silicon dioxide inside the cavity.

Since some plasma etching is unavoidable during this step, the vents were moved off of the beam and were placed parallel to the beam but over the electrodes. Since the thermal oxide on the beam is not attacked, the oxide coating on the beam remains

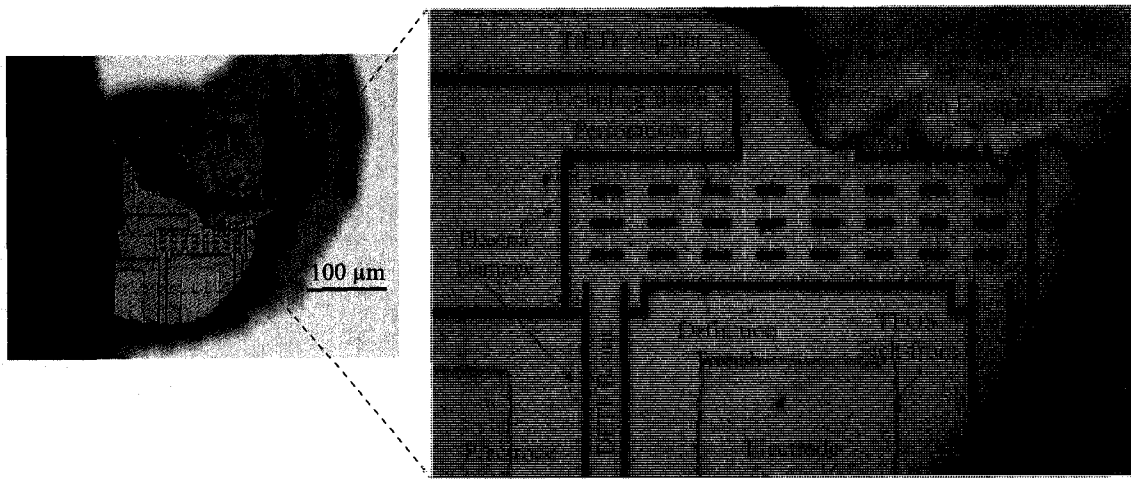


Figure 3.15: True-color microscope image of DETF with broken encapsulation. The silicon dioxide appears pink in the figure. Silicon appears as grey. Damage in the silicon dioxide is seen in the form of white slots. The white slots, appearing on the DETF, correspond to arrangement of the vents in the encapsulation above the device. During plasma etch of the silicon-nitride, directional plasma attacks the silicon dioxide. If overetched, the silicon dioxide in the damaged areas is completely removed, revealing silicon.

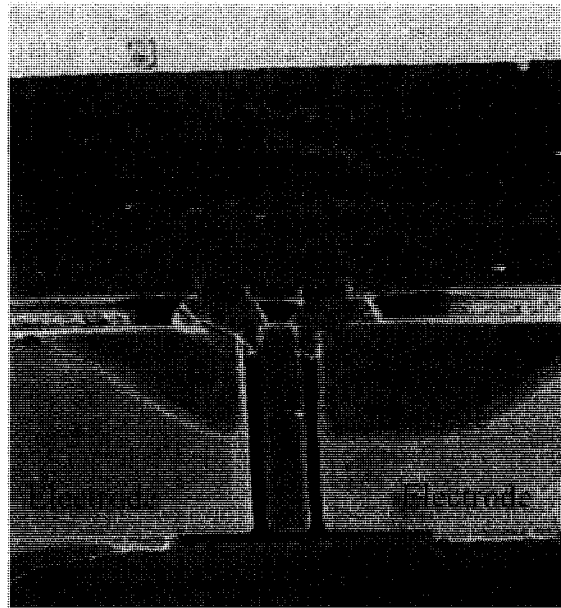


Figure 3.16: During plasma overetch of the silicon-nitride layer, the directional plasma completely removes the silicon dioxide over the vents and reveals silicon. During “epi-seal,” silicon is deposited in the cavity at the location of the plasma damage. If the vents are sufficiently large, during the sealing, silicon plugs form at the site of the damage. These plugs can grow to completely fill a nearby trench. SEM shows two plugs under the vents that have mechanically shorted the trenches between the beam and the electrodes.

symmetric. However, as we will see in Chapter 6, the plasma damage could be causing unwanted frequency instabilities in the resonator.

The motivation for the second oxidation was the result of a critical failure due to the overetch of the silicon nitride and thus the exposing of a silicon surface inside the cavity directly under the vents. During the selective silicon deposition of the “epi-seal” step, silicon is preferentially grown on top of silicon and not silicon dioxide. During the “epi-seal” step, silicon will grow on the exposed silicon inside the cavity due to the plasma etch. If the vents are large, silicon plugs can form starting at the exposed silicon. If the exposed area is close to a definition trench, the plug can grow to fill the definition trenches such that the devices are mechanically shorted (see Figure 3.16).

To avoid this, a thin 1000 Angstrom thermal oxidation is performed at a lower temperature, approximately 900 °C, to carefully control the growth. Since the oxide is grown on silicon and is thin, the plasma etch can be optimized to remove this silicon dioxide without needing an overetch. The etch rate of silicon dioxide on the top surface of the wafer is faster than inside the cavity. As such, a precisely timed silicon dioxide etch will leave silicon dioxide remaining inside the cavity.

3.2.4 Composite Dimension Uncertainty

In the creation of “zero-TCf” composite resonators it is essential to know the dimensions of the silicon and silicon dioxide portions of the resonator. However, the fabrication and encapsulation processes makes determining dimensions very difficult.

After the DRIE etch forms the beams of the resonator, the topology of the trench is not the “ideal” parallel sidewall configuration. Not only is there tapering and scallops on the sidewalls, the dimensions of these features varies across the wafer by hundreds of nanometers.

During thermal oxidation to form the composite, some of the silicon in the beam will be consumed. The amount consumed depends on the crystallographic orientation of the surface on which the growth is occurring. The top and bottom surfaces of the beams are $\langle 100 \rangle$ oriented, whereas the sidewalls would ideally be $\langle 110 \rangle$ oriented. However due to the tapering and scalloping of the sidewalls, the $\langle 110 \rangle$ orientation is only the nominal orientation. The amount of silicon dioxide grown on these surfaces also varies, not just due to the scalloping but also the crystallographic preference.

Knowledge of dimensions is further complicated by having no optical access to the resonators after thermal oxidation since the resonators are “buried” under the encapsulation. IR imaging does not provide high enough resolution to provide accurate measurements of any of the beam dimensions. Breaking a die to cross-section the composite can provide reasonably accurate oxide thickness measurements. However, due to the DRIE, the beam widths across the wafer vary, and thus the ratio of the bending stiffness will vary from part to part. If an SEM of the part is not available, the best approximation of the thickness of the silicon dioxide inside the

cavity is to place a test wafer next to the device wafer during the oxidation. The test wafer will provide a nominal $\langle 100 \rangle$ silicon dioxide thickness that can be measured on the top surface of the test wafer. To approximate the $\langle 110 \rangle$ direction thickness the Deal-Grove model can be used with modified parameters.

3.2.5 Miscellaneous Problems and Discussion

The initial steps of the “epi-seal” composite encapsulation follow closely those of the “epi-seal” silicon resonator encapsulation. However, the presence of stresses during the thermal oxidation of composite formation required a thicker epitaxial silicon deposition for the 1st cap and an additional CMP step.

After the “epi-seal” step, the total thickness of the encapsulation is approximately $40 \mu\text{m}$. The consequence of such a thick encapsulation impacted every subsequent fabrication step. The high aspect ratio DRIE etch to form the isolation posts needed a silicon dioxide hard mask because use of photoresist as a mask resulted in “mouse-bites.” Even using a hard-mask, the trench width would “blow-out” due to the long DRIE etch.

A wider isolation trench leads to a thicker LTO deposition for the passivation to fill the trenches. Thick silicon dioxide layers, greater than $3 \mu\text{m}$, can be difficult to etch. Such layers often require thick layers of photoresist whose features are more difficult to control and could begin to burn due to the lengthy etch times.

Thicker passivation silicon dioxide layers lead to thicker aluminum depositions to fill the contact openings. As with thick silicon dioxide layer, thick aluminum layers have similar processing disadvantages. In general, etching of thick, non-silicon, films are not a standard processes in semiconductor equipment.

Although there is much room for improvement of the “epi-seal” composite process, many of the issues have been minimized such that high yield composite resonator wafers can be fabricated and packaged in a clean, hermetic environment, capturing many of the benefits of the “epi-seal” technology.

3.3 Summary

In this chapter a modified “epi-seal” process for hermetic vacuum level sealing of composite resonators is described. Flexural and extensional mode single-crystal silicon resonators were designed. The composite structures were formed using thermal oxidation just after the resonator is released, but before the cavity in which the resonator resides is sealed using epitaxial polycrystalline silicon. Thermal oxidation from 0.33 μm to 0.42 μm , measured on a $\langle 100 \rangle$ silicon surface, formed the composite. The majority of the modified process is the result of addressing thermal stresses that formed during the thermal oxidation composite-formation step and ensuring electrical interconnects remain functional. Four inch fully processed wafers with greater than 90% composite resonator yield were manufactured. The wafers then underwent harsh post-processing, such as wafer-dicing and wirebonding, to yield 1 mm by 1mm by 0.6 mm die with encapsulated composite resonators.

3.4 Acknowledgements

The development of the modified “epi-seal” fabrication process for composite resonators was a collaborative effort with Bongsang Kim. Saurabh Chandorkar, Matt Hopcroft, Hyungkyu Lee, and Violet Qu also contributed to the fabrication. General advice and help was also provided by Gary Yama. SEM images of cross-section of composite resonators were taken with the help of Gary Yama and Mariam Ziaei-Moayyed.

Chapter 4

“Zero-TCf” Resonators

The “epi-sealed” composite resonator combines a CMOS-compatible wafer-level hermetic packaging technology with a passive temperature compensation scheme. Both technologies are necessary for silicon resonators to become competitive with the frequency stability of quartz crystal resonators in high precision applications.

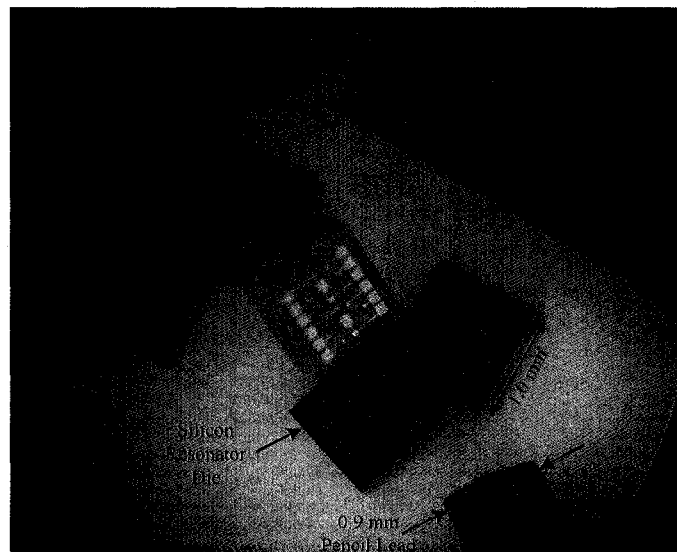


Figure 4.1: Singulated composite resonator die next to 0.9 mm pencil lead.

In this chapter the experimental temperature-frequency behavior of “epi-sealed” composite resonators is presented. A composite resonator with the ideal ratio of

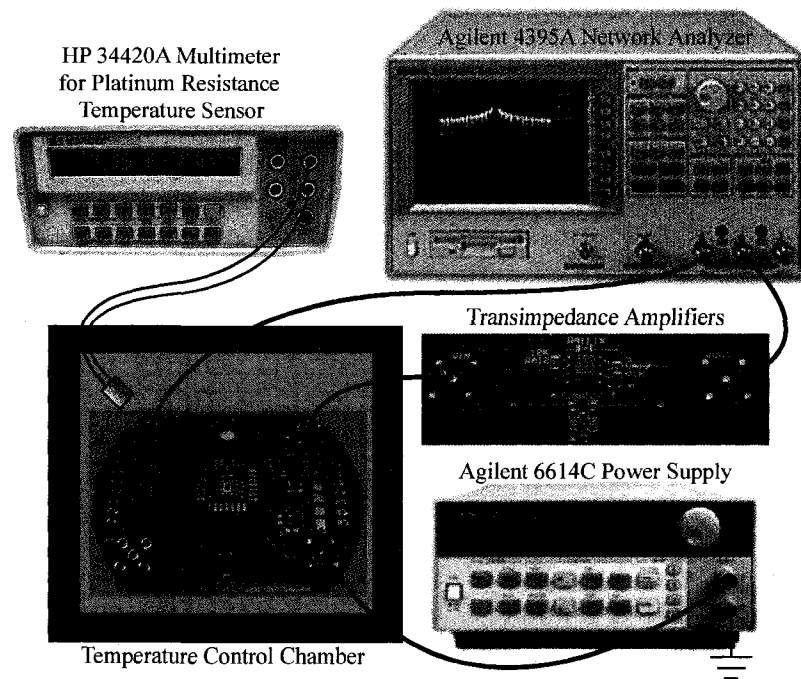


Figure 4.2: Test setup for measuring frequency-temperature behavior of composite resonators.

silicon to silicon dioxide is demonstrated. This resonator exhibits approximately 150 ppm of frequency variation over a 125 °C temperature range. This level of frequency variation is comparable to that of quartz crystal resonators.

4.1 Composite Resonator Testing

A resonator is typically part of the oscillator architecture which forms a frequency reference. However, to determine the natural frequency of the resonator it is not necessary to build the entire oscillator architecture. Instead, the resonator can be treated as a dynamic system whose frequency response can be obtained by applying a known input forcing function. The frequency of the input forcing function can be swept using a network analyzer. In this section, the testing environment which is used to obtain the frequency-temperature behavior is described.

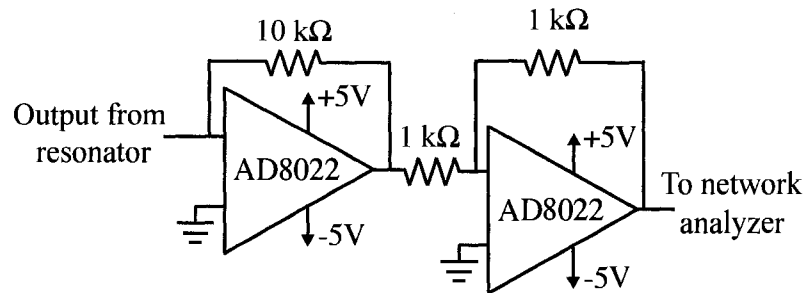


Figure 4.3: Transimpedance amplification circuit diagram.

The key components of the experimental setup are (see Figure 4.2):

1. A composite resonator die attached to an open-lid IC package and wirebonded. The resonator requires a bias voltage, an AC input voltage from a network analyzer, and a ground line for operation. The output of the resonator is an oscillating current (see section 1.2.1).
2. A transimpedance amplifier board which converts the output current from the resonator to an amplified voltage signal (Figure 4.3). The AD8022 is low-noise amplifier. The second transimpedance amplifier is used as an inverting buffer to revert the phase shift associated with the first amplifier.
3. A network analyzer provides the AC voltage to the resonator and sweeps the frequency of that input in a specified frequency range. This input forcing function is then compared to the amplified output of the resonator. The network analyzer supplies an adjustable AC voltage to the resonator. Two types of network analyzers were used, Agilent 4395A and Agilent 8753ES.
4. A power supply to provide the bias voltage to the resonator.
5. A temperature control chamber.
6. A temperature sensor with high resolution placed close to the resonator.
7. A GPIB enabled computer for experiment control and data gathering.

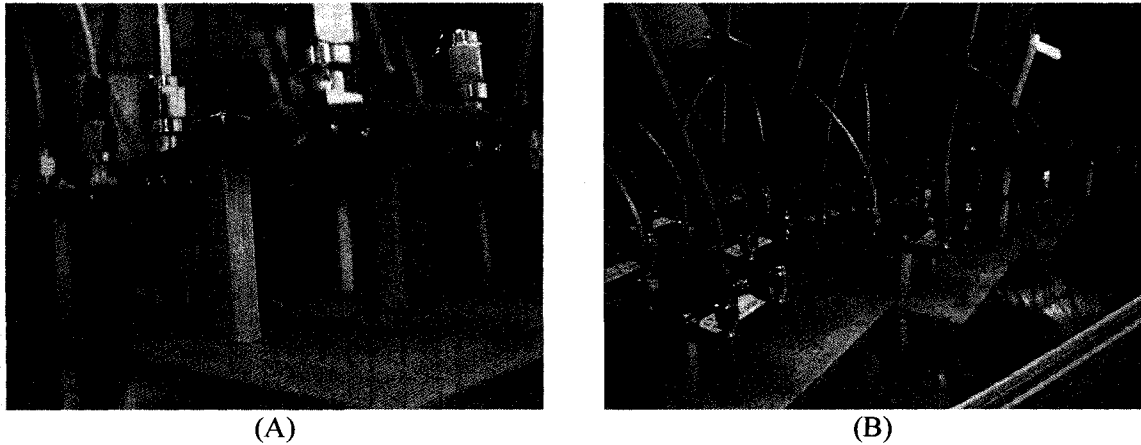


Figure 4.4: (A) An IC packaged resonator mounted to a PCB. PCB is mounted upside-down to protect the resonator. (B) Multiple resonators can be serially monitored during a given experiment using a multiplexer.

8. (Optional) A multiplexer to monitor the frequency of multiple resonators inside the temperature control chamber. In the multi-resonator setup, the multiplexer is used to actuate one resonator at a time. To minimize the noise introduced by the multiplexer, each resonator had a dedicated amplifier board and only the bias voltage and the amplified resonator response was passed through the multiplexer.

At the desired measurement temperature, the oven is stabilized to within ± 0.1 °C at higher temperatures and ± 0.5 °C at temperatures below zero. However, at low temperatures the AC voltage is reduced to avoid driving the resonator in a nonlinear regime. Figure 4.5 shows the frequency response of the resonator recorded by the network analyzer. The frequency at maximum amplitude is recorded as the resonant frequency of the resonator, f_o . The quality factor of the resonator is found using the following relation (see Figure 4.5):

$$Q = \frac{f_o}{f_{-3dB}} \quad (4.1)$$

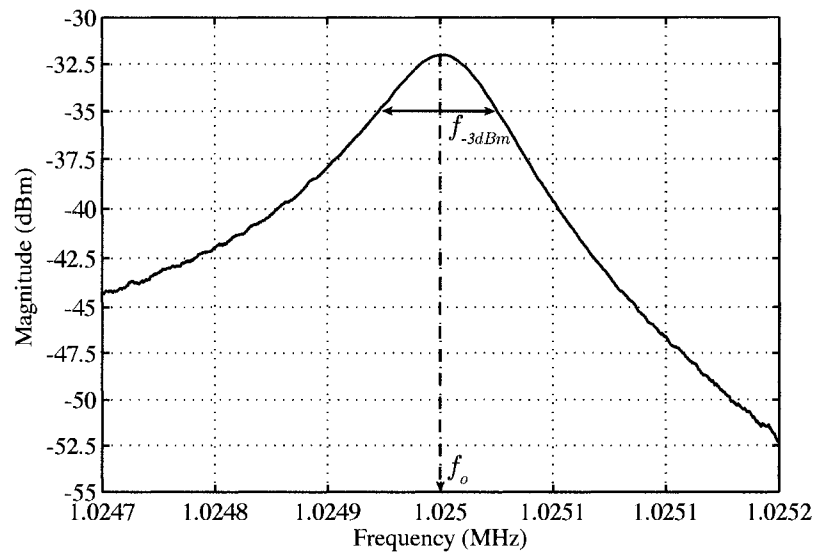


Figure 4.5: Frequency response of a 1MHz composite resonator using a network analyzer.

4.2 “Zero-TCf” Composite Resonators

In section 2.2 we found that the ideal ratio of silicon to silicon dioxide for a composite resonator to become insensitive to temperature changes is:

$$r^* = -\frac{TCf_{1,SiO_2}}{TCf_{1,Si}} \approx 3 \quad (4.2)$$

For flexural mode resonators the ratio of interest is the ratio of bending stiffness of each material’s section of the beam. For extensional mode resonators the ratio is the ratio of axial stiffness of each material’s section in the beam. To minimize the amount of silicon-dioxide in the composite, the ideal construction is a flexural-mode silicon resonator with a silicon dioxide coating. The fabrication and packaging process for these resonators was described in Chapter 3. Two flexural mode resonators, a double-ended tuning fork resonator and a wine-glass ring resonator, as well as an extensional-mode ring were fabricated and tested. Due to the large uncertainty in the material properties of silicon-dioxide, different bending stiffness ratios were achieved by varying the width of the beam while the thickness of the oxidation was constant per wafer.

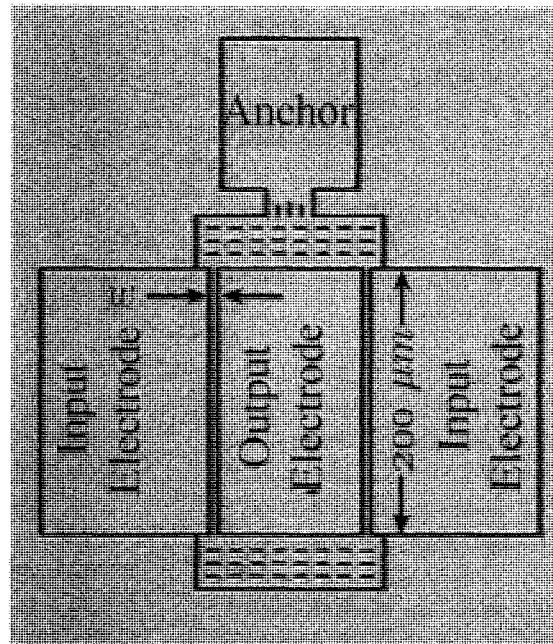


Figure 4.6: Microscope image of a DETF resonator.

The results presented use oxidation thicknesses from $0.33 \mu\text{m}$ to $0.42 \mu\text{m}$ measured on a $\langle 100 \rangle$ oriented silicon wafer.

4.2.1 Double Ended Tuning Fork Resonators

Identical DETF resonators with widths varying from $4 \mu\text{m}$ to $8 \mu\text{m}$ by $0.25 \mu\text{m}$ increments were designed such that the beams of the resonator were aligned with the $\langle 110 \rangle$ direction in the silicon crystal. These resonators were thermally wet oxidized with approximately $0.43 \mu\text{m}$ of silicon dioxide measured on the $\langle 100 \rangle$ surface. Although the actual beam width is not known due to the encapsulation, the initial beam width is approximated using SEM measurements of a similar test wafer after the definition etch. The width of the beam was found to be approximately $0.3 \mu\text{m}$ thinner than lithographically defined. The sidewall oxidation thickness can be approximated using the Deal-Grove model ([75]). However a small portion of the wafer was cross-sectioned for SEM. Approximately $0.48 \mu\text{m}$ of thermal oxide was grown on

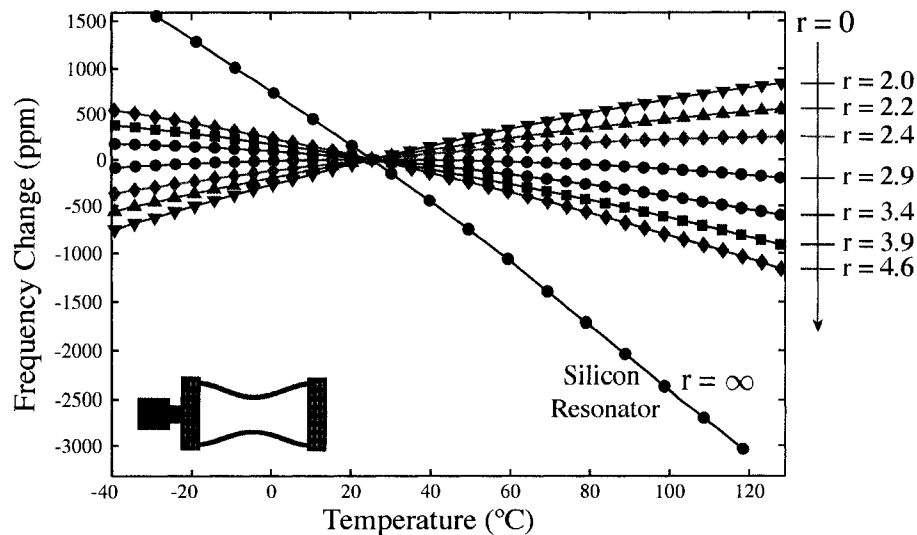


Figure 4.7: Frequency-temperature behavior of composite DETF resonators with varying bending stiffness ratios.

the $\langle 110 \rangle$ sidewalls of the resonator. In determining the bending stiffness ratio, it was assumed that in the process of thermal oxidation the amount of silicon consumed is approximately 46% of the total thickness of the thermal oxide grown ([75]).

Figure 4.7 is a plot of frequency-temperature behavior for the beams of varying ratio r . The bending stiffness ratios were determined by using Young's Modulus values of 169 GPa and 71 GPa for $\langle 110 \rangle$ single crystal silicon and silicon-dioxide, respectively. The minimum frequency variation is seen for a ratio of approximately 2.9.

Using figure 4.7, the linear temperature coefficient of frequency at 25 °C can be found by taking the slope of the frequency-temperature behavior at 25 °C. Figure 4.8 shows the $TCf_1(25^\circ\text{C})$ of each resonator in figure 4.7. The figure also plots the expected value of $TCf_1(25^\circ\text{C})$ using the analytical equation found in Chapter 2. The solid theory line uses the average value of silicon-dioxide temperature coefficient of Young's Modulus from the values found in literature, $TCE_{1,\text{SiO}_2} = 183 \text{ ppm}/^\circ\text{C}$. The dashed lines indicate the $\pm 29 \text{ ppm}/^\circ\text{C}$ single standard deviation of TCE_{1,SiO_2} found

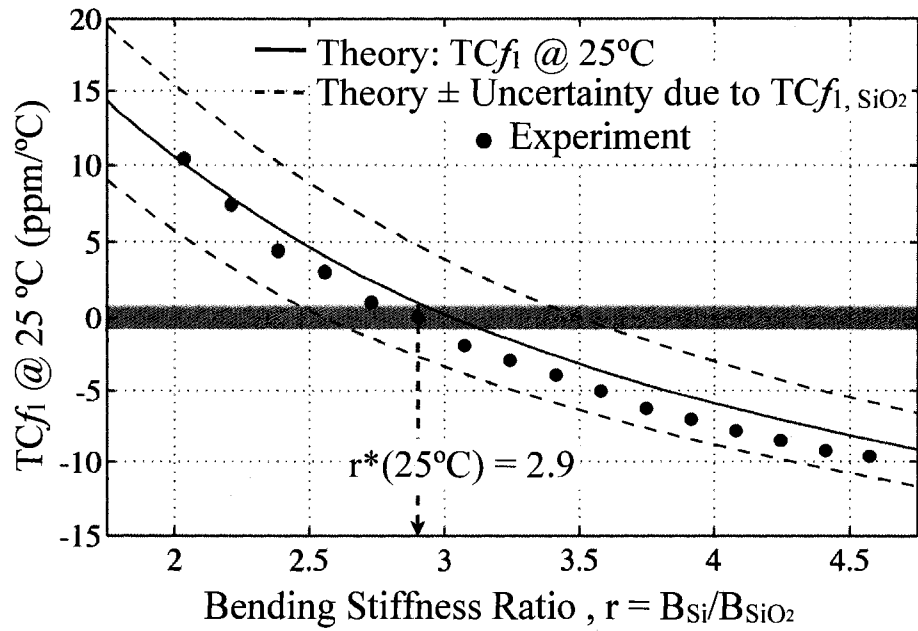


Figure 4.8: Linear temperature coefficient of frequency TCf_1 at 25°C .

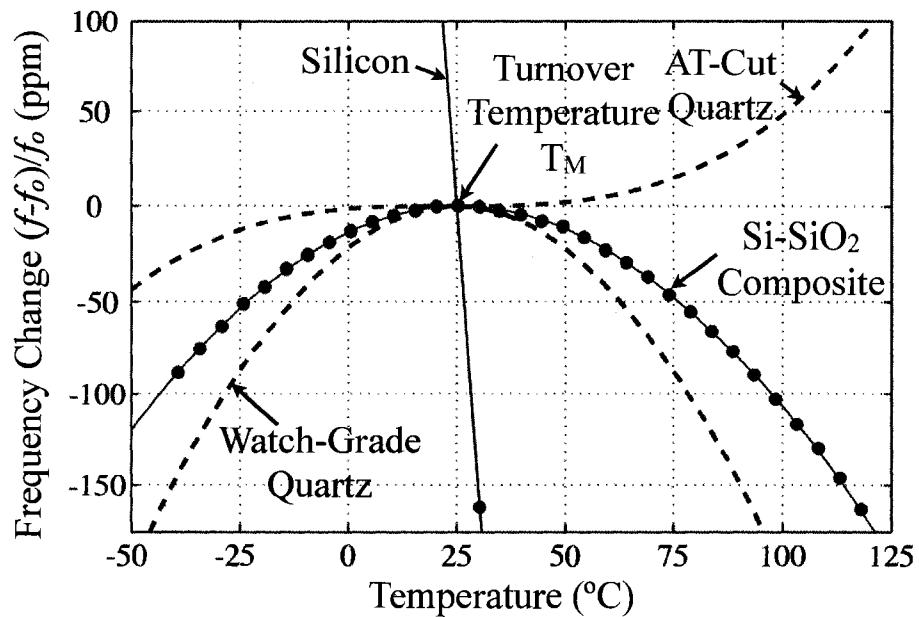


Figure 4.9: Measured frequency-temperature behavior of a silicon resonator and a composite resonator with ideal bending stiffness ratio compared to expected frequency behavior of quartz crystal resonators of two popular cuts.

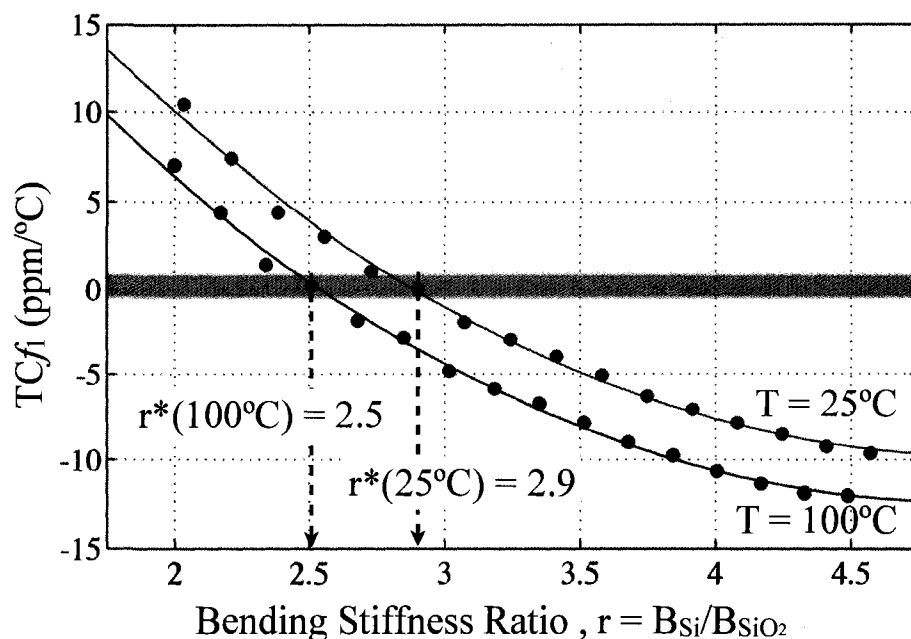


Figure 4.10: Linear temperature coefficient of frequency at 25 °C and 100 °C for varying bending stiffness ratios. The ideal ratio at which TCf_1 is zero changes with temperature.

in literature. The behavior is consistent with expected results within the uncertainty due to material properties. The device closest to zero temperature coefficient of frequency at 25 °C has a ratio of 2.9.

Figure 4.9 shows comparison of frequency temperature behavior for four different resonators: a silicon resonator, an ideally compensated (at 25 °C, $r=2.9$) composite resonator, a watch-grade quartz crystal tuning fork, and an AT Cut quartz crystal. The composite resonator shows a quadratic temperature dependence. The maxima, where the slope is zero, is the turnover temperature, T_m . At this temperature the linear temperature dependence is cancelled - leaving only higher order terms. A parabolic behavior indicates that there are significant quadratic dependencies on temperature.

If the linear temperature coefficient of frequency is extracted at 100 °C, $TCf_1(100^\circ\text{C})$, from Figure 4.7 we see a translation of the TCf curve (Figure 4.10). The resonator

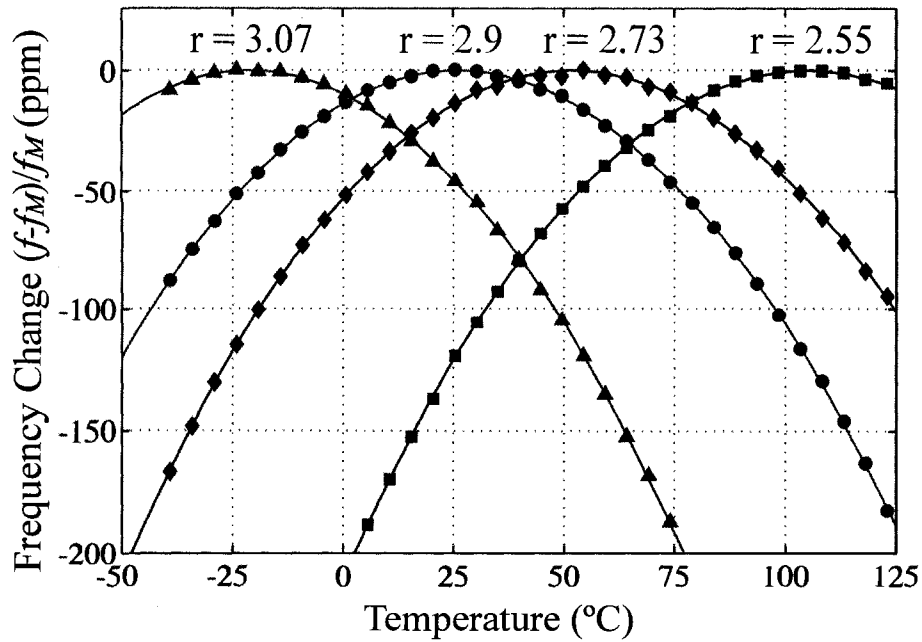


Figure 4.11: Tuning of turnover temperature to be at the desirable operating temperature.

with the "zero-TCf" at 100 °C has a ratio of 2.5. This indicates that the linear temperature dependence can only be cancelled at a particular temperature with a particular ratio. For example, to use a resonator in a oven controlled system, it would be desirable to design a resonator with a turnover temperature at an elevated temperature at which the oven will operate.

Figure 4.11 shows the frequency temperature behavior of the resonators with bending stiffness ratios close to 3. Slight changes in the ratio result in a translation of the turnover temperature. The resonator can be designed to match the operating temperature conditions of a particular application. This is similarly done in quartz crystal resonators where the resonator used in wrist watches has a turnover temperature designed to be at the temperature of human skin. The non-linear behavior of the composite resonator will be discussed in more detail later in the chapter.

It is interesting to note that resonators with beams oriented along the $\langle 100 \rangle$ direction will have a lower Young's Modulus than those oriented along the $\langle 110 \rangle$

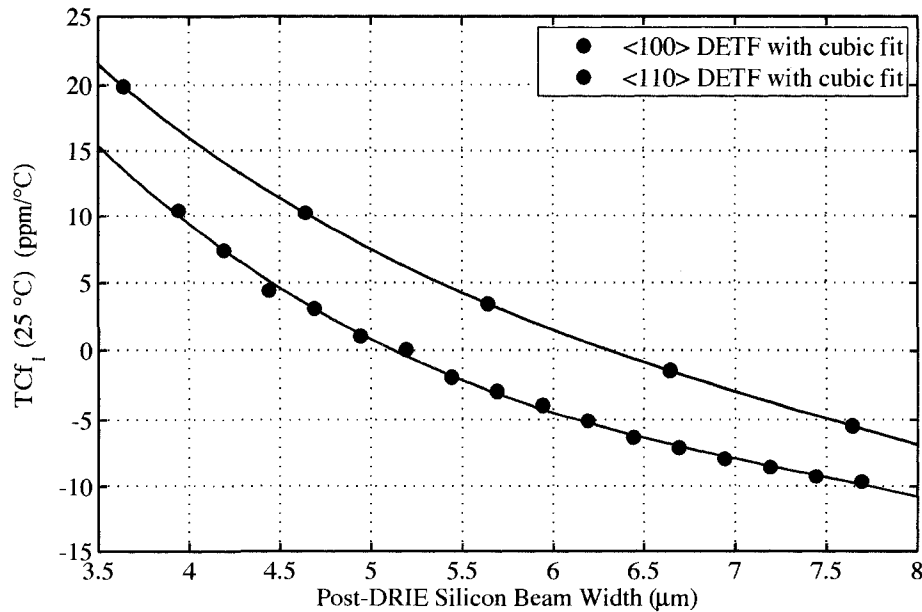


Figure 4.12: the linear temperature coefficient of frequency at 25°C versus the post-DRIE silicon beam width (prior to oxidation and corrected for etch). Data from <110> oriented DETF from Figure 4.8 is re-plotted using beam width. Data from <100> oriented DETF is shown for comparison.

direction in the silicon crystal. The <100> and <110> Young's Moduli are approximately 130 GPa and 169 GPa, respectively. Thermal oxidation of the <100> sidewalls in the <100> oriented DETF will also be smaller. However, for a given beam width, the overall bending stiffness ratio of the <100> oriented DETF will be smaller compared to the <110> oriented DETF. This indicates that <100> DETF will have a more positive TCf for a given beam thickness. The implication is that wider beams can be ideally compensated when they are aligned with the <100> crystallographic orientation. DETF resonators with beams oriented along the <100> direction were fabricated on the same wafer as the <110> oriented DETF resonators previously presented. All resonators were thermally wet oxidized with a 0.42 μm of silicon dioxide measured on the <100> surface. A comparison of the linear temperature coefficient of frequency at 25°C for the two orientations is shown in Figure 4.12.

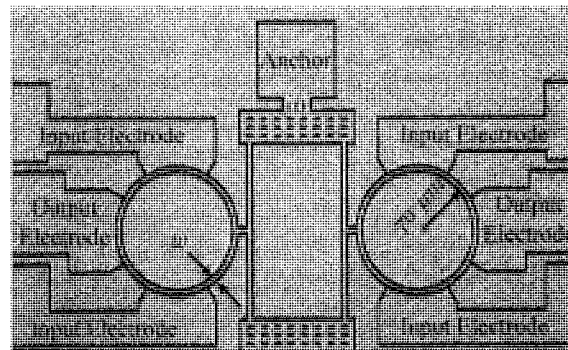


Figure 4.13: Double ring resonators whose flexural-mode frequencies are matched to the first flexural mode of the DETF. The DETF acts as the connector to the anchor to minimize anchor loss from the vibration of the ring.

4.2.2 Flexural Mode Ring Resonator

Double ended tuning fork resonators provide an exceptional platform for testing composite flexural mode resonators. However, one of the disadvantages of flexural beam resonators is their inability to scale to higher frequencies. The DETF resonators explored in the previous section were in the hundreds of kHz to 1.5 MHz range. One straight forward way to scale frequency is to build flexural mode ring resonators with small radius. Unlike tuning fork resonators, the ring resonators can be coupled using an array to improve power handling in a more straightforward way [69].

To prototype composite ring resonators, the resonators were designed in the same frequency range as the DETF's. Operating in this lower frequency range eliminates the need for the associated complex high-frequency measurement setup due to a lower output signal from the resonator.

Another element in the design of the ring resonator was the configuration of the connections to an anchor. To reduce anchor loss, and thus increase the quality factor, higher frequency ring resonators are typically connected to an anchor using a mode matched quarter wavelength support at the nodal point of the ring's vibration [1, 60, 93]. However, for lower frequency ring resonators, the length of the stem becomes long and thus has many lower frequency modes of vibration. To overcome this problem, the connection to the anchor was designed as a double-ended tuning fork. The frequency

of the beams of the tuning fork were designed to match to the flexural mode of the ring resonator (Figure 4.13).

If the resonator's material were isotropic and the connecting design was a simple clamped-clamped beam, the length of the beam could be simply determined by setting the ring's flexural mode frequency (2.24) to the beam's flexural mode frequency (2.19) and solving for the length of the beam. This would be particularly simple if the width of the beam and ring were identical such that the bending stiffness, and thus temperature coefficient of frequency, were identical. However, the anisotropic nature of the elastic properties of silicon as well as a complex tuning fork geometry make a simple analytical mode matching relationship insufficient. A finite element analysis is necessary to determine the exact length of the tuning fork beams. For example, the frequency of a DETF resonator is approximately 10% less than the frequency of a clamped-clamped beam resonator with a length identical to the beams of the DETF. This is due to the contribution of the coupling beams to the overall stiffness of the DETF.

The designed ring resonators, shown in Figure 4.13, all had identical ring radii of $70 \mu\text{m}$, while the ring width was varied. The width of the DETF beams were matched to the width of the ring resonator. However, the length of the DETF was determined using a finite element analysis software, COMSOL, to match the frequencies. The rings were oxidized with a $0.35 \mu\text{m}$ of silicon dioxide using dry thermal oxidation. The frequency-temperature behavior of the ring resonator is shown in Figure 4.14.

Due to the anisotropic nature of silicon, the simple relationship for the flexural mode found in equation 2.32 does not hold. The fundamental equation for the ratio, from equation 2.30, must be used to compare the ratio of mass and frequency. A finite element analysis is performed to determine the bending stiffness ratios. In figure 4.14, the resonator with a bending stiffness ratio of 3.0 has a turnover temperature of approximately $70 \text{ }^\circ\text{C}$. The bending stiffness ratio is determined by using a $0.3 \mu\text{m}$ reduction in the width of the ring due to DRIE etching as well as a further silicon width reduction due to consumption during oxidation of 46% of thickness of silicon dioxide ([75]).

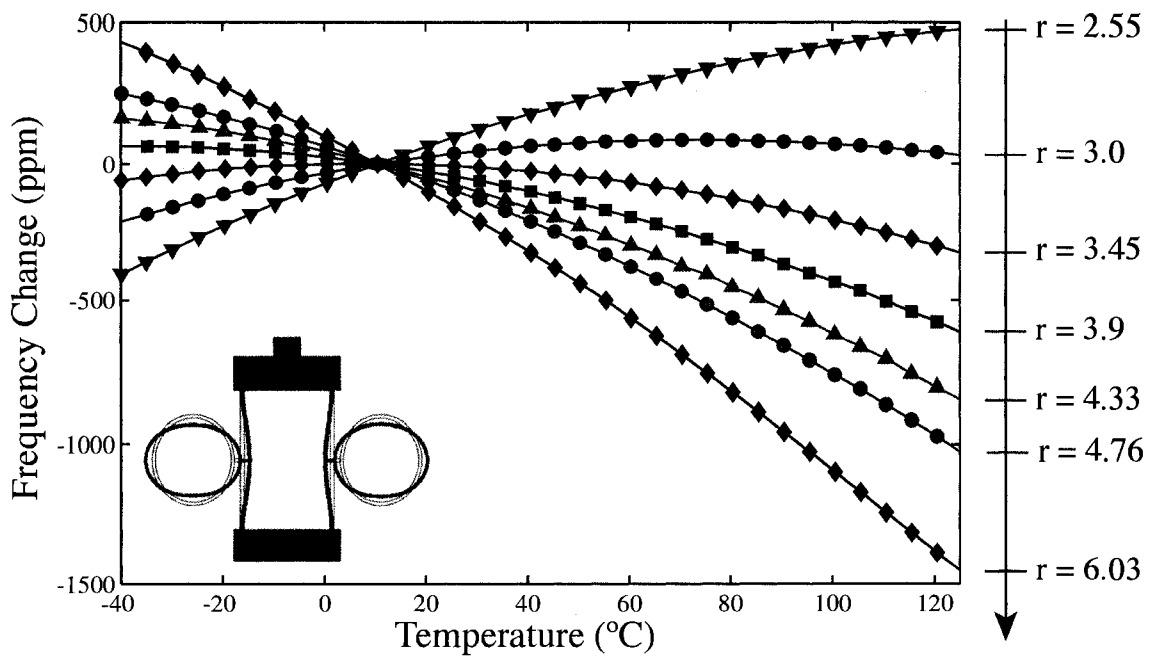


Figure 4.14: Frequency-temperature behavior of flexural-mode ring resonators with varying bending stiffness ratio. The frequency of the rings varied from 746 kHz to 1.54 MHz.

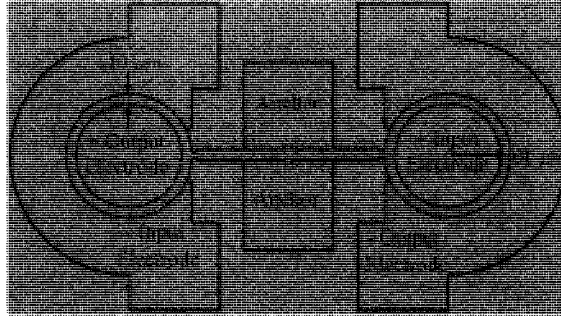


Figure 4.15: Double ring extensional-mode resonators with a stem anchor. The stem anchor is mode matched to the extensional frequency of the ring.

4.2.3 Extensional Mode Ring Resonator

Higher frequencies can also be achieved by designing bulk-mode resonators. There are many different types of bulk modes, such as extensional mode, breathing-mode, and Lamé resonators. As derived in chapter 2, bulk mode resonators tend to require a thicker silicon dioxide layer to achieve “zero-TCF” because their ideal ratio depends on the ratio of cross-sectional area. However, modest improvement in the frequency-temperature variation for bulk mode resonators can be achieved.

An extensional mode ring resonator was designed, as shown in Figure 4.15. The two rings are connected to a center anchor by mode-matched stems. The inner and outer electrodes are designed such that the area of electrostatic actuation is identical. This allows driving the resonator in differential mode to improve the signal to noise ratio. The radius of the ring is $69\ \mu\text{m}$ and the width of the ring is $10\ \mu\text{m}$. To vary the cross-sectional stiffness ratio, the width of the ring could be varied. Unfortunately, only the $10\ \mu\text{m}$ ring width was available for testing.

The frequency-temperature behavior comparison of a silicon and a composite extensional ring resonator is shown in Figure 4.16. The composite resonator has a $0.35\ \mu\text{m}$ of oxide on the $\langle 100 \rangle$ crystallographic surface. The composite shows a 30 % reduction in the linear temperature coefficient of frequency.

Due to the anisotropic nature of silicon, the simple relationship for the extensional

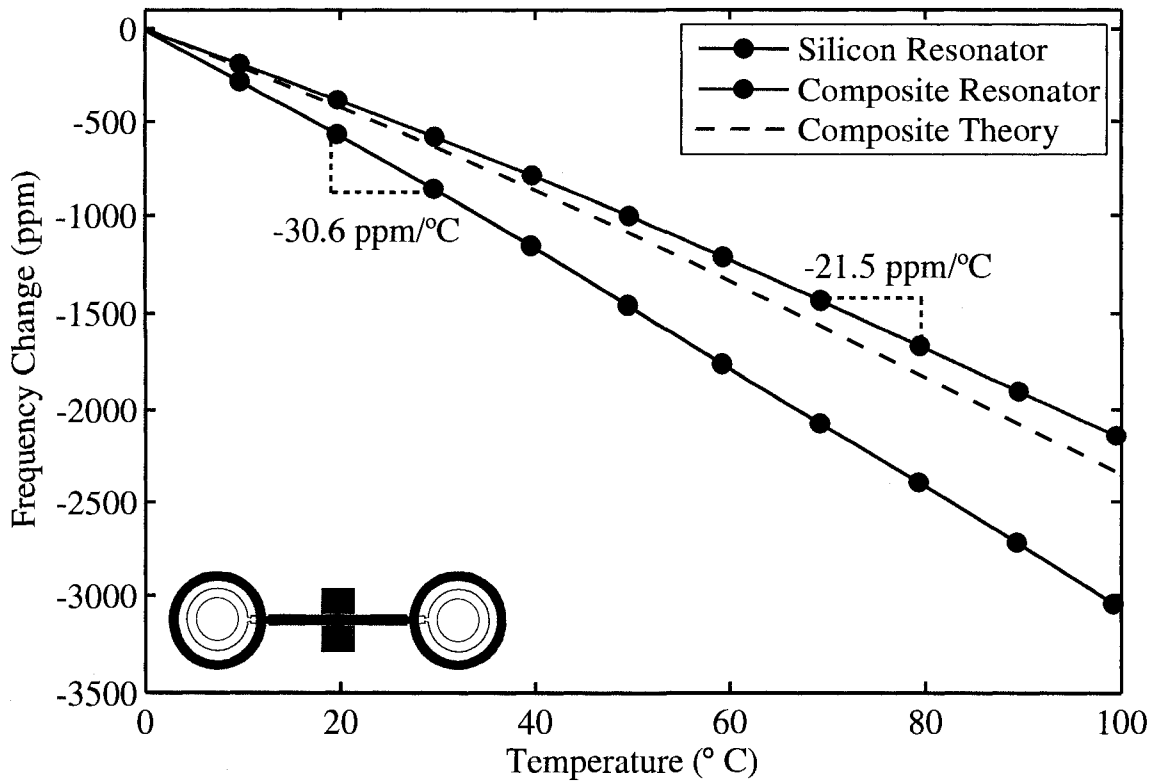


Figure 4.16: Frequency-temperature behavior of extensional mode resonator. The frequency of the silicon resonator and composite resonator is 19.8 MHz and 19.3 MHz, respectively.

mode found in equation 2.32 does not hold. Instead, the fundamental ratio (equation 2.30) which depends on mass and frequency must be used. A finite element analysis was used to determine the stiffness ratio for the resonator in figure 4.16 as 17.87.

4.3 Higher Order Effects

The use of silicon-dioxide has been shown to successfully cancel the linear temperature coefficient of frequency at a particular temperature, thus creating "zero-TCf" resonators. The resulting "residual" frequency-temperature behavior can be approximated by a quadratic function with temperature. In this section, we explore the various higher order properties that could result in this quadratic behavior and find that the quadratic temperature coefficients of Young's Modulus are primarily responsible for this behavior.

The quadratic temperature coefficient of frequency determined at the turnover temperature can be extracted from the experimental data. The TCf_2 extracted from composite DETF resonators in the $\langle 110 \rangle$ and $\langle 100 \rangle$ orientations is shown in figure 4.17. The linear change in the quadratic temperature coefficient of frequency indicates that there are other higher order temperature coefficients.

The quadratic temperature coefficient of frequency, TCf_2 , for a composite resonator has an analytical form similar to the linear temperature coefficient of frequency, TCf_1 , found in Chapter 2, equation 2.29.

$$TCf_2|_{Composite} \approx \frac{TCf_{2, SiO_2} + rTCf_{2, Si}}{1 + r} \quad (4.3)$$

In equation 4.3, the ratio r (see equation 2.30) has been previously defined. For flexural mode resonators, r is the ratio of bending stiffness. Ignoring the effects of electrostatics, the quadratic temperature coefficient of frequency for a single material is (see equation 1.35):

$$TCf_2|_{SingleMaterial} \approx \frac{1}{2}TCE_2 + \frac{1}{4}\frac{\partial \alpha}{\partial T} \quad (4.4)$$

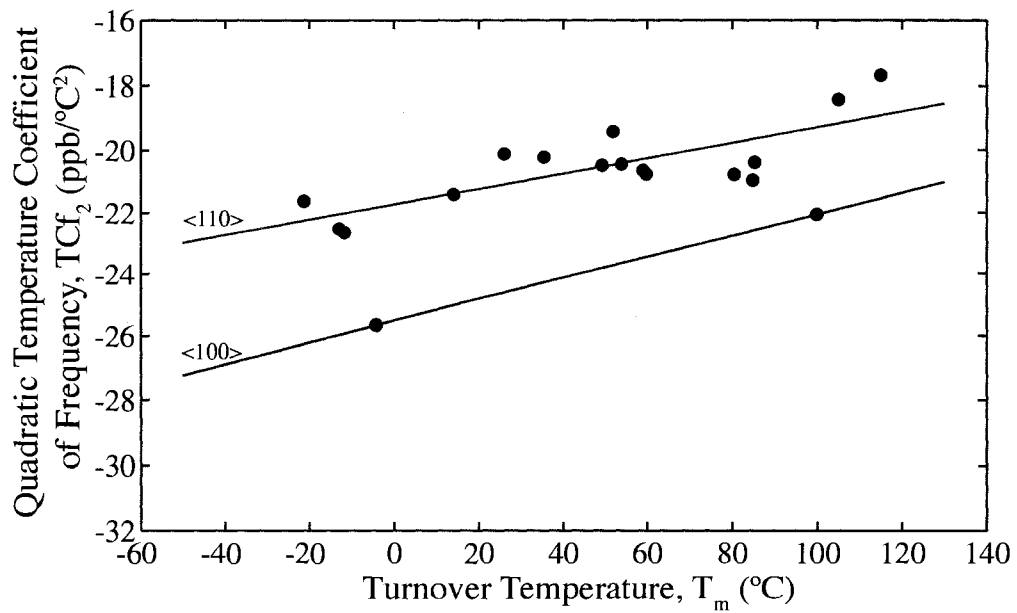


Figure 4.17: Quadratic temperature coefficient of frequency of composite DETF resonators evaluated at the turnover temperature. Data for DETF oriented along the <100> and <110> direction with respective linear fit.

The derivation of equation 4.3 can be found by careful differentiation of the equation of frequency (equation 2.19) and setting higher order terms to zero. Higher order terms are a result of cross multiplication of the linear temperature coefficients of the material properties. Another simplistic approach is to take the temperature derivative of the linear temperature coefficient of frequency for a composite (equation 2.29). This also will yield equation 4.3, and intrinsically assumes there is no cross coupling between the two materials. Since these equations are approximations, in the following sections we will examine their validity in explaining the higher order temperature effects.

4.3.1 Effect of Linear Material Properties

We begin by examining the approximation of the quadratic temperature coefficient of frequency of a single material resonator. The error in equation 4.4 is dominated by the nonlinear dependence on the linear temperature coefficient of Young's Modulus.

$$TCf_{2,error}|_{SingleMaterial} \approx -\frac{TCE_1^2}{8} \quad (4.5)$$

This indicates that even for perfectly linear materials ($TCE_2 = 0, \frac{\partial \alpha}{\partial T} = 0$), the quadratic temperature coefficient of frequency is not zero. This originates from the non-linear dependence of frequency on Young's Modulus. For a single material silicon resonator or silicon dioxide resonator, this error corresponds to approximately -0.5 ppb/ $^{\circ}C^2$ or -4 ppb/ $^{\circ}C^2$, respectively.

The error in the quadratic temperature coefficient of the composite, equation 4.3, is bounded, but the equations are generally long and best evaluated computationally. Figure 4.18 shows how the error changes with the ratio, r . As more silicon dioxide is added and r approaches zero, the error can be approximated as $-TCE_{1,SiO_2}^2/8$. If the ratio approaches infinity, or a silicon beam, the error can be approximated as $-TCE_{1,Si}^2/8$. At the ideal ratio, the error is at a minimum at approximately -0.07 ppb/ $^{\circ}C^2$.

It is important to note that part of the error shown in Figure 4.18 is due to the

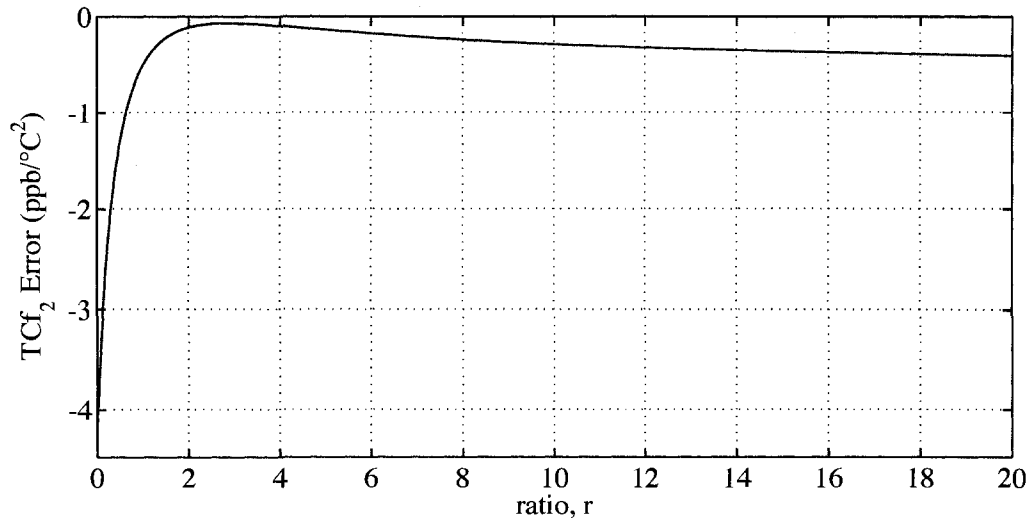


Figure 4.18: Nonlinear dependence of quadratic temperature coefficient on linear material properties.

dependence of r on the temperature. The effect of this on the TCf_2 of the composite goes to zero as r approaches zero and as r approaches infinity. Since the quadratic temperature coefficient of frequency measured at the turnover temperature, and thus at the ideal ratio, is much larger than the error in this analysis, it is a misconception that the quadratic frequency-temperature dependence of the composite is primarily due to the ratio, r , changing with temperature. It is interesting to note that the temperature coefficient of r can be approximated by taking the temperature derivative of equation 2.30:

$$TCr = 2(TCf_{1,Si} - TCf_{1,SiO_2}) \approx -240 \text{ ppm}/^\circ\text{C}^2 \quad (4.6)$$

However, the cross-multiplication of the TCr with other temperature coefficients of frequency reduces its effect on the overall quadratic temperature coefficient of frequency. Since the effect of the temperature dependence of r and nonlinear dependence on the linear temperature coefficients do not account for the measured TCf_2 , in the following section the effect of nonlinear material properties will be explored.

4.3.2 Effect of Nonlinear Material Properties

Effects that are on the order of parts per billion (ppb) can be difficult to capture. However, the contribution of several factors can be estimated. For example, the nonlinear coefficients of thermal expansion for silicon and silicon dioxide can be found in the literature [32]:

$$\alpha_{Si} = 2.6\left(\frac{ppm}{^{\circ}C}\right) + 8.66\left(\frac{ppb}{^{\circ}C^2}\right)(T - 25) - 3.44\left(\frac{ppt}{^{\circ}C^3}\right)(T - 25)^2 \quad (4.7)$$

$$\alpha_{SiO_2} = 0.583\left(\frac{ppm}{^{\circ}C}\right) + 0.317\left(\frac{ppb}{^{\circ}C^2}\right)(T - 25) - 1.034\left(\frac{ppt}{^{\circ}C^3}\right)(T - 25)^2 \quad (4.8)$$

The effect of these nonlinear coefficients of thermal expansion on the dimensions of the resonator can be found as:

$$L = L(T_o) \left(1 + \int_{T_o}^{T_{final}} \alpha(T) dT \right) \quad (4.9)$$

Where L in equation 4.9 is some characteristic dimension. If the Young's Moduli were assumed to be linear, but the coefficients of thermal expansion were allowed to vary nonlinearly, the effect on the quadratic temperature coefficient of frequency is found to be approximately $1.5 \text{ ppb}/^{\circ}C^2$. Since the Young's Modulus of silicon is known to have a much larger quadratic temperature coefficient, approximately $-56 \text{ ppb}/^{\circ}C^2$, it is hypothesized that the quadratic temperature dependence of Young's Modulus dominates the quadratic temperature coefficient of frequency. Unfortunately, only a single literature value for the quadratic temperature coefficient of Young's Modulus for fused quartz was found, approximately $-137 \text{ ppb}/^{\circ}C^2$ [61].

The measured quadratic temperature coefficient of frequency for the composite oriented along the $\langle 110 \rangle$ and $\langle 100 \rangle$ direction was found to be approximately $-21 \text{ ppb}/^{\circ}C^2$ and $-25 \text{ ppb}/^{\circ}C^2$ at $25^{\circ}C$, respectively. It is interesting to note that the measured quadratic temperature coefficient of frequency of silicon oriented along the $\langle 110 \rangle$ and $\langle 100 \rangle$ directions is $-26.4 \text{ ppb}/^{\circ}C^2$ and $-32 \text{ ppb}/^{\circ}C^2$ at $25^{\circ}C$, respectively. The difference in the TCf_2 for silicon in the different orientations is currently not

explained by using the published temperature coefficients of elastic constants of silicon by Bourgeois et al. [15]. Since the composite quadratic temperature coefficient of frequency will depend on a combination of silicon and silicon dioxide properties, this indicates that silicon dioxide could have a more positive quadratic temperature dependence than silicon.

4.3.3 Extracting Temperature Dependent Properties

One of the ways to extract the temperature dependencies of silicon dioxide is to fit the temperature dependence of the ideal ratio. The ideal ratio is defined at a particular temperature, the turnover temperature (T_m) to be exact. From chapter 2 the ideal ratio is given by:

$$r^*|_{T_m} = -\frac{TCf_{1,SiO_2}|_{T_m}}{TCf_{1,Si}|_{T_m}} \quad (4.10)$$

The linear temperature coefficients of frequency in equation 4.10 can be written in terms of the linear and quadratic temperature coefficients at room temperature (T_o):

$$r^*|_{T_m} = \frac{\left(\frac{f_{SiO_2}(T_o)}{f_{SiO_2}(T_m)}\right) \left(TCf_{1,SiO_2}|_{T_m} + 2TCf_{2,SiO_2}|_{T_m}(T_m - T_o) \right)}{\left(\frac{f_{Si}(T_o)}{f_{Si}(T_m)}\right) \left(TCf_{1,Si}|_{T_m} + 2TCf_{2,Si}|_{T_m}(T_m - T_o) \right)} \quad (4.11)$$

The frequency fractions in equation 4.11 can also be expanded using Taylor expansion such that equation 4.11 is only a function of the linear and quadratic temperature coefficients of silicon and silicon dioxide. The values for the silicon temperature coefficients ($TCf_{1,Si,<110>} \approx -31.4$ ppm/ $^{\circ}$ C, $TCf_{2,Si,<110>} \approx -26.4$ ppb/ $^{\circ}$ C²) were previously extracted from silicon resonator measurements. Using the data from composite resonators next to each other on the wafer, such as shown in Figure 4.11, the turnover temperature versus the ideal ratio (r^*) can be fit to using equation 4.11 (Figure 4.19).

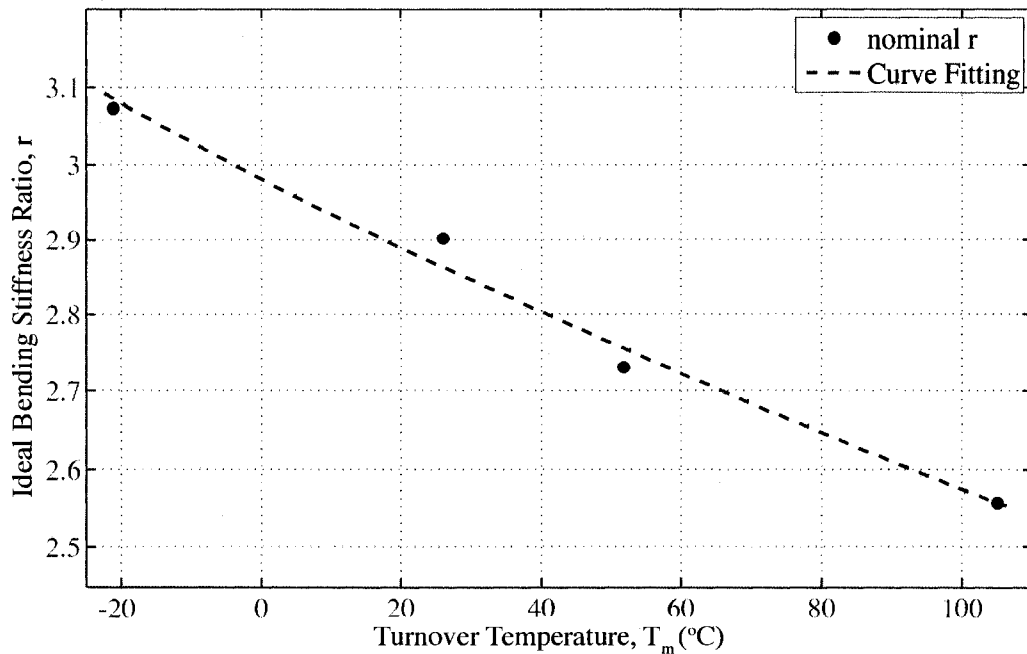


Figure 4.19: Ideal ratio versus turnover temperature and fit.

The extracted TCf_{1,SiO_2} is 90 ppm/°C with 95% confidence bounds of 87.7 ppm/°C to 92.4 ppm/°C. Using the literature value of 0.58 ppm/°C for the thermal expansion of silicon dioxide at room temperature, the nominal TCE_{1,SiO_2} is 179.4 ppm/°C. Note that an uncertainty in the actual ratio of approximately $\pm 3\%$, which is discussed in section 4.4, will further increase the uncertainty in the extracted TCE values by $\approx \pm 3\%$ or ± 5.4 ppm/°C.

The extracted TCf_{2,SiO_2} value had a large range with a nominal value of +12.6 ppb/°C² and 95% confidence bounds of -13.4 ppb/°C² to +38.6 ppb/°C². The TCE_{2,SiO_2} is approximately twice the extracted TCf_{2,SiO_2} , and is also widely varying. Although these values are more positive than the TCf_2 of silicon, as the measurements predict, the exact value could not be extracted. In exploring the cause of this variation, it is interesting to note that the change of the ideal ratio, r^* , over turnover temperatures (Figure 4.19), can be approximated by a line. In doing so, a simplified analytical expression for the temperature coefficient of the ideal ratio can be expressed as:

$$TCr^* = \frac{1}{r^*} \frac{\partial r^*}{\partial T} \approx 2 \left(\frac{TCf_{2,SiO_2}}{TCf_{1,SiO_2}} - \frac{TCf_{2,Si}}{TCf_{1,Si}} \right) \quad (4.12)$$

Rewriting the equation to solve for the properties of silicon dioxide:

$$\frac{TCf_{2,SiO_2}}{TCf_{1,SiO_2}} = \frac{TCr^*}{2} + \frac{TCf_{2,Si}}{TCf_{1,Si}} \quad (4.13)$$

Within 95% confidence bounds, the TCr^* is between -0.09% to -0.2%. The ratio of the silicon temperature coefficients in equation 4.13, $\frac{TCf_{2,Si}}{TCf_{1,Si}}$, extracted from previous measurements, is approximately 0.05%. By comparison to $\frac{1}{2}TCr^*$, small variation in the slope of TCr^* result in large variations from positive to negative in the ratio of the silicon dioxide temperature coefficients. One interpretation of this result is that the quadratic temperature coefficients of silicon material properties are dominating and making extraction of the quadratic temperature coefficients of silicon dioxide material properties difficult.

It is important to note the temperature coefficient of the ideal ratio, TCr^* , is approximately 4 to 8 times larger than the temperature coefficient of the ratio, r , found in in the previous section ($TCr \approx -242$ ppm/°C). The implication is that the higher order material properties, particularly the quadratic temperature coefficients of Young's Modulus, are determining the tunability of the turnover temperature as well as the quadratic frequency-temperature behavior of the composite resonator.

4.4 Effect of Fabrication Variation

The variation in frequency of identical DETF resonators across a 4" wafer was measured to be approximately 2%. It is believed that this variation is due to manufacturing variations, particularly during the lithography and deep reactive ion etch definition of the resonator. Variations in the width of the beams and the thickness of the oxide would lead to a variation in the ratio, r , and thus result in a different turnover temperature. By examining the turnover temperatures across the wafer, we find that lithographically identical resonators have different turnover temperatures (Figure 4.20). For example, resonators with an approximated ratio of 2.55 have a 50

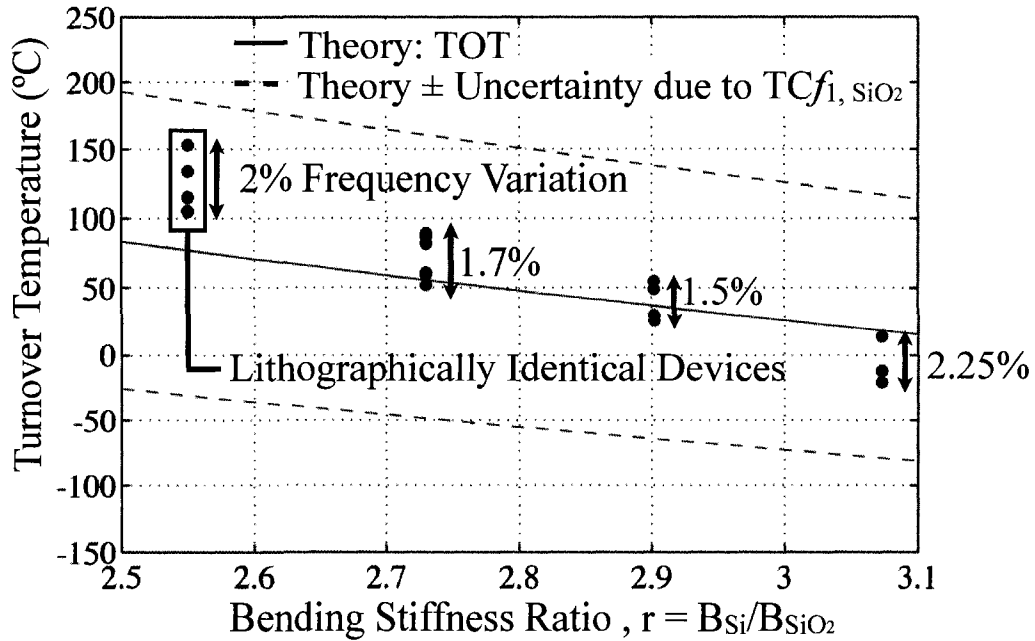


Figure 4.20: Turnover temperature plotted for lithographically identical $\langle 110 \rangle$ oriented DETF resonators.

°C variation in the turnover temperature .

A correlation can be established between the frequency of the DETF and its turnover temperature. Simply, a thinner beam width, results in a lower frequency, a lower ratio of silicon to silicon dioxide bending stiffness, and thus a higher turnover temperature. Assuming material properties are constant across the wafer, the variation in the bending stiffness ratio is can be approximately defined as:

$$\frac{\delta r}{r} = \sqrt{\left(\frac{\partial r}{\partial w_{Si}} \delta w_{Si}\right)^2 + \left(\frac{\partial r}{\partial h_{Si}} \delta h_{Si}\right)^2 + \left(\frac{\partial r}{\partial t_{SiO_2}} \delta t_{SiO_2}\right)^2} \quad (4.14)$$

where w_{Si} and δw_{Si} are the silicon beam width and variation, h_{Si} and δh_{Si} are the silicon beam height and variation, and t_{SiO_2} and δt_{SiO_2} are the silicon dioxide thickness and variation. Evaluation of equation 4.14 is best done with a computer since there are many cross-coupling terms. However, a rough approximation yields that the variation is primarily proportional to the variations in the silicon width and

silicon dioxide thickness:

$$\frac{\delta r}{r} \approx \sqrt{\left(\frac{\delta w_{Si}}{w_{Si}}\right)^2 + \left(\frac{\delta t_{SiO_2}}{t_{SiO_2}}\right)^2} \quad (4.15)$$

To account for this dependence, the average frequency of lithographically identical DETF resonators was found. Deviation from the average frequency was assumed to be due to only width variations. The width and corresponding ratio, r , was determined and the data replotted with new ratio values (Figure 4.21). A $\pm 2\%$ variation in the width accounts for approximately $\pm 2.2\%$ of variation in r . However, if both the width and silicon dioxide thickness are allowed to vary by $\pm 2\%$, then r can vary as much as $\pm 3.3\%$. This type of variation could account for the 50°C variation in the turnover temperature observed. If the silicon beam width and silicon dioxide thickness could be controlled to within $\pm 1\%$ of a nominal value, the resulting variation in the ratio r would be approximately $\pm 1.6\%$ and the resulting turnover temperature variation would be approximately $\pm 10^\circ\text{C}$.

The ability to design resonators with a turnover temperature at an elevated temperature is very desirable for integration with oven control temperature compensation techniques. In oven-controlled compensation, maintaining the temperature of the resonator at the turnover where the linear temperature coefficient of frequency is zero can further improve the temperature-frequency stability.

For example, if a silicon resonator were maintained within $\pm 0.1^\circ\text{C}$ around a nominal temperature, then the error in frequency would be within ± 3 ppm due to the approximately -30 ppm/ $^\circ\text{C}$ linear temperature coefficient of frequency. By comparison, if a silicon-silicon dioxide composite resonator were maintained within $\pm 0.1^\circ\text{C}$ of its turnover temperature, the resulting error in frequency would be ± 0.1 ppb due to the -20 ppb/ $^\circ\text{C}^2$ quadratic temperature coefficient of frequency. In practice it might be difficult to operate at the ideal temperature unless each device is calibrated over temperature to determine its turnover. This type of calibration can be costly, and operation away from the ideal temperature might be necessary. If the turnover temperature variation across the wafer is large, the ± 0.1 ppb frequency stability is

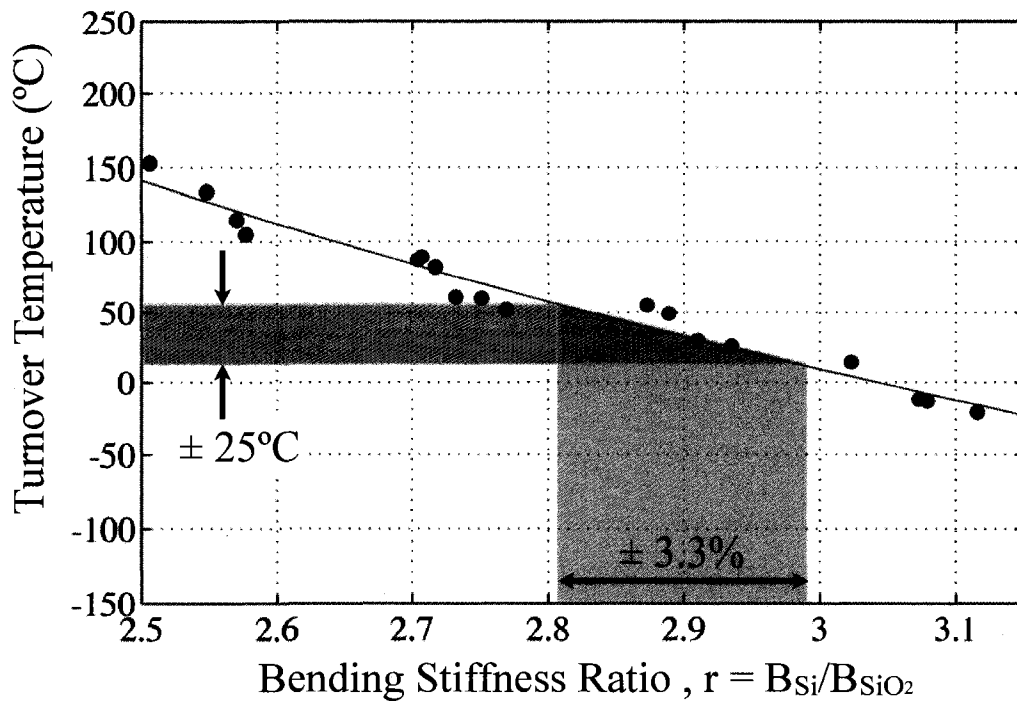


Figure 4.21: Variation in the turnover temperature due to variation in the ratio, r .

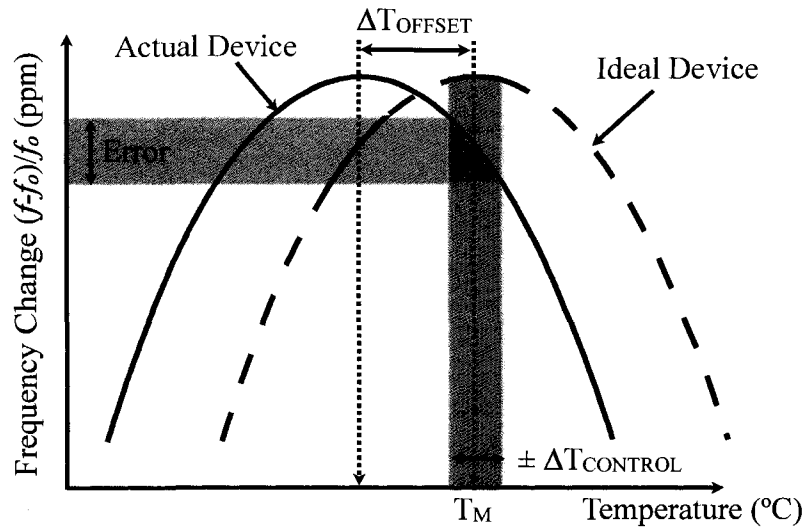


Figure 4.22: Oven-control of composite resonator away from turnover temperature leads to reduced frequency stability.

difficult to achieve.

How much error would result from operating the resonator with a ΔT_{offset} from the oven temperature set point by using a temperature controller capable of maintaining the resonator within $\pm T_{\text{control}}$ of the oven set point (see Figure 4.22)? Figure 4.23 compares the frequency stability versus temperature controller capability for a silicon resonator and three composite resonators with turnover temperatures at different ΔT_{offset} from the oven set point. To be competitive with the oven-controlled crystal oscillator (OCXO), the frequency stability must be less than 0.01 ppm. An oven controlled silicon resonator can not be competitive with an OCXO even with a milliKelvin precision temperature controller. Most commercial temperature sensors will not be able to control the temperature to better than ± 0.1 °C. To be competitive with an OCXO, a non-calibrated wafer will need to have less than ± 1 °C variation in turnover temperature. Since that is not currently feasible, a wafer with ± 10 °C variation in turnover temperature would need temperature control of approximately 0.01 °C. Although this is not possible with commercial temperature sensors, this level of temperature control has been recently shown by using the resonators as temperature

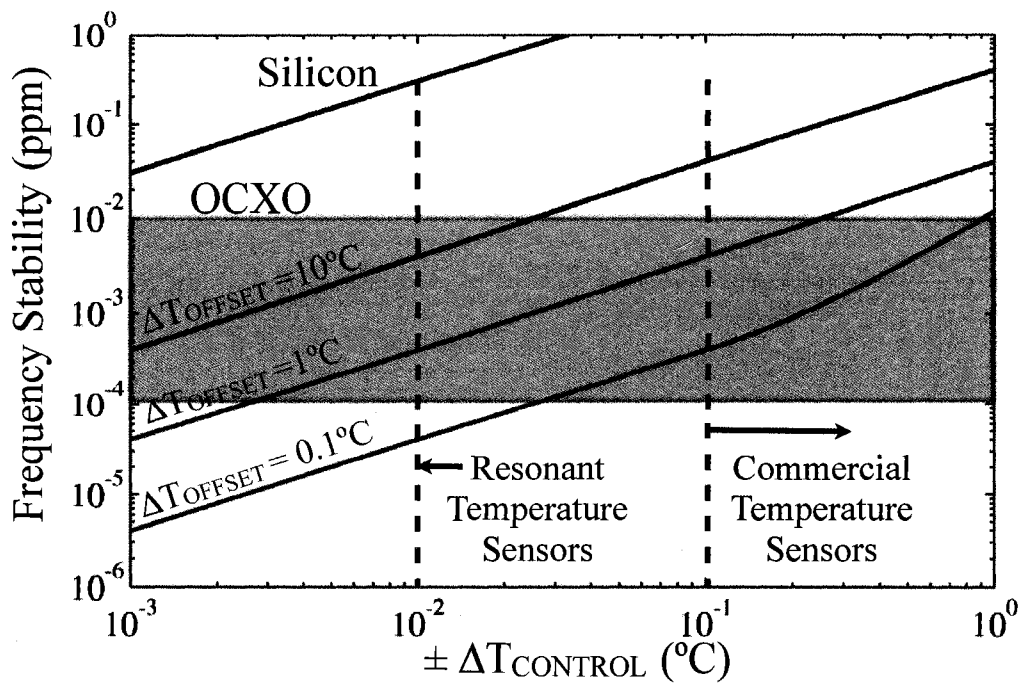


Figure 4.23: Achievable frequency stability for oven-compensation of composite resonators away from the turnover temperature.

sensors [44].

4.5 Summary

Flexural mode and extensional mode composite resonators were tested over more than 150 °C temperature range. "Zero-TCF" flexural mode composite resonators were demonstrated with frequency variations of less than 200 ppm over a -55 °C to 125 °C temperature range. The linear temperature coefficient of frequency was found to be zero at a particular temperature - the turnover temperature. The resulting frequency-temperature behavior was characterized by a quadratic temperature coefficient of frequency of approximately -20 ppb/°C². By examining the mechanisms contributing to this higher order behavior, it was determined the the quadratic temperature coefficients of the Young's Modulus are primarily responsible. Small modifications in the ration of composition of the silicon to silicon dioxide portions of the resonant structure were found to translate the turnover temperature. Resonators with turnover temperatures at high temperatures, greater than 100 °C, are beneficial for combining with active oven-controlled compensation schemes to further reduce the frequency sensitivity. However, variations in manufacturing resulted in large variations in the turnover temperature for identically designed resonators. This variation constrains the type of thermometry necessary for oven control such that a temperature sensor with better than 0.1 °C resolution is needed to attain OCXO levels of frequency stability.

4.6 Acknowledgements

Measurements of the frequency-temperature behavior of resonators was greatly helped by the GPIB code and amplifier board developed by Matt Hopcroft and Aaron Partridge. The extensional mode resonator was designed by Saurabh Chandorkar. The amplifier board for differential measurements of the extensional mode resonator was designed by Jim Salvia.

Chapter 5

Stability of Composite Resonators

The development of composite resonators was motivated by the need for temperature stable silicon-based resonators. As discussed in Chapter 1, temperature stability is just one of the requirements for a frequency reference [89]. Other critical factors include long term frequency stability, phase noise, vibration and shock sensitivity, and stress sensitivity.

In this chapter we will primarily focus on long term frequency stability and factors influencing the phase noise in composite resonators. Vibration and shock sensitivity for composite resonators should be very similar to vibration and shock sensitivity of similarly designed silicon resonators [4, 44], since the sensitivity to acceleration has not been significantly modified. However, the introduction of the silicon dioxide around the silicon resonator necessitates a re-examination of the effect of this dielectric coating on the long term stability and phase noise in this new architecture.

5.1 Short Term Stability

Phase noise is a measure of short term frequency stability of a frequency reference. At frequencies far from the carrier (the frequency of the resonator) the phase noise can be described by the ratio of the current noise density to the current generated by the resonator [59].

$$L(f) = 20 \log \left(\frac{i_n}{i_{res}} \right) \quad (5.1)$$

The current noise density, i_n , is determined by the electronics in the oscillator, such as the noise of the first stage amplifiers. For low-noise amplifiers, i_n is in the range of picoAmperes. The current generated by the resonator, which is measured by the network analyzer at the output electrode, has a fundamental dependence on the quality factor of the resonator and the effectiveness of the electrostatic transduction. Increasing the current generated by the resonator, also referred to as current handling, is a central issue in the commercialization of silicon resonators for large volume applications, such as wireless communication.

The current generated by the resonator can be described in terms of a motional resistance, R_m [58]:

$$i_{res} = \frac{v_{ac}}{R_m} \quad (5.2)$$

where

$$R_m = \frac{2\pi f m}{Q\eta^2} \quad (5.3)$$

In equation 5.3, f is the frequency of the resonator, m is the mass, Q is the quality factor, and η is the electrostatic transduction factor defined as:

$$\eta = V_{bias} \frac{\partial C}{\partial v} \quad (5.4)$$

In equation 5.4, V_{bias} is the bias voltage applied to the resonator, C is the capacitor formed between the resonator and the electrodes, and v is the displacement of the resonator. Phase noise and the effects of nonlinearities in electrostatically transduced silicon resonators have been studied in depth [3] [47]. In this section we will look at the effect of the silicon dioxide dielectric coating on critical parameters such as the quality factor and transduction factor which determine the power handling of the resonator.

5.1.1 Composite Quality Factor

As discussed in Chapter 1, the quality factor in double ended tuning fork resonators in low-pressure environments is dominated by thermoelastic dissipation (TED) [21], [23]. Thermoelastic dissipation is an energy loss mechanism caused by interaction of thermal modes and mechanical modes formed during vibration of the resonator. Strain gradients formed during resonator vibration result in thermal gradients due to the compression and tension of the crystal lattice. The resulting heat conduction is an entropy generation process that results in energy loss in the resonator.

Although the full derivation of the quality factor in single material or composite resonators is beyond the scope of this work, quality factor measurements of single crystal silicon and composite silicon-silicon dioxide resonators are compared in this section. Double ended tuning fork resonators were designed such that the width of the resonator beam is kept constant at $10\ \mu\text{m}$ and the length of the resonant beam is varied from $220\ \mu\text{m}$ to $395\ \mu\text{m}$. At each unique length, silicon resonators and identically defined composite resonators with a $0.42\ \mu\text{m}$ of silicon dioxide coating were measured.

Keeping the width of the resonator constant ensures that the thermal modes of the resonators are identical. However changing the length of the resonator will change the frequency of vibration. In doing so, the interaction between the thermal and mechanical mode is varied. The lowest quality factor is attained when the overlap between the thermal and mechanical modes is maximized.

To remove the effect of gas damping by the residual gas in the cavity, after completion of the encapsulation, a focused ion beam was used to break into the cavity of the resonator and expose it to the environment (Figure 5.1). The packaged and wire-bonded die were then placed in a vacuum chamber where the frequency and quality factor were measured using a network analyzer as described in Chapter 4. The measured quality factor of composite resonators is generally higher than silicon resonators by 15% to 50% (Figure 5.2).

The entropy generated due to thermoelastic dissipation also depends on material

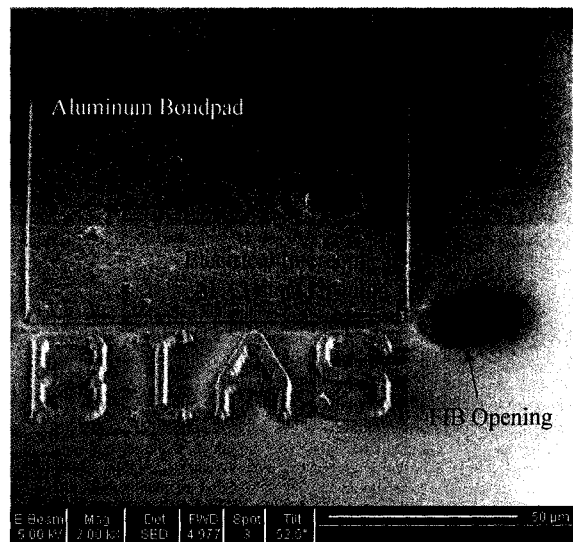


Figure 5.1: Focused Ion Beam (FIB) opening of resonator cavity to expose resonator to the environment.

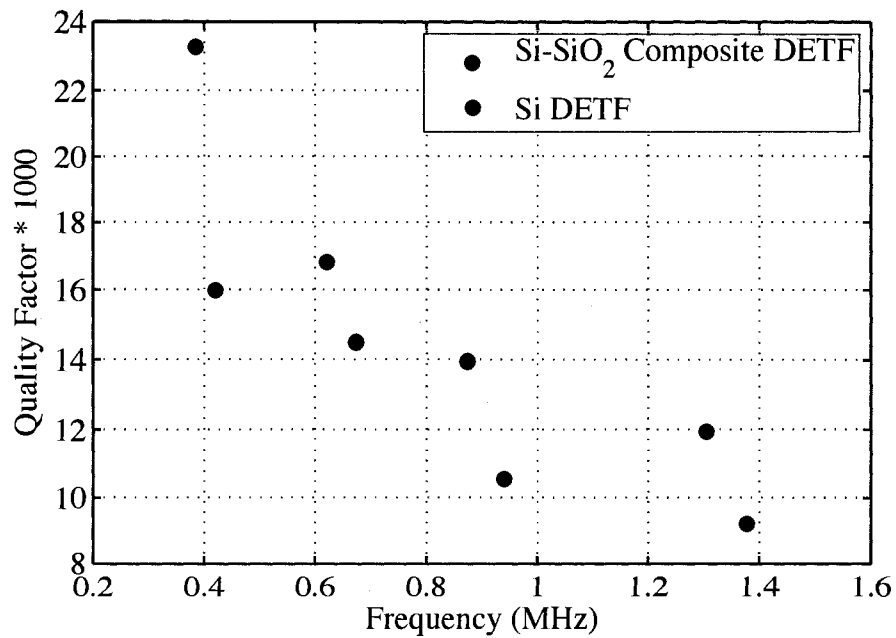


Figure 5.2: Comparison of quality factor measurement for various silicon and composite resonators.

properties. For a single material resonator, the entropy is proportional to [23]:

$$S \propto \frac{\alpha^2 B^2}{c_v} \quad (5.5)$$

In equation 5.5, α is the coefficient of thermal expansion, B is the bulk modulus, and c_v is the heat capacity per unit volume of the material. The coefficient of thermal expansion for silicon is approximately 4.5 times larger than silicon dioxide. The Bulk modulus of silicon is approximately 2.5 times larger. The heat capacity of silicon is 0.4 times that of silicon dioxide. For identically designed silicon and silicon dioxide resonators, the quality factor of the silicon dioxide resonator would be 300 times larger than silicon. Since the thermal-mechanical properties of crystalline quartz are similar to amorphous silicon dioxide, quartz crystal resonators have been manufactured with quality factors of up to 1 million [90]. It is hypothesized that the addition of silicon dioxide to the resonator structure improves the quality factor of the resonator due to the reduced thermal expansion and bulk modulus of silicon dioxide.

5.1.2 Electrostatic Transduction in Composite Resonators

Increasing the electrostatic transduction in MEMS resonators results in reduced motional resistance, increased current handling, and thus reduced phase noise. In silicon resonators the electrostatic transduction factor depends on the capacitor formed between the moving structure and the sense electrode (see equation 1.3). Taking the derivative with respect to displacement of equation 1.3, assuming small deflections, and ignoring higher order terms, the electrostatic transduction factor for a single material resonator is:

$$\eta \approx V_{bias} \frac{\epsilon_o A_e}{g^2} \quad (5.6)$$

In equation 5.6, ϵ_o is the permittivity of free space, A_e is the electrostatic area, and g is the gap between the resonator and electrode. Following a similar analysis as presented in Chapter 1, the electrostatic system for a differential element of the

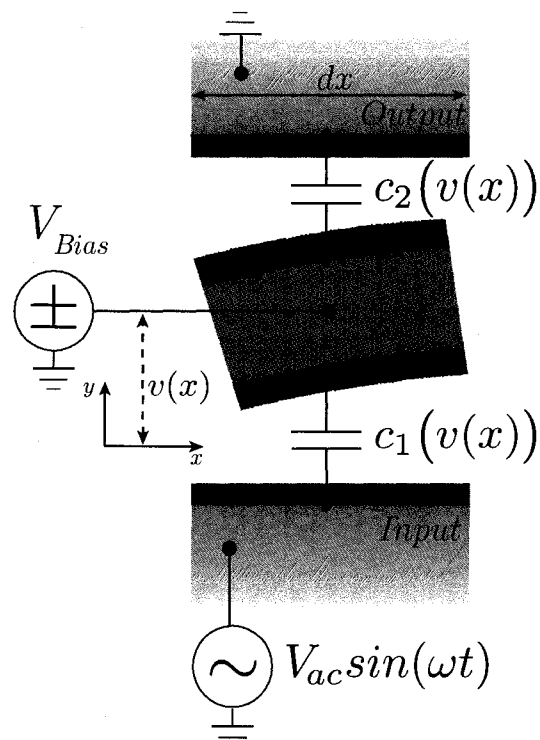


Figure 5.3: Differential element of composite flexural mode resonator and electrodes.

composite resonator is shown in Figure 5.3.

The capacitors that are formed between the resonator and the electrodes are described by:

$$\frac{1}{c_1(v)} = \frac{(g - 1.08t) + v(x)}{\varepsilon_o h dx} + \frac{2t}{\varepsilon_o \kappa_{ox} h dx} \quad (5.7)$$

$$\frac{1}{c_2(v)} = \frac{(g - 1.08t) - v(x)}{\varepsilon_o h dx} + \frac{2t}{\varepsilon_o \kappa_{ox} h dx} \quad (5.8)$$

In equations 5.7 and 5.8, g is the electrostatic gap prior to thermal oxidation, h is the height of the beam, t is the thickness of the thermally grown silicon dioxide on the sides of the beams, ε_o is the permittivity of free space, and κ_{ox} is the dielectric constant of silicon dioxide, approximately 3.9 [62]. After thermal oxidation, the electrostatic gap is reduced due to the growth of silicon dioxide by approximately 1.08 times the thickness of the silicon dioxide layer. This is due to approximately 54% of the thickness which grows outward from the original silicon surface [75].

Using Taylor expressions, equations 5.7 and 5.8 can be rewritten as:

$$c_1(v) = \frac{\kappa \varepsilon_o h dx}{g} \sum_{n=1}^{\infty} \left(\frac{\kappa v}{g} \right)^n \quad (5.9)$$

$$c_2(v) = \frac{\kappa \varepsilon_o h dx}{g} \sum_{n=1}^{\infty} \left(-\frac{\kappa v}{g} \right)^n \quad (5.10)$$

where

$$\kappa = \frac{1}{1 + \frac{t}{g} \left(\frac{2}{\kappa_{ox}} - 1.08 \right)} \quad (5.11)$$

The maximum thickness of silicon dioxide that can be grown is slightly smaller than the electrostatic gap ($t = g/1.08$). In equation 5.11, the ratio of the thickness of silicon dioxide to the electrostatic gap is limited to $0 < \frac{t}{g} < \sim 0.93$. Furthermore, since $\frac{2}{\kappa_{ox}} < 1.08$, the denominator in equation 5.11 will be less than 1 and thus κ will be greater than 1, indicating an improved transduction factor. Taking the derivative of equation 5.9, assuming small deflections, and ignoring higher order terms, the electrostatic transduction of a composite resonator is approximately:

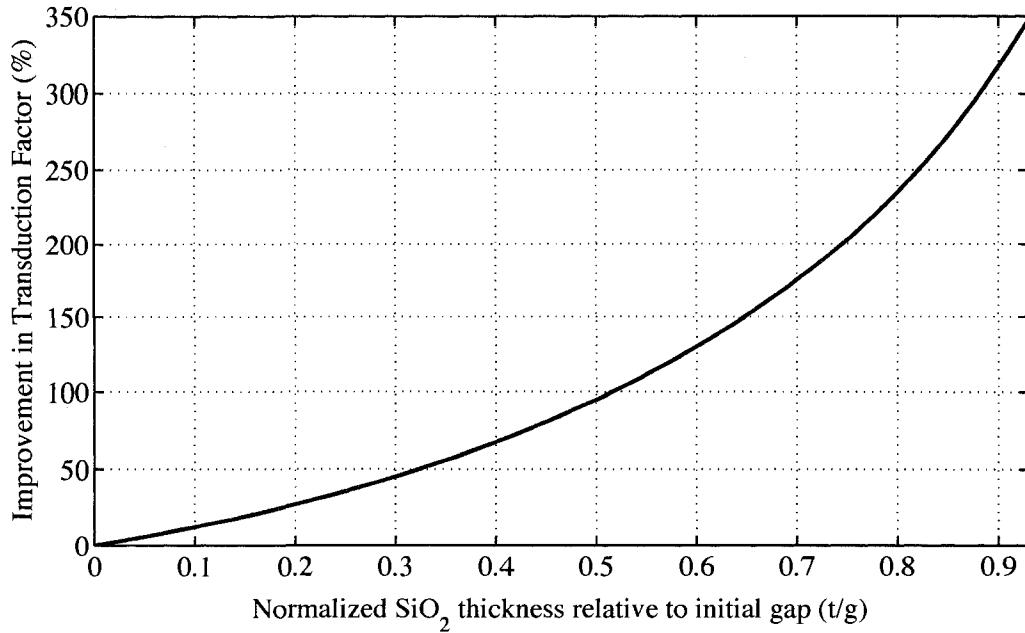


Figure 5.4: Improvement in transduction factor after thermal oxidation.

$$\eta_{composite} \approx V_{Bias} \frac{\kappa^2 \epsilon_o A_e}{g^2} \quad (5.12)$$

By comparison to the electrostatic transduction factor for a silicon resonator, equation 5.6, this indicates that the composite electrostatic resonator will have a higher electrostatic transduction factor than an identically designed but not thermally oxidized silicon resonator. For resonators with identical electrostatic transduction areas and initial electrostatic gap, Figure 5.4 shows the level of improvement in η for a composite resonator.

For a $0.48 \mu\text{m}$ silicon dioxide coating on the $\langle 110 \rangle$ silicon surface and an initial gap of approximately $1.8 \mu\text{m}$ ($1.5 \mu\text{m}$ defined + $0.3 \mu\text{m}$ blowout), a 25% increase in η expected. With a 25% improvement in the transduction factor and a 30% improvement in quality factor, the power handling of the resonator improves by a factor of 2. The expected decrease in phase noise is approximately -6 dBc/Hz. Further improvements in phase noise are possible for thicker oxidations. However, thicker oxidations complicate the manufacturing process and results in lower yields. The

highest achieved ratio of silicon dioxide thickness to gap width in this processes was approximately 0.36. The analysis indicates that improved transduction factors are possible by using higher dielectric constants in the electrostatic gap. Research into electrostatic gaps completely filled with high- κ dielectric materials is currently ongoing [9, 10, 92].

5.2 Long Term Stability of Frequency

Candler et al. [22] and Kim et al. [50] have previously shown that silicon resonators encapsulated using the “epi-seal” process show remarkable stability to less than ± 3 ppm at room temperature for approximately one year. The two factors critical in achieving this level of stability are the simultaneous removal of native oxide and contaminants on the silicon surface, thus revealing pristine clean silicon resonators, and hermetic packaging using “epi-seal”. Although a similar hermetic package was used to fabricate composite resonators, the stability of a combined silicon - silicon dioxide resonator has not been shown. One concern is that dielectrics, such as silicon dioxide, have been known to get electrostatically charged when placed in an electric field. Since the composite resonators are electrostatically actuated, the long term stability of the devices must be monitored.

5.2.1 Constant Temperature

Using a similar setup as described in Chapter 4, multiple DETF resonators were monitored at a constant temperature of 36 °C for almost one year. Although the resonators were tested serially, the bias voltage was maintained at all times such that the electrostatic field within the gap was constantly present. Figures 5.5 through 5.12 show the long term frequency behavior. Silicon resonators were included as a reference (Figure 5.5). Identically designed composite DETF resonators from the same wafer are shown on the same plot. The nominal width of the beam, prior to lithography and etching, is indicated in the figure title. A total of 14 composite resonators with different frequencies and SiO₂ thickness are showing in Figures 5.6

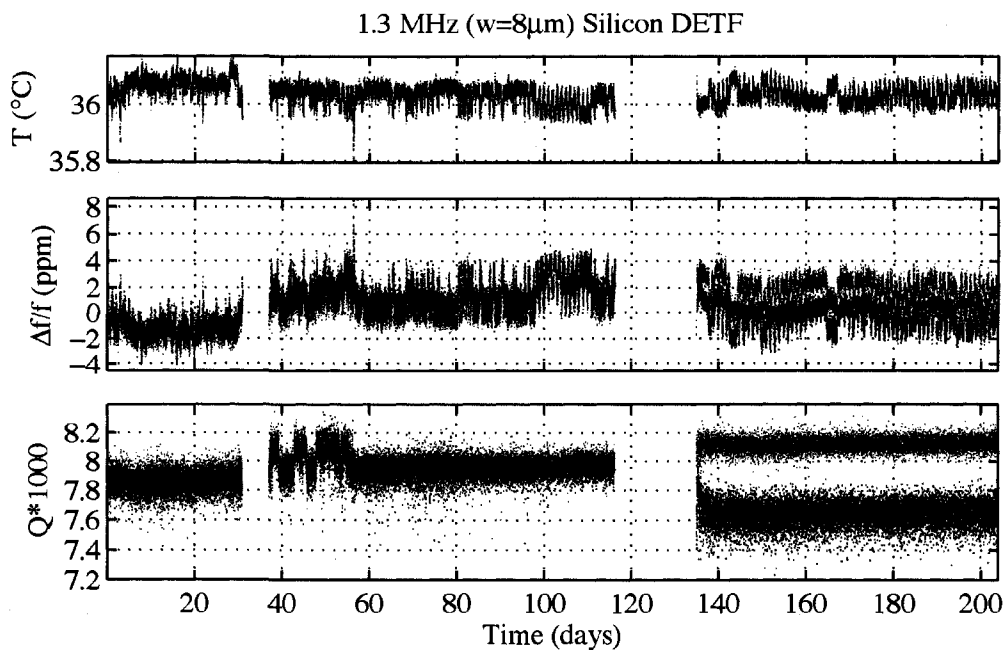


Figure 5.5: Stability of two Silicon 1.3 MHz DETF.

through 5.12. Gaps in the data correspond to maintenance of the setup. No other measurements were performed before the start of the experiment or during the gap times.

In Figure 5.5 the temperature varies by at most ± 0.2 °C. With a -30 ppm/°C temperature coefficient of frequency for silicon resonators, the silicon resonator exhibits frequency variations of approximately ± 6 ppm. Furthermore, noise at the peak of the response introduces additional noise into the data (Figure 5.13). To remove this, the peak is fitted using a polynomial and the frequency at maximum amplitude is extracted. Although more sophisticated models for fitting were considered, it was determined that a simple quadratic polynomial fit in a very limited frequency range

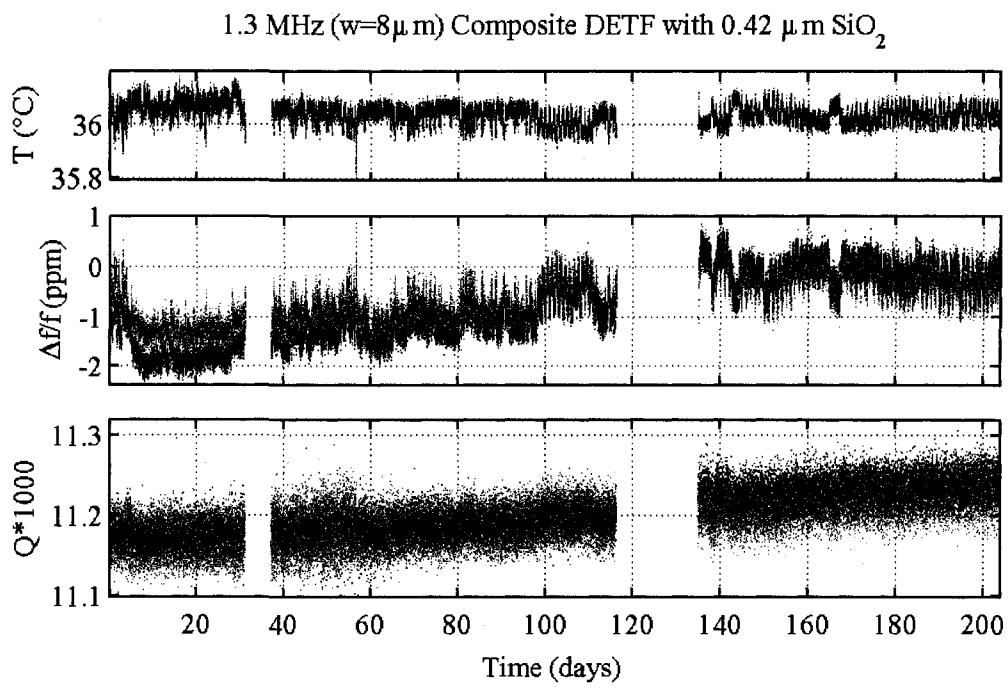


Figure 5.6: Stability of two 1.3 MHz DETF with a $0.42\ \mu\text{m}\ \text{SiO}_2$.

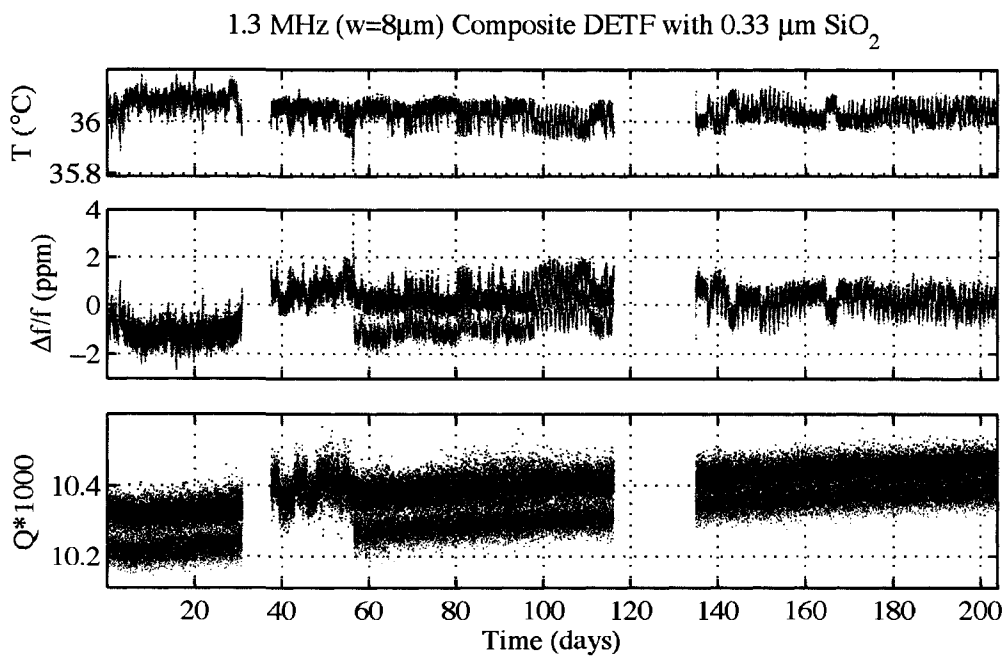


Figure 5.7: Stability of two 1.3 MHz DETF with a $0.33\ \mu\text{m}\ \text{SiO}_2$.

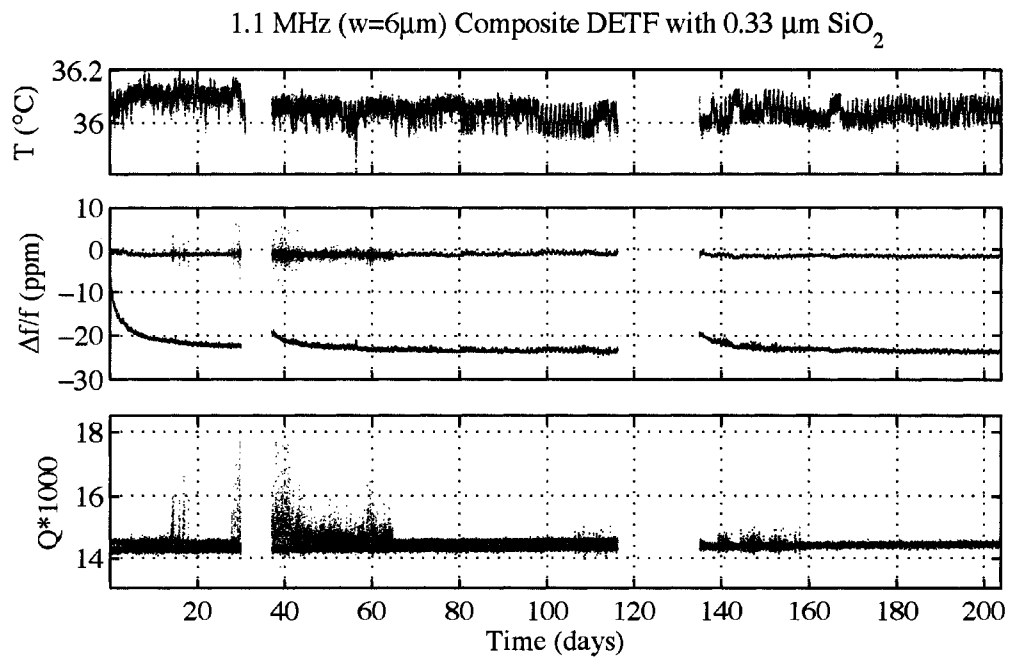


Figure 5.8: Stability of two 1.1 MHz DETF with a $0.33\ \mu\text{m}\ \text{SiO}_2$.

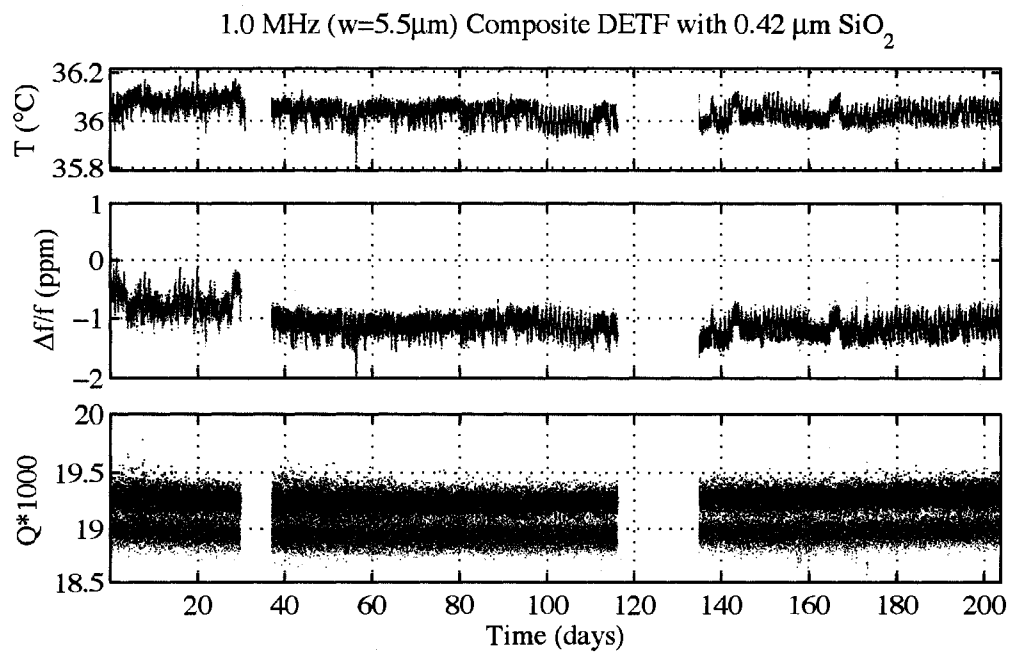
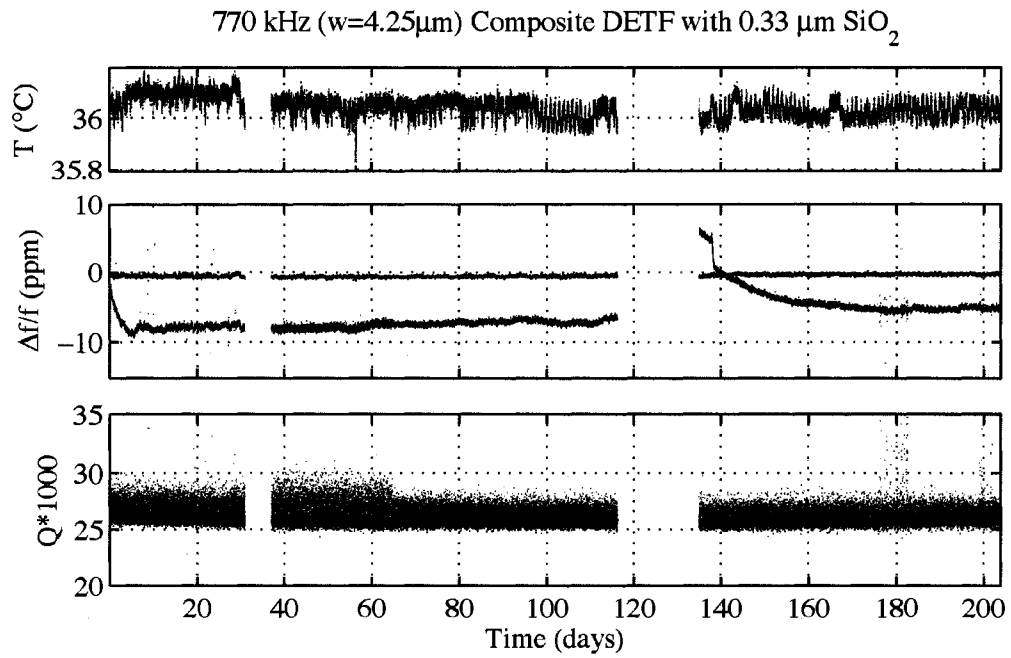
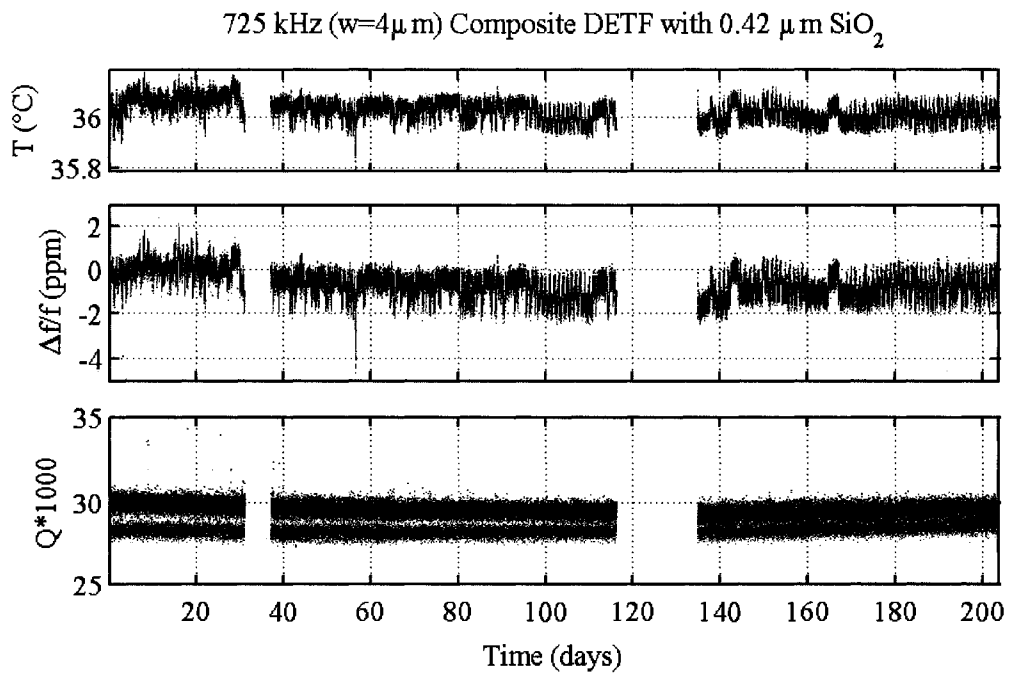


Figure 5.9: Stability of two 1.0 MHz DETF with a $0.42\ \mu\text{m}\ \text{SiO}_2$.

Figure 5.10: Stability of two 770 kHz DETF with a $0.33\mu\text{m SiO}_2$.Figure 5.11: Stability of three 725 kHz DETF with a $0.42\mu\text{m SiO}_2$.

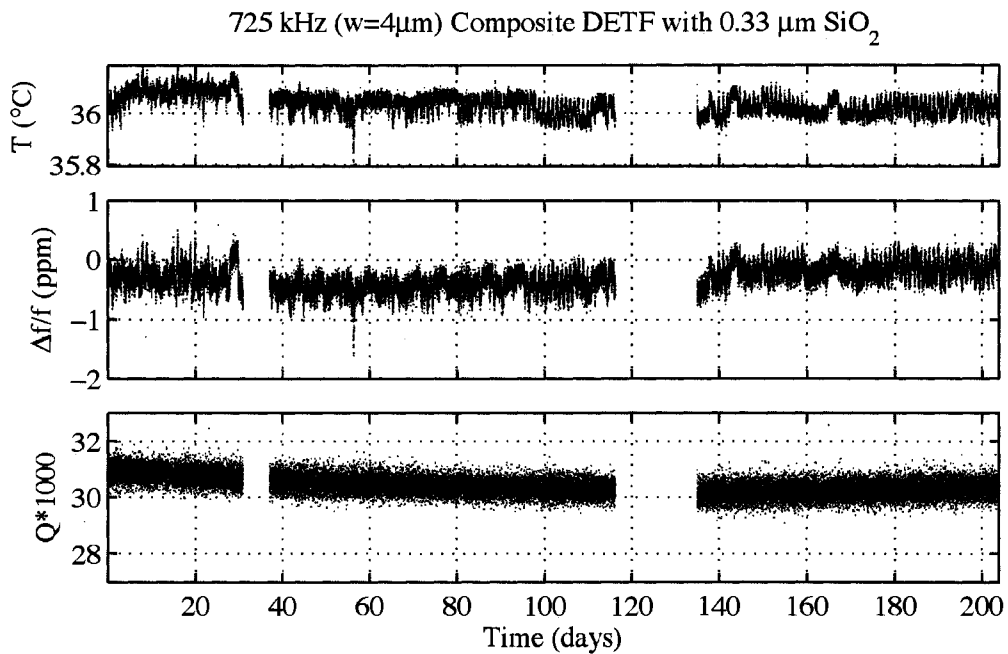


Figure 5.12: Stability of one 725 kHz DETF with a $0.33\ \mu\text{m}\ \text{SiO}_2$.

near the peak was sufficient.

Of the 14 composite resonators tested, 12 showed frequency stability to within ± 2 ppm. However, several devices showed significant drift on the order of tens of parts per million (Figures 5.8 and 5.10). For the two devices showing drift, there were also identical devices that did not show this level of drift. Since the silicon resonators do not exhibit this behavior, it is postulated that the drift is an effect of the presence of silicon dioxide. A possible mechanism is the presence of fixed or mobile charges in the dielectric. To test this hypothesis, changes in the electrostatic field were induced to monitor the effect on frequency. The results are presented in the following section.

5.2.2 Effect of Changing Electrostatic Field

To induce electrostatic field changes, the polarity of the bias voltage applied to the DETF resonators was alternated. Figure 5.14 shows the change in frequency of a silicon and composite resonator for different magnitudes of bias voltage and for different

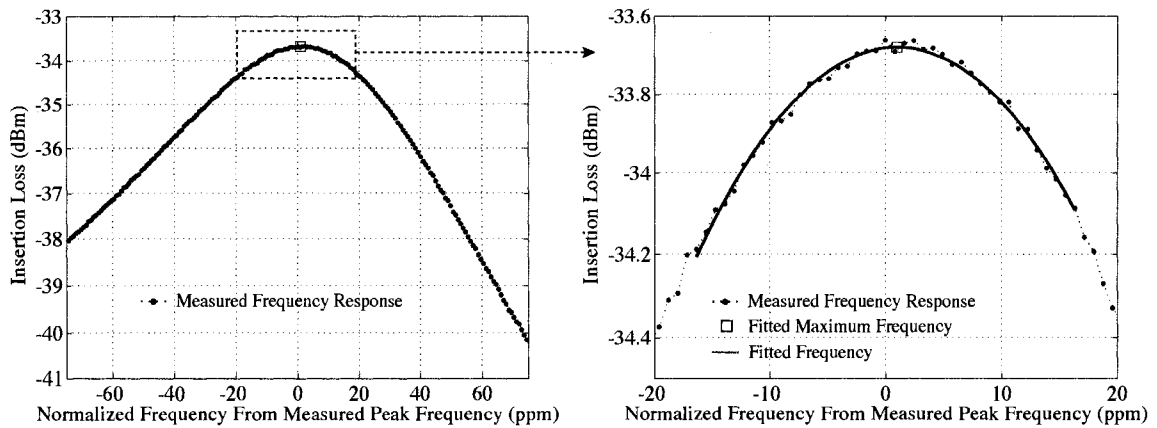


Figure 5.13: (Left) Frequency response of a DETF resonator. (Right) Frequency response is fitted near the maximum to remove noise. A new maximum frequency is extracted.

polarities. Changing bias voltage polarity has no effect on the silicon resonator. However, the composite resonator exhibits a frequency split between positive and negative voltages.

The lack of an effect on the silicon resonator can be explained by revisiting the effects of the non-linear electrostatic force on the frequency of the resonator from Chapter 1 equations 1.18 and 1.19. The frequency of the resonator is modified by the electrostatic spring stiffness rewritten here:

$$k_e = \frac{2\varepsilon_o A_e}{g^3} V_{bias}^2 \quad (5.13)$$

Recall that ε_o is the permittivity of free space, A_e is the electrostatic area, g is the electrostatic gap, and V_{bias} is the bias voltage applied to the resonator. Due to the the quadratic dependence on bias voltage, inversion of the polarity of bias does not change the electrostatic stiffness and therefore the frequency of the resonator is also unchanged.

In composite resonators, if a non-equal presence of charge develops on the dielectric surfaces between the resonator and electrodes this would result in the formation of an additional electrostatic field. The charges would act to modify the electrostatic

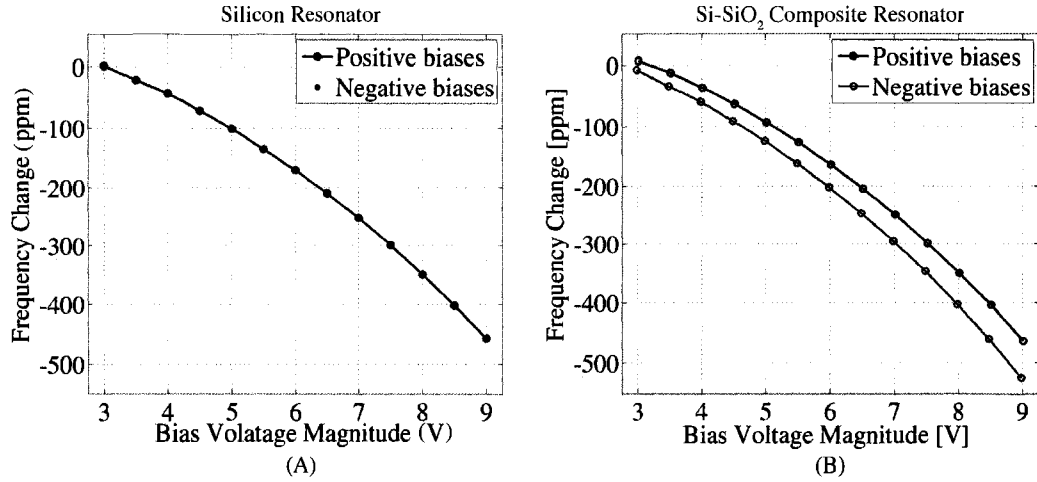


Figure 5.14: Change in frequency versus bias voltage for positive and negative polarity. (A) Silicon DETF Resonator (B) Composite DETF Resonator with $0.42 \mu\text{m}$ of SiO_2 .

field formed in gap. Following the analysis from Chapter 1, the non-time dependent electrostatic force on the composite beam can be written as:

$$f_{e,composite}(v) = \frac{\kappa^2 \epsilon_e h}{g^2} (V_{Bias} + \Delta V)^2 \sum_{n=1}^{\infty} 2n \left(\frac{\kappa v(x)}{g} \right)^{(2n-1)} dx \quad (5.14)$$

In equation 5.14, κ is defined as in equation 5.11. ΔV is the result of the modified electrostatic field due to the presence of charges in the dielectric. The modified electrostatic spring constant is the first term in the expansion of equation 5.14:

$$k_{e,composite} = \frac{2\kappa^3 \epsilon_o A_e}{g^3} (V_{bias} + \Delta V)^2 \quad (5.15)$$

From equation 5.15, application of a bias voltage of varying polarities would change the electrostatic stiffness and thus change the frequency of vibration. If charges are mobile, the electrostatic stiffness would change over time and cause a transient change in frequency. However, fixed charges would result in a change in frequency but no transient behavior. Interestingly, increasing the effectiveness of electrostatic transduction does not help to reduce this effect.

The effect of changing bias polarity was observed over a period of one day. While

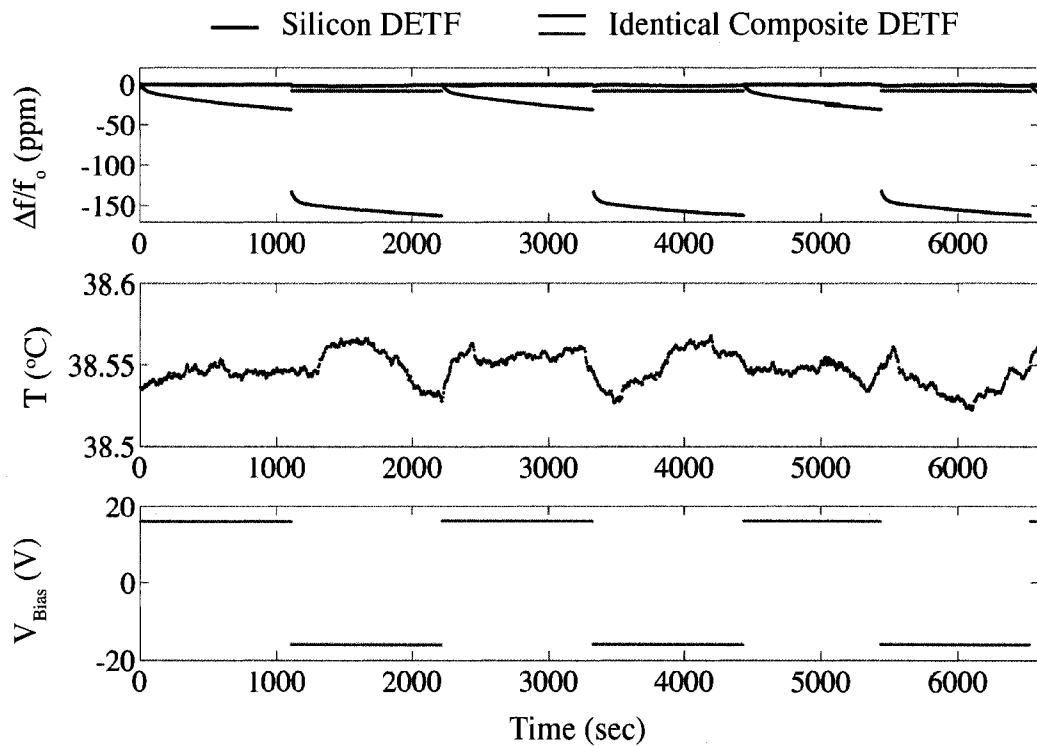


Figure 5.15: Long term stability with bias polarity switching of a silicon DETF and two identical composite DETFs.

temperature was maintained constant, three lithographically identical resonators experienced bias polarity inversion: one silicon resonator and two lithographically identical composite resonators. Repeatable behavior was observed of which two hours is plotted in Figure 5.15. For the silicon device, flipping the bias voltage had no effect. For one of the composite resonators, flipping the bias voltage resulted in a jump in frequency but no transient behavior. For the second composite resonator, flipping the bias voltage resulted in both a jump in frequency as well as a transient behavior.

Because this experiment results in a repeatable frequency behavior, it can be concluded that the effect is electrostatic in nature and not the result of fatigue, stress relaxation, or packaging defects. Since most applications use a constant bias source the primary concern is the reduction of this transient effect.

The nature of the charges that allow ΔV to develop is uncertain and is an ongoing

subject of research [6]. Having a combination of fixed and mobile charges could explain why some devices only see a change in frequency while others also experience transient behavior. Since identically designed devices on the same wafer show different types of behavior, this indicates that this type of variation maybe manufacturing-process induced. For example, ionic conduction could be the result of contamination or plasma damage. One possible cause is the plasma step just prior to sealing of the encapsulation which is used to remove the silicon dioxide on the top surface of the wafer (see Chapter 3). Because the vents are not sealed at this point, the plasma attacks the silicon dioxide just under the vent. Ions could be injected into the silicon dioxide coating the device or the electrodes.

Some literature [57, 2, 54] indicates that high temperature hydrogen annealing results in fixed positive charge generation in SiO_2 . Since the resonator is exposed to high temperature hydrogen during the “epi-seal” process, the effect of sealing temperature on composite resonator charging should be investigated. Although this could be an important mechanism, it would not explain the presence of mobile charges nor the large variation in the behavior of identical devices on the same wafer. However, the presence of fixed and mobile charges has not been attributed to a particular cause.

5.3 Summary

In this chapter key characteristics of the composite resonator were examined to determine the viability of the composite as a frequency reference. Of concern were short term and long term stability of the resonator. The short term stability is characterized by current handling of the resonator. Current handling depends on both the quality factor of the resonator as well as the electrostatic transduction factor. The presence of the silicon dioxide dielectric layer was found to improve both the quality factor due to the lower coefficient of thermal expansion and bulk modulus of silicon dioxide compared to silicon. The reduction in these material properties results in lower entropy generation due to thermo-elastic dissipation, and thus, higher quality factor. The transduction factor also increased due to an increase in the effective dielectric constant in the resonator electrostatic gap. Improvements of approximately

20% were seen in each.

The long term frequency stability of 2 silicon resonators and 14 composite resonators was monitored over a period longer than 200 days at constant 36 °C temperature. Silicon resonators exhibited frequency stability dominated by short term temperature fluctuations. Of the 14 composite resonators, 12 exhibited frequency stability to within 2 ppm. However, 2 composite resonators showed initial exponential frequency shifts on the order of 10's of ppm. A bias voltage polarity experiment was conducted which indicated a modified electrostatic field in composite resonators under polarity switching. A similar effect was not observed in silicon resonators. It is hypothesized that this result is the effect of charges trapped in the silicon-dioxide dielectric coating. Resonators exhibit the effects of both a fixed and transient charges. However, it is the transient behavior that must be addressed to retain the commercial viability of the composite resonators.

5.4 Acknowledgements

The measurement of quality factor would not have been possible without the generous help of Mariam Ziaei-Moayyed, J Provine, Roozbeh Parsa in using the FIB to open the resonator cavity. Quality factor measurements were done with the help of Saurabh Chandorkar. Measurement of the effect of bias polarity on the frequency of the resonators were performed by Gaurav Bahl.

Chapter 6

Thin Film Stress Temperature Compensation

One of the passive temperature compensation methods previously studied by researchers is the use of thermal stress to cancel the temperature dependence of frequency in silicon resonators with multiple anchors [39]. Thermal stresses that induce tension in the resonator as the temperature increases can increase the frequency of the resonator at the same rate as the frequency is decreasing due to decreases in Young's Modulus. To induce thermal stresses, materials with different coefficients of thermal expansion are used.

The "epi-seal" encapsulation of silicon resonators has been shown to yield stable frequency references [50]. As discussed previously, to a large degree this is due to having only exceptionally clean single-crystal silicon resonators hermetically sealed. The introduction of other materials, particularly those with large coefficients of thermal expansion, into the process could jeopardize not only the process but the stability of the resonator. To avoid introducing new materials into the encapsulation process, in this chapter we will demonstrate the use of die level packaging stress to temperature compensate hermetically sealed, single-crystal silicon double-ended tuning fork (DETF) resonators that are double anchored (Figure 1.7).

6.1 Package Level Stresses

Stresses that develop in the die can be analyzed at many different levels and can expand into a system level problem. From the thin films that make up the layers in the final resonator die, to the IC package that the resonator is glued to, to the printed circuit boards and the products which they are a part of, thermal stresses caused by the mismatch of coefficients of thermal expansion can couple into the stress in the resonator. The type of glue that is used to bond the resonator to the IC package and the flexibility of the leads of the IC package that connect it to the PCB can play a large role in the resonator's thermal stress. To model this system completely finite element software is necessary.

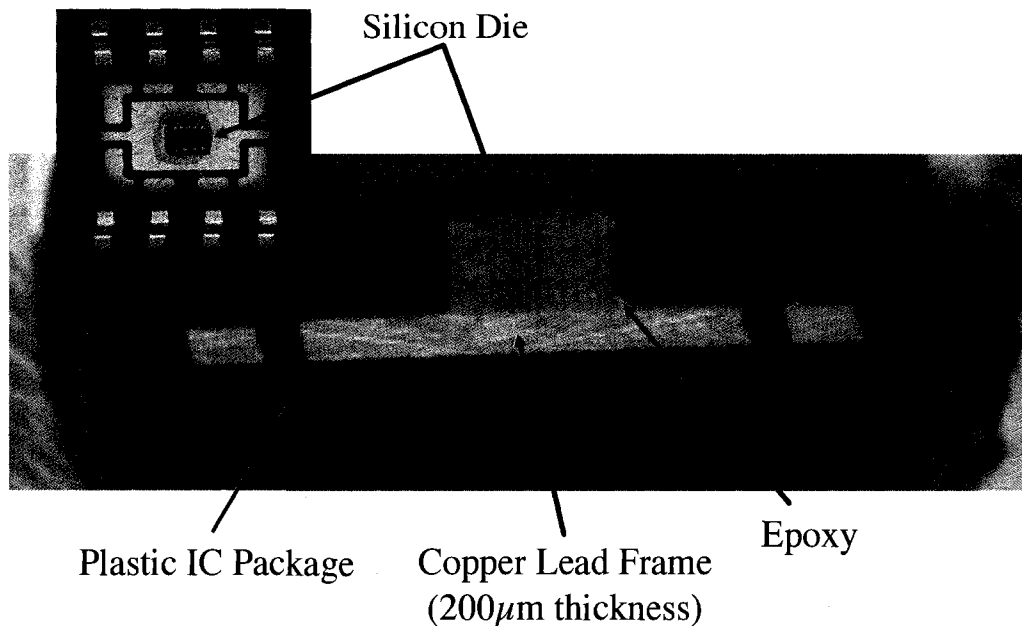


Figure 6.1: Cross section of resonator die epoxied to an IC package.

To illustrate the large degree to which thermal stresses can play a role in the frequency of the resonator, consider a double-anchored DETF resonator die that is bonded using silver epoxy to the copper paddle at the bottom of the IC package,

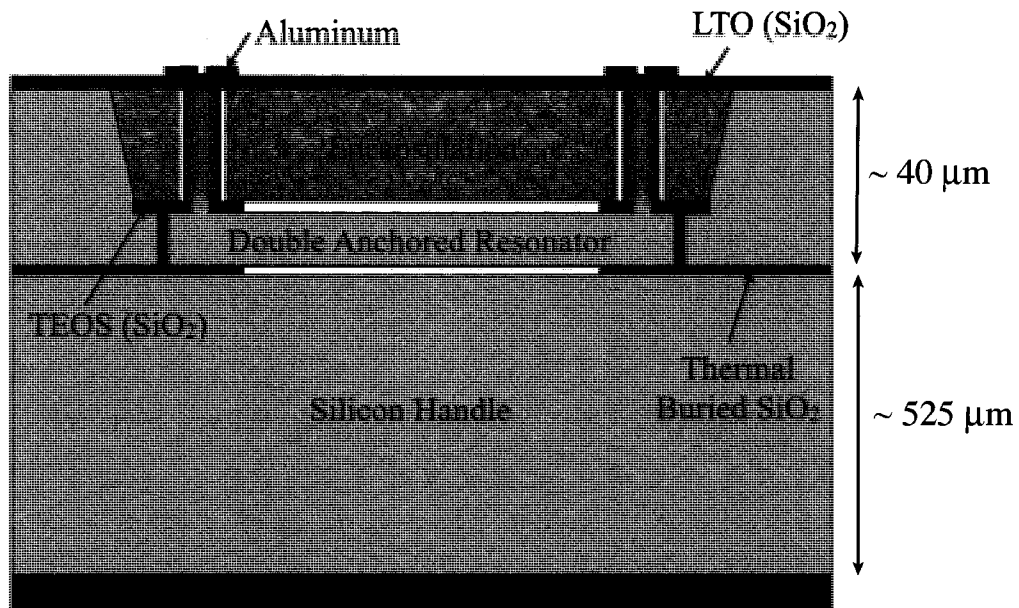


Figure 6.2: Schematic of cross section of die with double anchored resonator.

Figure 6.1. An approximated cross-section drawing of the die with the double anchored resonator is shown in Figure 6.2. Figure 6.3 shows the frequency-temperature behavior of this die compared to an identical die that has been released from the package such that it is “floating” and does not have packaging induced stresses. The linear temperature coefficient of frequency is approximately 6 times larger than the $-31 \text{ ppm}/^\circ\text{C}$ that is typical for an unstressed silicon resonator.

To analyze the effect of the package stress, a radial-symmetry linear finite element model in the COMSOL program was used to simulate the effects of the epoxy, copper paddle and IC plastic. Figure 6.4 shows the stress distribution through the package due to a 25°C increase in temperature. Using this model the strain of the resonator cavity can be determined. The copper, which has a higher coefficient of thermal expansion than silicon, induces tensile stresses in the die at the interface with the epoxy with increasing temperature. The epoxy transmits the strain of the copper paddle to the bottom of the resonator die. The resultant moment created by the forces at the interface generates a compressive stress at the top of the die where the

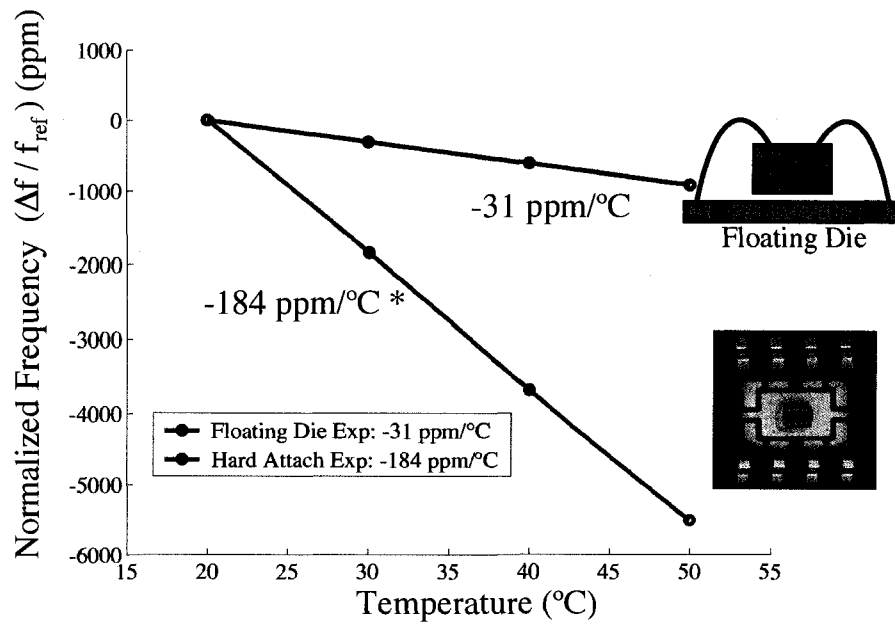


Figure 6.3: Frequency-temperature behavior of a double-anchored DETF attached to a copper lead frame using epoxy compared with an identical device die which is floating.

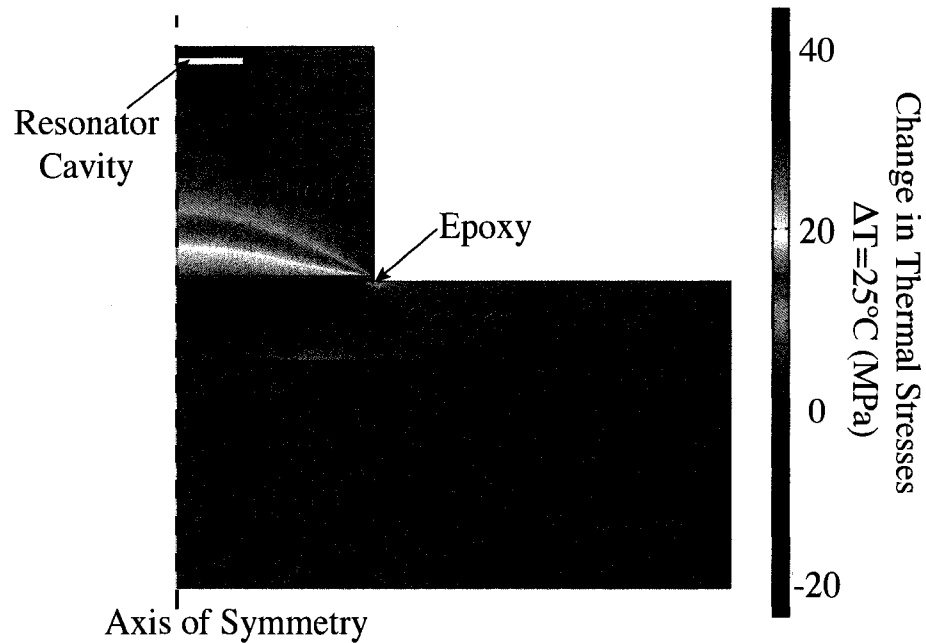


Figure 6.4: Axi-symmetric 2D finite element model of resonator die epoxied to a copper leadframe of a plastic IC package.

resonator is located. This is due to the cube-like geometry of the resonator die such that the neutral axis is found to be approximately half way through the die. Since the bottom of the die is in tension, the top of the die, where the resonator is fabricated, is in compression. It is this compressive stress that results in a decrease in frequency, in addition to the decrease in the Young's Modulus of silicon.

When strain at the edges of the resonator cavity is applied to a finite element model of the DETF resonator, the resulting stress is determined. Lastly, the eigenfrequency solver is used to obtain the frequency of the resonator under this strain condition. Figure 6.5 shows the finite element simulation matches well to the measurement results.

Since we have seen that it is possible to use thermal stresses to increase the sensitivity to temperature, it is also possible to reduce the sensitivity to temperature. In the following section, package level stresses will be designed such that the temperature

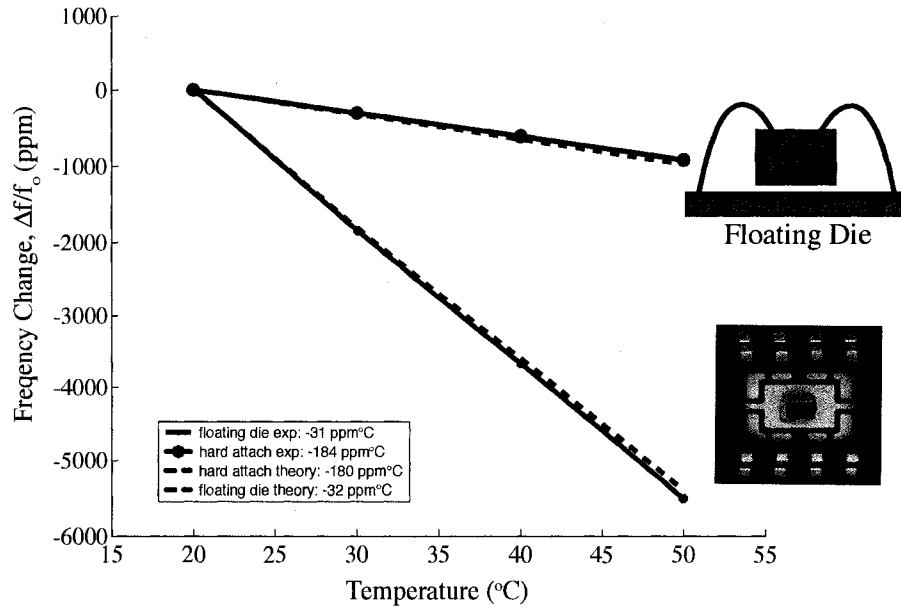


Figure 6.5: Frequency-temperature behavior of packaged double-anchored DETF. Finite element results compared to experiment.

coefficient of frequency is minimized.

6.2 Optimization of Thin Film Encapsulation

The determination of thermal stresses / strains that will yield “zero-TCf” resonators can be found by using the equations 1.21 through 1.23 derived in Chapter 1. Assuming that electrostatic effects are negligible ($r_e \ll 1$) and that the initial axial loads are small compared to the buckling load ($P \ll P_b \rightarrow r_b \ll 1$), the linear temperature coefficient of frequency becomes:

$$TCf_1 = \frac{(\alpha + TCE_1) + \left(\frac{1}{P_b} \frac{\partial P}{\partial T}\right)}{2(1 + r_b)} \quad (6.1)$$

Equation 6.1 can be set to zero and solved for the change in the axial load with temperature required to yield “zero-TCf” resonators:

$$\frac{\partial P}{\partial T} = -P_b(TCE_{1,S_i} + \alpha_{S_i}) \quad (6.2)$$

Substituting the Euler buckling load for a clamped-clamped beam into equation 6.2 and rewriting the equation in terms of axial strain, the axial strain necessary to achieve a “zero-TCF” resonator is:

$$\frac{\partial \varepsilon}{\partial T} = -\frac{\pi^2}{3} \left(\frac{w}{L} \right)^2 (TCE_{1,Si} + \alpha_{Si}) \quad (6.3)$$

From equation 6.3, the ideal thermal strain depends not only on the temperature dependent properties of silicon but also on the geometry of the resonator. In particular, resonators with larger length to width ratios will require smaller changes in strain to cancel the temperature changes of the material properties. Furthermore, since the temperature coefficient of Young’s Modulus of silicon is a negative quantity, the change in strain with temperature must be a positive quantity (i.e. a tensile change with temperature must be induced).

One of the ways to induce tensile stress in the resonator is to include an additional material layer in the die which has a larger coefficient of thermal expansion than silicon. This layer must also be at the top of the die near the resonator such that as the temperature is increased the expansion of this layer induces a tensile strain in the resonator (Figure 6.6). For a given material, whose material properties are known, it is possible to approach this problem in two ways: (1) determine the ideal thickness of the compensating layer such that the resonator with a particular dimension is compensated, or (2) for a given thickness of the compensating layer determine the resonator geometry such that the strain induced by the compensating layer perfectly compensates the resonator.

There are advantages and disadvantages to both approaches. One disadvantage of the first approach is that the thickness necessary to perfectly compensate might be difficult to achieve if the film must be very thick. Furthermore, since the method uses a mismatch in the coefficient of thermal expansion, thick layers might induce unwanted wafer level thermal stresses that result in wafer bending. In the second approach, a resonator could be designed to be compensated with a much thinner layer. However, this constrains the design of the resonator such that only a resonator with a particular width to length ratio, and thus a particular frequency, is temperature

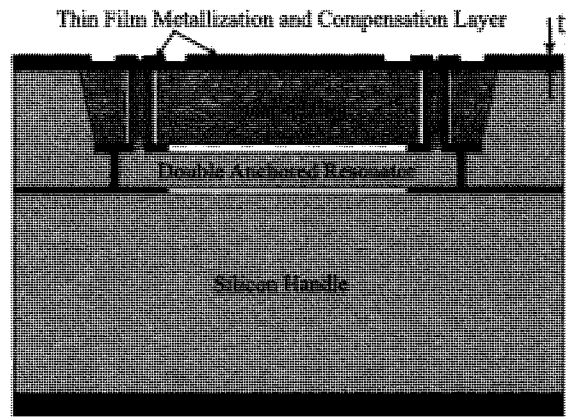


Figure 6.6: Schematic of cross section of die with double anchored resonator.

compensated.

Regardless of which approach is taken, the first step toward compensating using thermal stresses is to understand how thermal stresses induced in the film are transferred to the resonator. Precise determination of this stress transfer can be achieved using a finite element software. However, to build intuition, a simple analytical model will be developed.

Several assumptions are made in creating the simple model. The first is that the materials in the die, excluding the compensation layer, have similar coefficients of thermal expansion such that the stresses induced by the die materials are much smaller than then the stresses induced by the compensation layer. This assumption is valid since the majority of the die is silicon with only a couple of very thin layers of silicon dioxide. Second, the stresses induced in the die are comparable to the wafer level stresses prior to dicing. This assumption will allow the use of simple wafer-bending formulations. Third, the thickness of the compensation layer is much smaller than the thickness of the substrate. This will allow simplified expressions using the thin film on a substrate approximation. Fourth, since the resonator is located near the encapsulation, and thus near the compensation layer, the strains in the resonator are approximately equal to the strains in the substrate at the interface of the encapsulation and compensation layer. Lastly, all of the preceding assumptions assume that the final die is measured in a “floating” position such that IC packaging

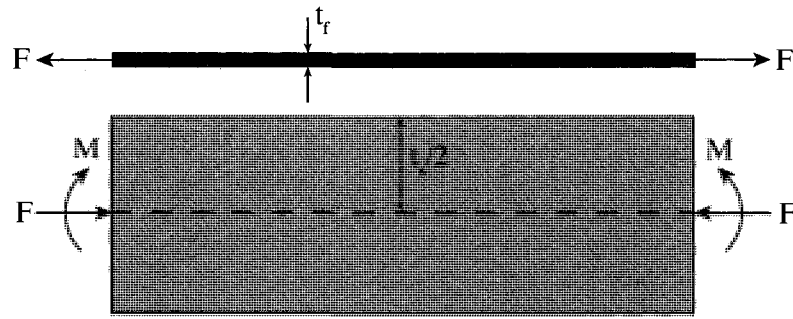


Figure 6.7: Thin film and substrate force / moment balance.

stress effects are removed.

By considering the compensation layer as a thin film covering the substrate, the stresses in the compensation layer are found by using strain compatibility at the interface of the film and the substrate:

$$\varepsilon_f^{elastic} + \varepsilon_f^{thermal} = \varepsilon_{s,interface}^{elastic} + \varepsilon_s^{thermal} \quad (6.4)$$

In equation 6.4, the subscripts “f” and “s” correspond to the compensating film and the substrate, respectively. To determine the elastic strains in the film and the substrate, consider the forces and moments developed at the neutral axis of the substrate due to stresses in the thin film (Figure 6.7).

Neglecting the out of plane dimension, the equivalent force in a thin film of thickness t_f due to a stress σ_f is:

$$F = \sigma_f t_f \quad (6.5)$$

This force will induce an equal but opposite force on the neutral axis of the substrate and a moment of magnitude:

$$M = \sigma_f t_f \frac{t_s}{2} \quad (6.6)$$

The total stress in the substrate at a distance y from the neutral axis is found by summing the stresses developed due to the equivalent force and moment:

$$\sigma_s = \sigma_F + \sigma_M \quad (6.7)$$

$$\sigma_s = -\frac{\sigma_f t_f}{t_s} \left(1 + \frac{6y}{t_s}\right) \quad (6.8)$$

The strain in the substrate near the interface with the thin film is found by substituting $y = t_s/2$ into equation 6.8 and dividing by the biaxial modulus of the substrate.

$$\varepsilon_{s,interface}^{elastic} = \frac{\sigma_{s,interface}}{B_s} = -\frac{4\sigma_f t_f}{B_s t_s} \quad (6.9)$$

Substituting equation 6.9 into the compatibility equation and solving for the stress in the thin film:

$$\sigma_f = \frac{(\alpha_s - \alpha_f)\Delta T}{\frac{1}{B_f} + \frac{1}{B_s} \frac{4t_f}{t_s}} \quad (6.10)$$

In equation 6.10, B is the biaxial modulus, ΔT is the change in temperature, t_f is the thickness of the compensating layer, and t_s includes all of the layers in the die except the compensating layer. For isotropic films the biaxial modulus is given by the Young's Modulus (E) and the Poisson ratio (ν):

$$B_{isotropic} = \frac{E}{1 - \nu} \quad (6.11)$$

For anisotropic materials with cubic symmetry, such as single-crystal silicon, the biaxial modulus is given by a combination of the stiffness coefficients [32]:

$$B_{cubic} = C_{11} + C_{12} - 2\frac{C_{12}^2}{C_{11}} \quad (6.12)$$

Using the assumptions mentioned, the strain in the resonator is approximately equal to the strain in the substrate near the film interface. The strain in the resonator is found by substituting equation 6.10 into equation 6.9. Taking the temperature derivative of the resulting equation results in an approximate change in strain in the resonator with temperature:

$$\frac{\partial \varepsilon_{s,res}}{\partial T} = -\frac{4t_f (\alpha_s - \alpha_f)}{B_s t_s \frac{1}{B_f} + \frac{1}{B_s} \frac{4t_f}{t_s}} \quad (6.13)$$

When equation 6.13 is set to equal the ideal temperature dependent strain necessary to temperature compensate (equation 6.3), the equation can be solved for the desired unknown. For example, if the dimensions of the resonator are set and the material properties of the compensating layer are known, the equation can be solved for the thickness of the compensating layer. However, if the compensating layer is fixed to a known thickness, the width to length ratio can be determined for resonator design. In the following sections, both approaches will be discussed.

6.2.1 Thin Film Thickness Compensation

Solving for the film thickness to achieve ideal compensation:

$$t_f^* = \frac{t_s B_s}{4 B_f} \left[\frac{(TCE_{1,Si} + \alpha_{Si})}{\frac{3}{\pi^2} \left(\frac{L}{w}\right)^2 (\alpha_s - \alpha_f) - (TCE_{1,Si} + \alpha_{Si})} \right] \quad (6.14)$$

To reduce the thickness necessary to compensate it is advantageous to use films with high biaxial moduli and large coefficients of thermal expansion compared to silicon. Figure 6.8 shows the ideal thickness necessary to compensate a resonator with a length to width ratio of $220/8 = 27.5$ using a wide range of biaxial moduli and coefficients of thermal expansion. Also shown are markers for the location of several common materials that could be used. One of the most common materials is aluminum which could be deposited as both a metalization layer and compensation layer in the last step of processing.

The approximate solution indicates that $3 \mu\text{m}$ of aluminum will be necessary to compensate. Typical metalization layers are less than $1 \mu\text{m}$. A 2D axi-symmetric finite element analysis was performed with a thin film compensation layer on the top surface of the resonator, but without the package shown in Figure 6.4. The ideal thickness for an aluminum film was determined to be approximately $5 \mu\text{m}$. Although the simplified model can be used as a good rule of thumb, it under-predicts the

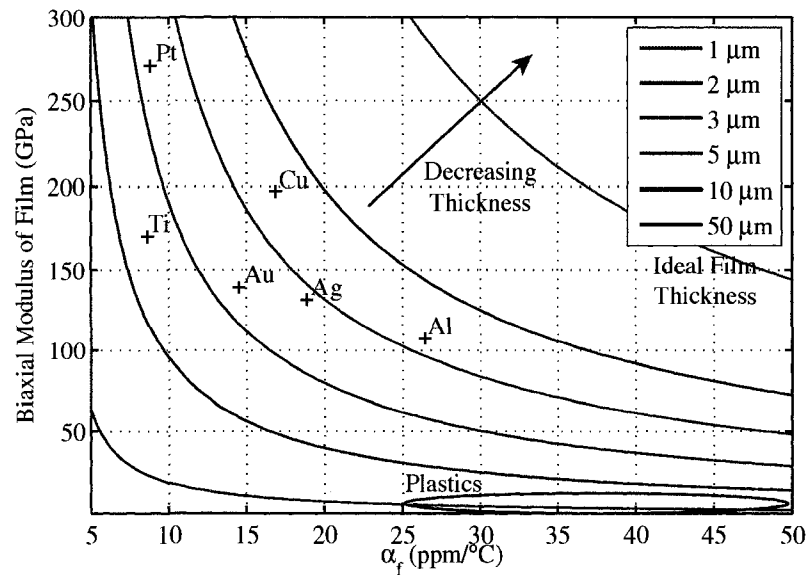


Figure 6.8: Ideal thickness of compensation layer versus biaxial modulus and coefficient of thermal expansion.

stiffness of the resonator die and thus the ideal thickness of the compensation layer necessary to compensate.

To verify this compensation methodology, DETF resonators with a length to width ratio of 27.5 were fabricated such that the majority of the die was covered with aluminum during the metal trace definition (see Chapter 3). Wafers were fabricated with this aluminum compensation layer varying from 2 μm to 7 μm in thickness. After dicing, the die was wirebonded and the epoxy under the resonator was then removed such that the die was “floating”. Figure 6.9 shows the measured temperature coefficient of frequency at 25°C for die with varying aluminum layer compensation thickness.

Unfortunately, low yield resulted in few functioning devices. A trend is established, showing that thicker compensation layers result in more positive temperature coefficients of frequency. For a 7.5 μm film thickness a positive temperature coefficient is observed, verifying this methodology. The deposition of thick films is undesirable due to the difficulty of controlling the deposition and requiring multiple wafers with

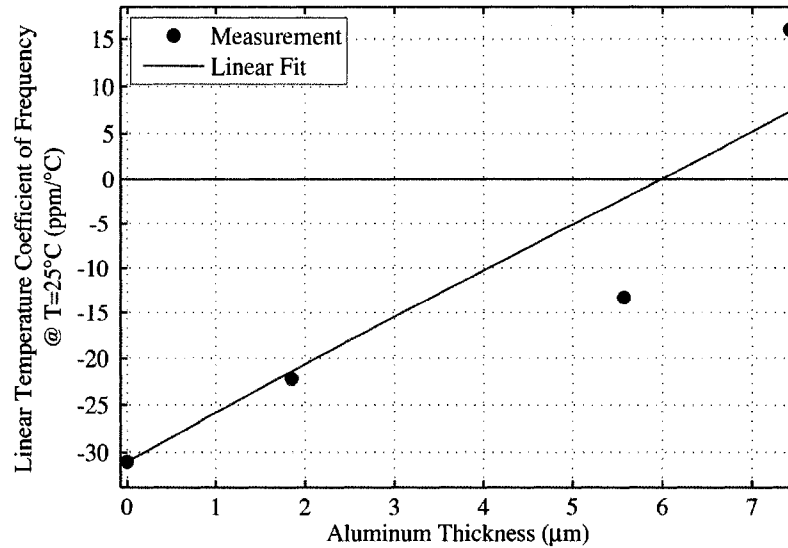


Figure 6.9: Measured linear temperature coefficient of frequency of a double-anchored resonator with various thickness aluminum thin film compensation layers.

different metal layer thicknesses. These drawbacks are reduced by following a different approach described in the next section.

6.2.2 Resonator Design for Thin Film Compensation

The ideal length to width ratio for a resonator to be compensated by a thin film with known material properties and thickness can be simply derived by rewriting equation 6.14:

$$\left(\frac{L}{w}\right)^* = \sqrt{\frac{\pi^2 (TCE_{1,Si} + \alpha_{Si})}{3 (\alpha_s - \alpha_f)} \left(1 + \frac{1}{4} \frac{t_s B_s}{t_f B_f}\right)} \quad (6.15)$$

Figure 6.10 shows the ideal length to width ratios necessary to achieve ideally compensated resonators using a compensation film thickness of 1 μm. For example, a 1 μm film of aluminum can be used to compensate a double anchored DETF with a length to width ratio of approximately 45. As before, it is expected that equation 6.15 will under predict the length to width ratio since the bending stiffness of the

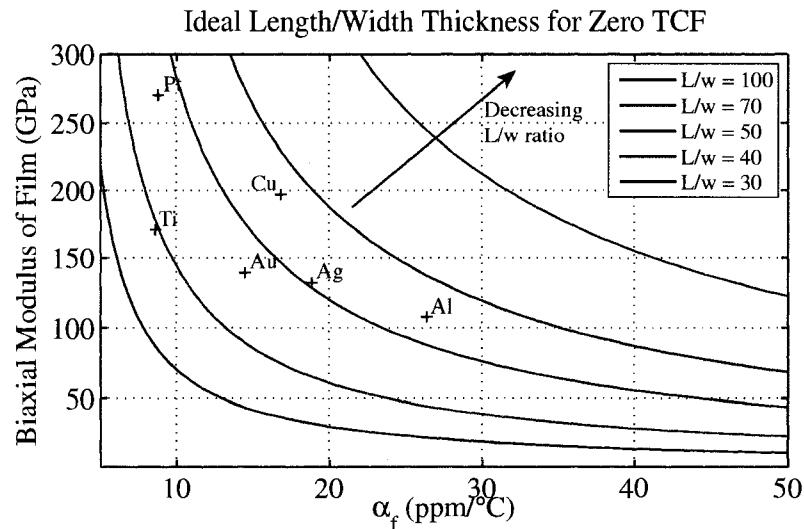


Figure 6.10: Ideal length to width ratios for compensation using a 1 μm thin film of various biaxial moduli and coefficients of thermal expansion.

resonator die will be higher than the bending stiffness of a wafer.

DETF resonators with a beam length of 300 μm and widths of 4.5 μm to 7 μm were fabricated on the same wafer. A 1 μm aluminum layer was sputtered for metallization as well as compensation. Figure 6.11 shows the layout of the metal layer on top of the die. The majority of the die is covered with aluminum. However, the layer is not continuous since bondpads are necessary to actuate the resonator under the encapsulation.

After dicing, the die was wirebonded and the epoxy under the resonator was then removed such that the die was “floating”. Figure 6.12 shows the measured frequency-temperature behavior of double anchored DETFs with varying length, L , to width, w , ratios. The linear temperature coefficient of frequency is extracted at 25 °C, and is plotted in Figure 6.13 compared to the theoretical prediction using the analytical model above.

For a L/w ratio of approximately 64, ideal compensation was achieved with a frequency variation of approximately 200 ppm over the 100 °C temperature range.

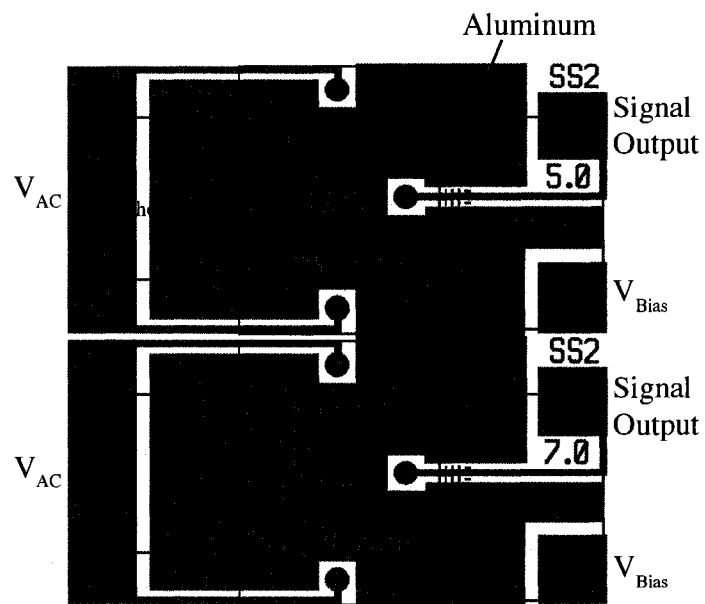


Figure 6.11: Layout of aluminum compensation layer on top of die with two double anchored DETFs. Image of double anchored DETF definition is superimposed on top of aluminum layout. Red circles indicate location of electrical interconnect between the aluminum traces and the underlying structure.

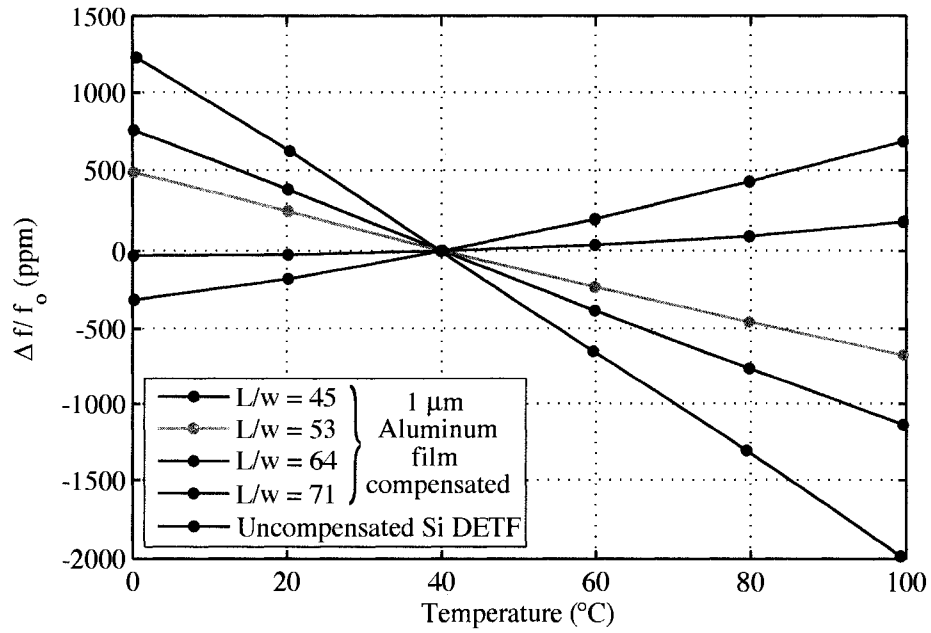


Figure 6.12: Measured frequency change versus temperature for DETFs with various L/w ratios. A L/w ratio of 64 achieves 200 ppm frequency variation.

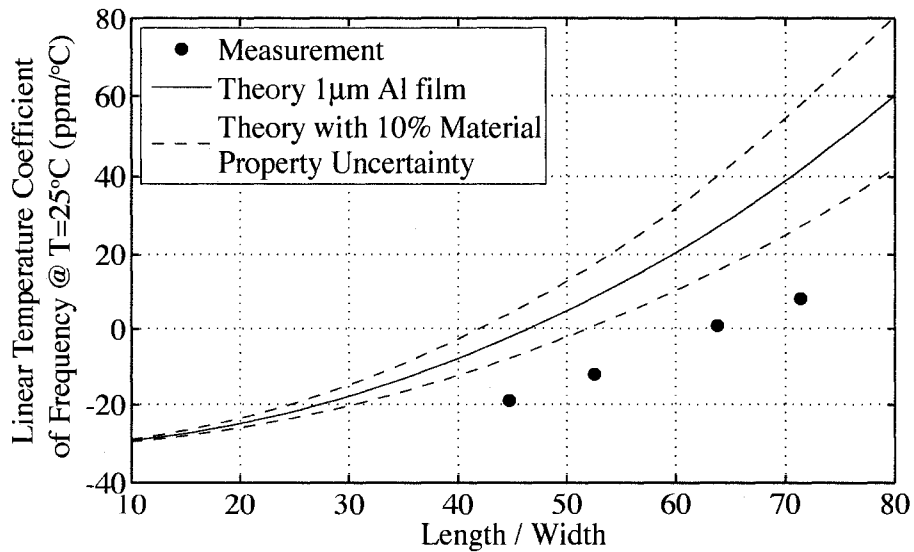


Figure 6.13: The temperature coefficient of frequency at 25 °C extracted from measurement in Figure 6.12 is compared to the simple analytical model

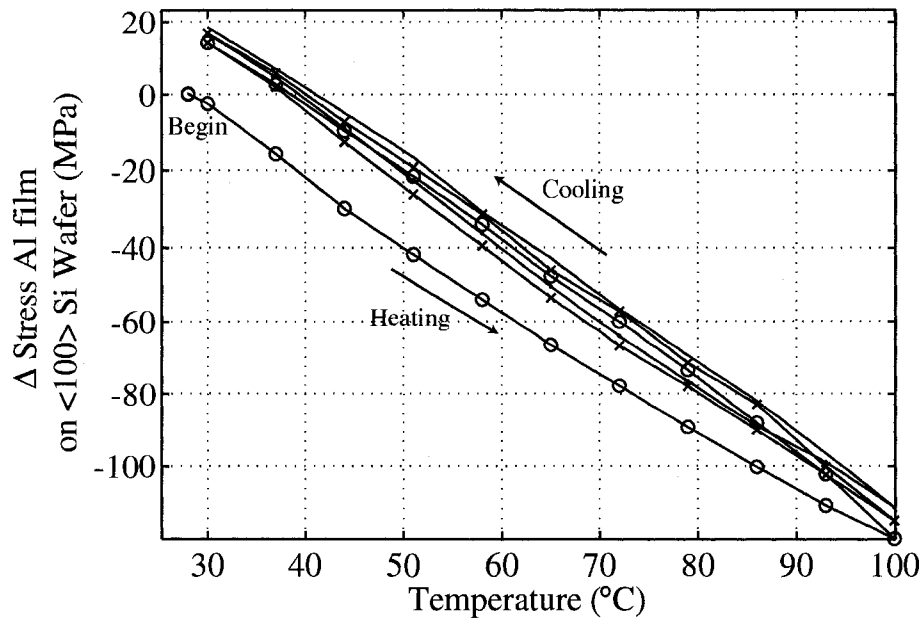


Figure 6.14: Low temperature cycling of a $1.1 \mu\text{m}$ sputtered aluminum film on a $\langle 100 \rangle$ silicon wafer. Measurement obtained using laser curvature system.

Although this is a large reduction compared to uncompensated silicon resonators, there are two major drawbacks to this approach. As discussed previously, stress compensation can be difficult, if not impossible to achieve, due to the difficulty in completely isolating the resonator to only the desired stress mechanism. Furthermore, this methodology relies on both the resonator as well as the stress inducing mechanism to be stable over time and temperature.

Stress evolution in thin films over thermal cycling has been studied in depth ([26, 70, 85]). In particular, the thermo-mechanical properties of aluminum have been of great interest in the semiconductor industry owing to its use as an interconnect material [30]. In this work, the effect of temperature cycling on the frequency of the resonator must be characterized since stress evolution leads to frequency instability and hysteresis.

Thermal hysteresis in aluminum thin films is due to transitions from elastic to plastic regimes during thermal cycling. Characteristic curves for aluminum are well

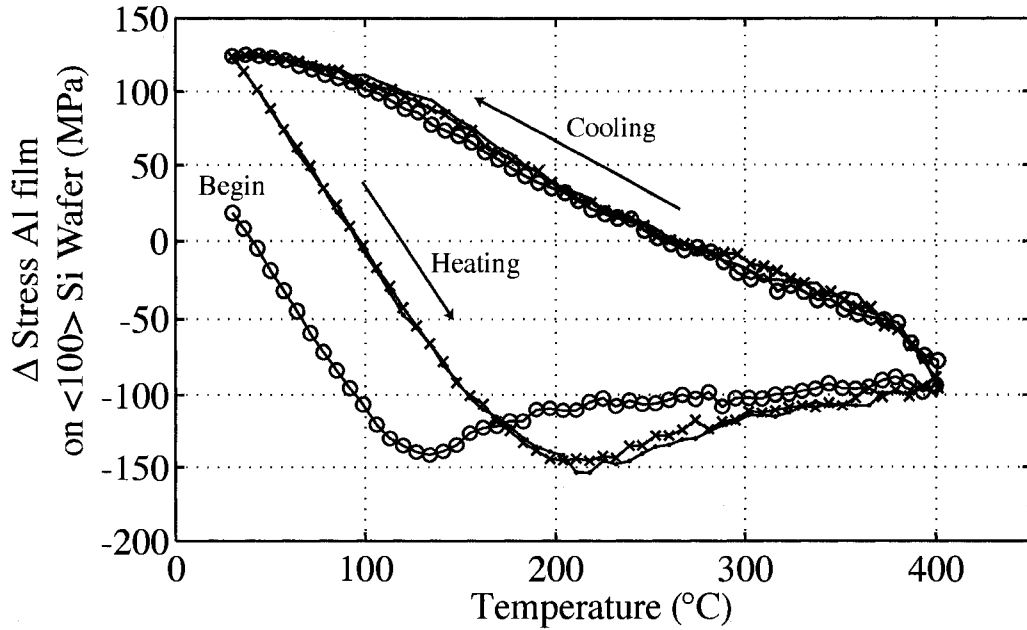


Figure 6.15: High temperature cycling of a $1.1 \mu\text{m}$ sputtered aluminum film on a $\langle 100 \rangle$ silicon wafer. Measurement obtained using laser curvature system.

established [70] and are reproduced here with a simple wafer curvature experiment. A $1.1 \mu\text{m}$ aluminum film was sputtered onto a $552 \mu\text{m}$ thick $\langle 100 \rangle$ $4''$ silicon wafer at 40°C in a Gryphon DC magnetron sputterer. The film was not annealed after sputtering. A Tencor FLEX laser system was used to measure the curvature of the wafer during thermal cycling. The change in stress in the thin film can be extracted using Stoney's Formula [32]:

$$\Delta\sigma_f = B_s \frac{t_s^2}{6t_f} \Delta\kappa \quad (6.16)$$

In equation 6.16, σ_f is the stress in the thin film, B_s is the biaxial modulus of the substrate, t_s is the thickness of the substrate, t_f is the thickness of the film, and κ is the measured curvature.

The thin film was first cycled three times over a 30°C to 100°C temperature range (Figure 6.14). There is a change between the first cycle and the subsequent cycles. Noise in the curvature measurement makes it difficult to clearly distinguish

repeatable hysteresis. The thin film was then cycled three times over a 30 °C to 400 °C temperature range (Figure 6.15). The high temperature cycling shows a characteristic elastic-plastic thermal hysteresis [70]. In the first part of the heating cycle a linear decrease in stress is due to the mismatch in the coefficients of thermal expansion. Since silicon has a lower coefficient of thermal expansion than aluminum, the aluminum goes into compression as temperature is increased. A minimum is reached as the aluminum transitions from elastic to plastic regime during which grain boundaries in the film expand and the film recrystallizes. The stress levels off as the aluminum yields. When the substrate begins to cool, the film undergoes a shorter elastic deformation and on subsequent cooling plastically deforms.

To investigate the effect of thermal cycling at the resonator level and temperature range of interest, the resonator with the ideal ratio was cycled seven times over a 0 °C to 100 °C temperature range. Figure 6.16 shows the measured frequency hysteresis of the resonator. Since frequency change is a measure of strain change in the resonator due to strain changes in the thin film, it is possible to extract the strain and thus stress changes in the thin film.

The strain in the resonator is first found by rewriting the effect of axial loads on the frequency of the resonator from equations 1.21 and 1.23:

$$f_{measured}(\varepsilon_{res}, T) = f_n(T) \sqrt{1 + \frac{3}{\pi^2} \left(\frac{L}{w}\right)^2 \Delta\varepsilon_{res}} \quad (6.17)$$

In equation 6.17, ε_{res} is the strain in the resonator and $f_n(T)$ is the change in frequency due to only temperature: $f_n(T) = f_o(1 + TCf_{1,Si}\Delta T)$. Solving for the change in strain of the resonator:

$$\Delta\varepsilon_{res} = \frac{3}{\pi^2} \left(\frac{w}{L}\right)^2 \left(\left(\frac{f_{measured}}{f_o(1 + TCf_{1,Si}\Delta T)} \right)^2 - 1 \right) \quad (6.18)$$

In equation 6.18, f_o is the frequency at 40 °C, the temperature at which the film is sputtered. The linear temperature coefficient of frequency of silicon resonators, $TCf_{1,Si}$, has been previously measured to be approximately -31.4 ppm/°C. Equation

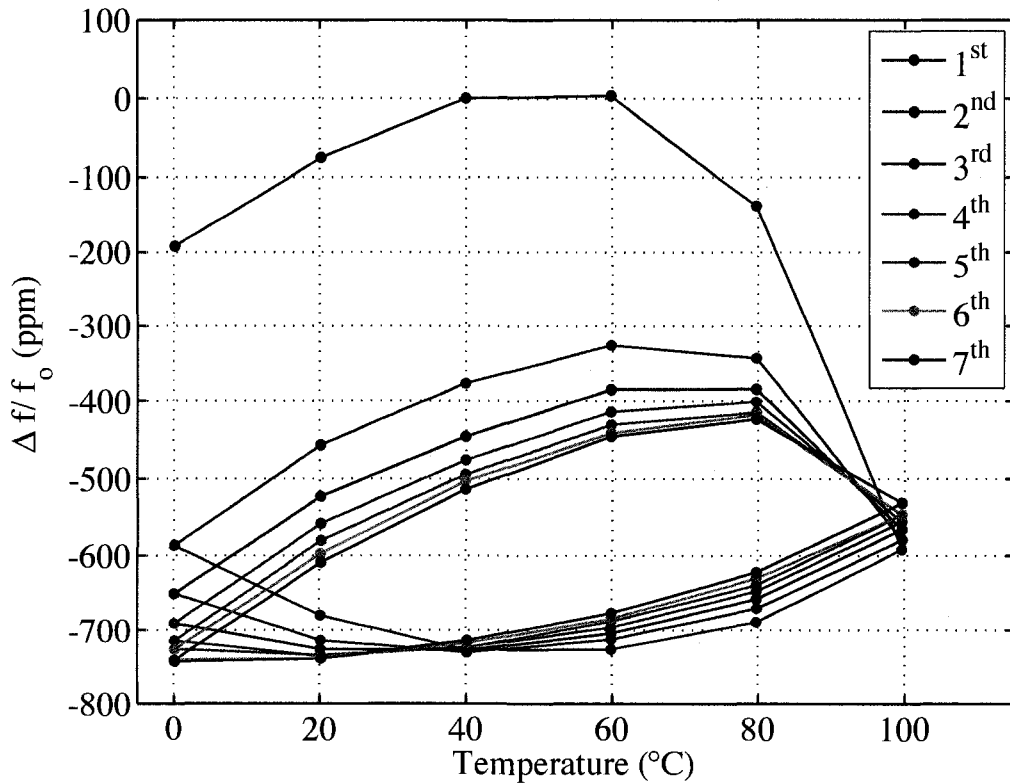


Figure 6.16: Thermal cycling of the resonator die indicates severe thermal hysteresis in the operating temperature range.

6.9 can be used to transform the strain in the resonator to stresses in the thin film. Fig. 6.17 shows the extracted change in stress in the compensating aluminum film.

Unlike the curvature measurements, the extracted change in stress from the frequency hysteresis is a clear indication of evolution of stresses at low temperatures. A comparison of the change in stress obtained from the frequency hysteresis, Fig. 6.17, to the change in stress obtained using the laser curvature method indicates that both methods are consistent in determining the relative change in stress. The change in determined from the curvature measurement system is approximately $-2 \text{ MPa}/^\circ\text{C}$. The change in stress determined from the frequency measurement is approximately $-1.4 \text{ MPa}/^\circ\text{C}$.

The hysteresis in the aluminum film makes its use in thermal stress compensation

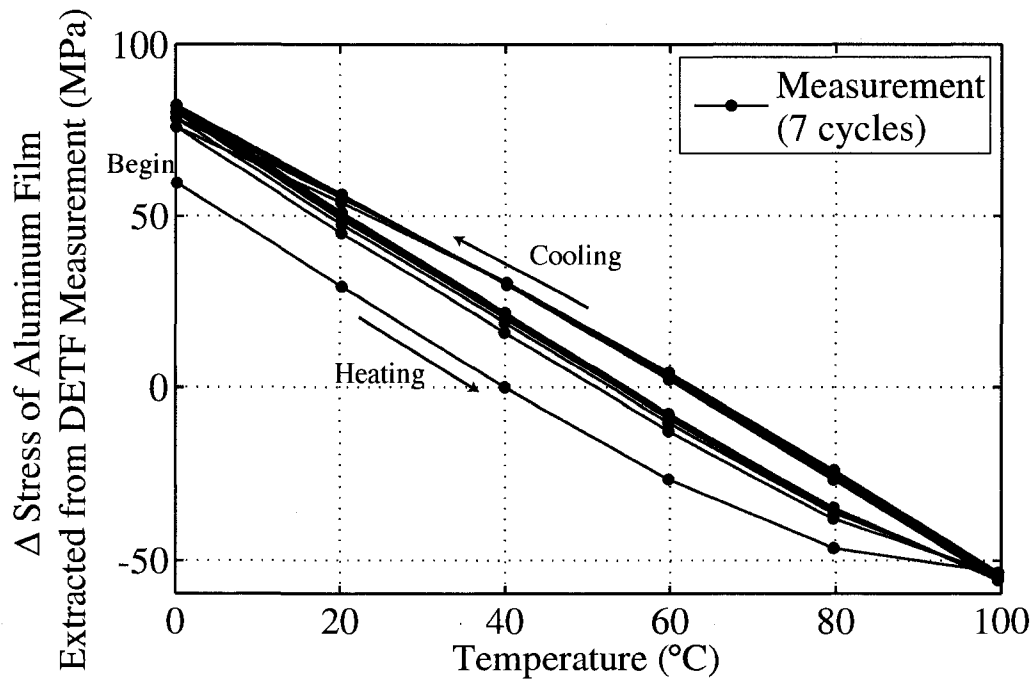


Figure 6.17: Extracted change in stress of aluminum thin film from frequency hysteresis of the compensated double anchored DETF.

impractical. However, the extraction of thin film behavior through frequency measurements opens opportunities for studying other commonly used thin films. This methodology allows using the encapsulated resonator as a platform for material science research. Since the reliability of the resonator is decoupled from the film, the resonator becomes an exquisite sensor for stress changes in the layers to which its coupled.

6.3 Summary

In this chapter the use of thin film thermal stress compensation for silicon-only encapsulated resonators is demonstrated. By a slight modification in the layout of the metallization layer - the last layer in the “epi-seal” process - the metal thin film can induce thermal stresses in double-anchored tuning forks to cancel the effects of temperature dependent material properties. Simple models are developed as a rule of thumb in

determining the ideal dimensions of the thin film or resonator to ideally compensate. Two approaches are taken for compensation. In one approach the dimensions of the resonator are kept constant and the thickness of an aluminum thin film on top of the encapsulation is varied. In the second approach, a 1 μm aluminum film is used to modify the frequency-temperature behavior of various double anchor double-ended tuning fork resonators. A resonator with a compensated frequency-temperature behavior of less than 200 ppm over a 100 °C temperature span is demonstrated using the second approach. However, thermal hysteresis in the frequency behavior is observed. This undesirable frequency behavior is due to stress evolution in the aluminum film. The stress in the film is extracted from the frequency behavior and is shown to be consistent with stress evolution of aluminum films determined by a wafer curvature measurement.

Due to the hysteretic frequency behavior, this methodology is not viable for a commercial device. However, the sensitivity of the silicon resonator to the stress evolution in thin films on top of the encapsulation provides an opportunity for material science research of thin films. The encapsulated silicon resonator, which has been thoroughly characterized, is a stable platform which can be used to measure the mechanical properties of thin films.

6.4 Acknowledgements

The double-anchor tuning fork resonators of varying length-width ratios were fabricated by Gary Yama. Violet Qu helped with the experimental setup of the floating die. Dr. Nix provided the Tencor FLEX laser system for curvature measurements.

Chapter 7

Conclusion, future directions, and impact

The commercialization of silicon resonators for frequency references is complicated by the high temperature sensitivity of frequency of silicon resonators. To correct for this sensitivity, active temperature compensation schemes require additional electronics devoted to temperature compensation, are limited by the thermometry used, and consume additional power. With the currently available thermometry, the temperature sensitivity of silicon resonators impedes the ability of active compensation to achieve the frequency stability levels that oven controlled quartz crystal oscillators (OCXO's) are currently providing.

Passive compensation methods aim to reduce the temperature sensitivity of resonators without the use of electronics. Previously, the passive compensation techniques employed thermal stresses in flexural mode resonators to compensate. However the use of thermal stresses is limited to multi-anchored devices and tends to couple undesirable stresses, such as from packaging, into the frequency response of the resonator.

A passive compensation scheme that does not use thermal stresses and can be used in a wide variety of resonator designs has been demonstrated. In this work, silicon dioxide, which has a positive temperature coefficient of Young's Modulus, is used to create composite silicon - silicon dioxide resonators with frequency - temperature

stability comparable to quartz crystal resonators. These silicon based resonators have a 30-fold reduction in their temperature sensitivity compared to silicon resonators over a $-40\text{ }^{\circ}\text{C}$ to $125\text{ }^{\circ}\text{C}$ temperature range. The devices are packaged in a CMOS-compatible, hermetic, wafer level encapsulation process.

In this dissertation, a theoretical analysis of the frequency and temperature coefficient of frequency (TCf) for composite resonators is demonstrated. It is shown that the temperature coefficient of frequency of the composite is determined by a ratio which is a function of the mass and frequency of the silicon and silicon-dioxide portion of the resonator. However, the "ideal" ratio, at which the linear temperature coefficient of frequency is cancelled, thus yielding "zero-TCf" resonators, is set only by the temperature dependence of the material properties of silicon and silicon dioxide. Furthermore, it is found that the construction which minimizes the use of silicon dioxide to compensate is a flexural mode resonator with a uniform coating of silicon dioxide around the vibrating beam.

To demonstrate the viability of this design, the resonators were fabricated at the Stanford Nanofabrication facility using a modified MEMS-first "epi-seal" packaging processes. The "epi-seal" process was previously demonstrated to yield hermetically sealed silicon resonators with impeccable long-term stability characteristics. The composite resonator was formed by thermally oxidizing the silicon resonator after the resonator was released, thus forming a symmetric structure. The modified process demonstrates that composite resonators can be hermetically encapsulated in an "epi-seal" process with very high yields.

The frequency temperature behavior of composite resonators was tested over a large temperature range. The resonators with the ideal silicon - silicon dioxide construction were found to have a zero linear temperature coefficient of frequency and a resulting quadratic frequency-temperature behavior. The quadratic temperature coefficient of frequency was found to be dominated by the quadratic temperature coefficient of Young's Modulus of silicon. Due to the uncertainty in the dimensions of the encapsulated resonator, the quadratic temperature coefficient of Young's Modulus of silicon dioxide could not be extracted. The linear temperature coefficient of the Young's Modulus of silicon dioxide was extracted to be $179.4\text{ ppm}/^{\circ}\text{C} \pm 5.4\text{ ppm}/^{\circ}\text{C}$.

Slight modification of the composition of silicon to silicon dioxide resulted in an adjustment of the turnover temperature, the temperature at which the linear temperature coefficient of frequency is cancelled. Several devices exhibited a turnover temperature at an elevated temperature which would allow for integration with an active oven temperature-control scheme. However, due to process variations, the turnover temperature of identically designed devices was found to vary across the wafer. The large degree of variation, ± 25 °C, is undesirable, since a consistent turnover temperature is necessary for oven controlled compensation techniques. If testing over temperature is not performed to obtain the turnover temperature, the thermometry for active oven control would require a temperature resolution of better than 0.1 °C.

The long-term stability of composite resonators was tested at constant temperature over a period of 200 days. Although the majority of the devices exhibited frequency stability better than 2 ppm, some devices exhibited exponentially decaying frequency on the order of tens of ppm. This transient behavior was attributed to the presence of mobile charges in the silicon dioxide. By switching the polarity of the bias voltage to the resonators, it was determined that both fixed and mobile charges are present. However, it is the mobile charges that are undesirable and threaten the viability of this architecture for commercialization. The search for the root-cause mechanisms for the presence of mobile charges is an ongoing effort ([6]).

7.1 Future Directions

The composite silicon-silicon dioxide devices provide a new starting point in the temperature sensitivity of silicon-based resonators. In this section, the pathway for new designs, processes, and improved frequency stability is outlined.

7.1.1 Composite Design

The use of finite element analysis can greatly enhance the design of ideally compensated resonators. Although simple beam and ring geometries are straight forward to

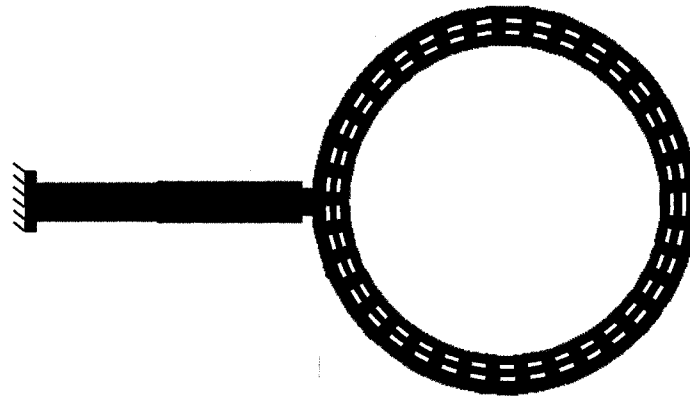


Figure 7.1: Extensional ring resonator with additional slots to reduce thickness of SiO_2 necessary to ideally compensate

analytically analyze, the incorporation of slots into the vibrating structure can reduce the amount of silicon dioxide necessary to compensate.

The use of slots can be particularly useful in extensional mode designs (Figure 7.1). In this dissertation, an extensional mode ring resonator was demonstrated. However, a $0.35 \mu\text{m}$ thermal silicon dioxide coating was not sufficient to achieve ideal compensation. Introduction of slots into the design would increase the ratio of silicon dioxide to silicon through the cross-section of the geometry. The design of slots is made complicated by a radially varying effective Young's Modulus. Analysis of the placement and number of slots would require the use of finite element techniques. Furthermore, Candler et al. [21] demonstrated the use of slots in silicon resonators as a way of improving the quality factor of the flexural mode resonator by reducing losses due to thermoelastic dissipation. Utilizing these results, a design that maximizes quality factor as well as reduces the thickness of oxidation for temperature compensation would be advantageous.

The composite structure developed in this dissertation had clearly separated areas of silicon dioxide and silicon. The proportion of each material was designed such that the temperature dependent properties combined in a way which would result in a temperature-stable structure. However, one interesting extension of the composite principle is to envision a structure with a more homogeneous mixture of silicon

and silicon dioxide. Such a material, also known as a silicon-rich oxide, has been previously developed [80]. However, measurements of the temperature coefficients of Young's Modulus of such a material could not be found. The mechanism which results in a positive temperature coefficient of Young's Modulus of silicon dioxide is believed to be an intermediate-order effect (see Appendix C). This intermediate-order must be present in the homogeneous structure such that the overall temperature coefficient of Young's Modulus of the material is minimized. However, operation of this resonator could be inhibited since the conductivity of the material is reduced.

7.1.2 Composite Fabrication

There are several practical modifications to the fabrication of the "epi-seal" of composite resonators that should be incorporated into future processes.

The first is the use of hydrogen annealing to smooth sidewalls of the resonant structures after the definition deep reactive ion etch (DRIE). It was found that hydrogen smoothing after composite formation is blocked by the thermally grown silicon dioxide. The scalloped sidewalls due to the DRIE result in a non-uniform coating of silicon dioxide after oxidation. This non-uniformity is one of the leading causes of uncertainty in the dimensions of the final resonant structure.

Secondly, the overall thickness of the "epi-seal" encapsulation could be greatly reduced. The first polycrystalline silicon layer forming the encapsulation must be a thick $20\ \mu\text{m}$ layer to avoid buckling of this layer during thermal oxidation. However, the subsequent "epi-seal" layer could be made approximately $5\ \mu\text{m}$ to $10\ \mu\text{m}$. Kim et al. [51] showed that the primary pathway for diffusion of gases into and out of the resonator cavity occurs along the silicon dioxide path through the isolation trench. Therefore, a thin "epi-seal" layer should be sufficient for hermetically sealing the resonators.

The root-cause mechanism for the presence of mobile charges in the silicon dioxide dielectric has not been isolated and several suggestions are made to investigate their presence. The role of various annealing gases, such as forming gas (N_2 and H_2) anneal and pure hydrogen anneal (H_2), on the charge density in silicon dioxide should be

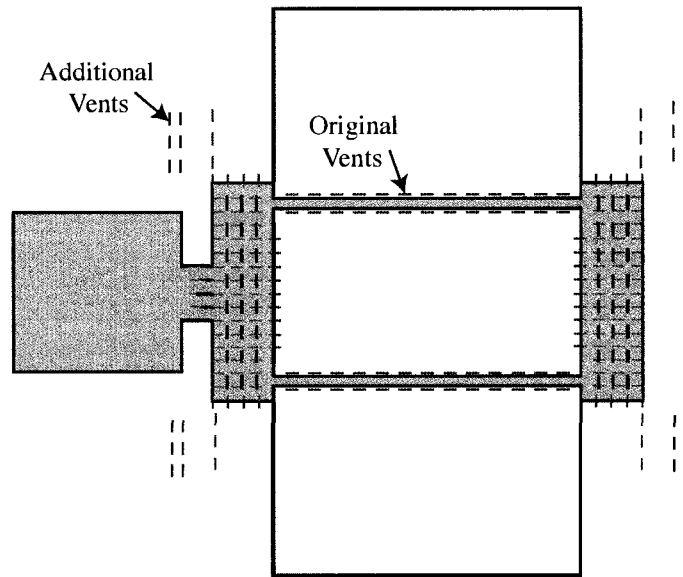


Figure 7.2: Layout of DETF definition superimposed with layout of original vent location and additional vent structures. The original vent structures provide access to the resonator for HF release and are then “epi-sealed”. The additional vents provide a new access path for thermal oxidation. After oxidation, plasma etching removes the thermal oxide on top of the wafer, but doesn’t damage the SiO_2 over the device since the original vents are sealed.

investigated. A modification of the “epi-seal” process to address the plasma damage caused by the reactive ion etching of the silicon dioxide on top of the wafer just before “epi-sealing” is suggested. The additional modification aims to seal the vents that are located just above the resonant structure before thermal oxidation and composite formation. To thermally oxidize the resonators, a different access path must be provided. This is accomplished by creating an additional set of vents located far away from the resonant structure and electrodes (Figure 7.2).

One way to realize this modification is to use the original vent placement to release the silicon resonators and then “epi-seal” the resonators following the original “epi-seal” process. After sealing, a mask containing the additional vents could be used to DRIE these vents far away from the resonator structure. An HF vapor release step is used to etch the TEOS silicon dioxide until access is gained into the resonator cavity.

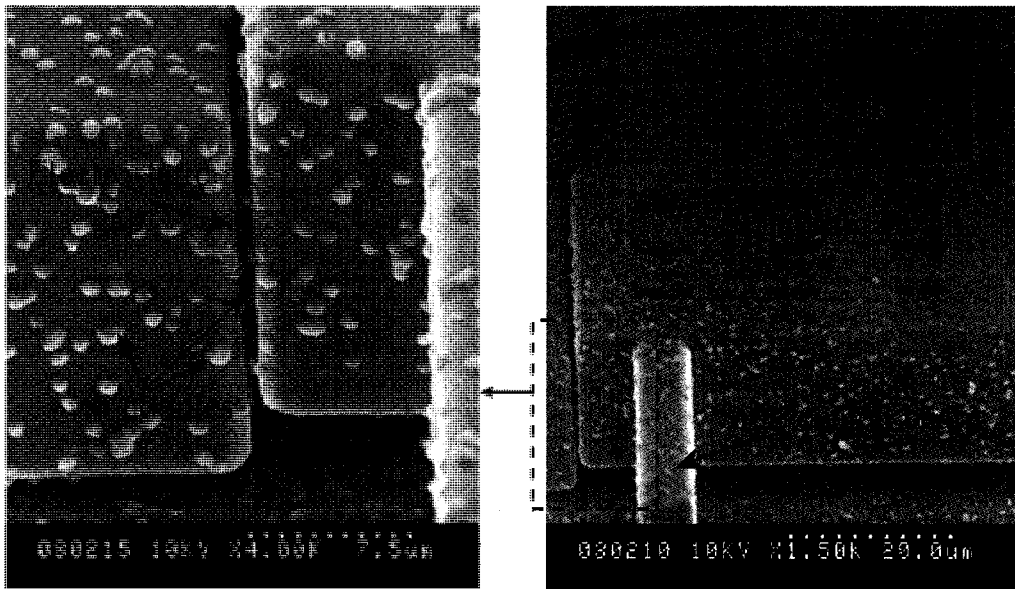


Figure 7.3: SEM of SiO₂ coated DETF resonator. During “epi-seal” silicon nodules grow on silicon dioxide surfaces due to poor selectivity. The silicon nodules in the electrostatic gap prevent the resonator from vibrating.

The resonators could then be thermally oxidized, forming the composite. A plasma etch of the top surface of the wafer would not affect the resonant structures since the vents over the resonator would have been previously sealed. After removing the top oxide, the additional vents could be sealed with an additional epitaxial silicon seal.

A slightly different approach would be to create a mask with both the original vent placement and the additional vents. However, the width of the additional vents could be doubled from 1 μm to 2 μm . After HF release of the silicon resonators, a carefully controlled “epi-seal” process is used to seal the original 1 μm vents, while leaving the additional vents still open. Thermal oxidation of the silicon resonators would then occur through the additional vents only. A plasma etch of the top surface would not attack the silicon dioxide on top of the resonator. After removing the top oxide, the additional vents could be sealed with an additional epitaxial silicon seal. However, control of the “epi-seal” process to just seal the original vents over the resonator can be challenging.

Of the two approaches, the former was prototyped. However, a major failure mode was discovered. The “epi-seal” of the additional vents resulted in redeposition of silicon on top of the composite resonator and mechanical shorting of the resonator to the surrounding structures (Figure 7.3). The “epi-seal” process is optimized to be selective to silicon dioxide when the majority of the exposed area is silicon. However, inside the oxidized resonator cavity, the selectivity of the “epi-seal” process was not sufficient. One way to address this problem is to provide an effective getter. During the plasma etch of the top surface silicon dioxide, just prior to “epi-seal,” if an over-etch is performed, the silicon dioxide under the additional vents in the resonator cavity will be removed. The removal of silicon dioxide was previously undesirable for vents placed over the resonator electrodes. However, in this process, the exposed silicon surfaces would act as a getter and could result in growth of silicon in the getter instead of on the surface of the resonator.

One of the major advantages of this process modification is that silicon-only resonators and composite resonators could be fabricated on the same wafer simply by choice of where the additional vents are included.

7.1.3 Characterization

One of the biggest challenges in characterization of composite resonators is the uncertainty of the dimensions of the silicon and silicon dioxide portions of the beam. Although encapsulation provides a clean hermetic environment for testing the resonator, it obscures the visual inspection of the device tested. Unfortunately there is no non-destructive way of gaining visual access to the resonator. One possible approach is to use focused ion beam (FIB) technology to remove the encapsulation. This is a very time consuming method, but could be used to get a visual inspection. One of the biggest advantages in reducing dimensional uncertainty will be the ability to extract the temperature coefficients of silicon dioxide.

The extraction of material properties might be best achieved by design of resonators that are not flexural mode. The TCf of composite flexural mode resonators is preferentially sensitive to the dimension in the direction of vibration due to the

dependence on the 2nd moment of inertia of the beam. The TCf of a composite extensional resonator depends on the cross sectional area of each material portion, thus being less sensitive to width variations. The extraction of material properties might be best achieved by using extensional mode resonators. In particular, using extensional mode bar resonators would simplify the analysis compared to ring resonators due to the anisotropic properties of silicon.

7.2 Impact

Passive temperature compensation using composite silicon - silicon dioxide structures provides a new starting point for subsequent improvements in frequency-temperature stability using active temperature compensation. This passive technology can be readily integrated with the active compensation techniques described in Chapter 1. This section overviews the recent progress in the development of high stability silicon frequency references which have been enabled by the the composite technology and rival the stability provided by oven-controlled (OCXO) and temperature-compensated (TCXO) crystal oscillators.

Lee et al. [56] recently demonstrated the use of electrostatic active compensation using an ideally compensated composite double-ended tuning fork with a turnover temperature at 85 °C. The frequency of the resonator was calibrated over temperature and bias voltage. Using a platinum RTD temperature sensor and a look-up table built from the calibration, the frequency was compensated to within ± 3 ppm over a 70 °C temperature range by varying the bias voltage applied to the resonator in accordance to the look-up table. The compensation was achieved with approximately 5% change in the applied bias voltage. Although electrostatic compensation has been previously applied to compensate silicon resonators [33], the large temperature sensitivity of silicon required a large variation in the compensating bias voltage and a small electrostatic gap to tune the resonators frequency over a similar temperature range.

Hopcroft et al. [35] demonstrated an integrated oven-control system incorporating an ideally compensated double-ended tuning fork resonator suspended from a micro-machined resistive heating structure (Figure 7.4). The resonator exhibited a turnover temperature at approximately 82 °C. By applying a potential difference across the resistive element, the resonator could be heated to the turnover temperature regardless of the surrounding temperature. Hopcroft et al. [35] used the amplitude of the resonator's output signal, which is a measure of quality factor of the resonator, as an indicator of temperature and could maintain the temperature of the resonator to within 0.004 °C of the turnover temperature using active feedback control. The resulting frequency variation was approximately ± 0.01 ppm over a 10 °C to 70 °C external temperature variation. By using an integrated resistive heater, this micro-oven consumed approximately 25 mW, a significant reduction compared to OCXO's which consume Watts of power. A similar approach applied to silicon resonators yielded a ± 1 ppm variation over a -55 °C to 85 °C temperature variation due to the higher temperature sensitivity of silicon resonators. However, one of the limitations of using the resonator's output amplitude as a temperature sensor is that variation in the electronic components of the oscillator result in fluctuation in the amplitude of the resonator [78]. These fluctuations are incorrectly interpreted as temperature changes in the feedback control and result in frequency error. A better thermometry system is therefore needed to practically attain high frequency stability.

One of the more recent advances in quartz crystal temperature compensation is the use of two different modes of the quartz crystal which exhibit different temperature coefficients of frequency [91, 88]. The two frequencies are mixed to obtain a beat frequency with a larger sensitivity to temperature changes. The beat frequency can be used as an internal temperature sensor. The major benefits of this architecture are that there is no error associated with temperature gradients between sensor and resonator and a measurement of the frequency can be accurately performed. This type of system can also be implemented using composite resonators since it is possible to design composite resonators on the same die which have very different TCF's. Jha et al. [44] demonstrated a dual resonator system in which two double-ended tuning

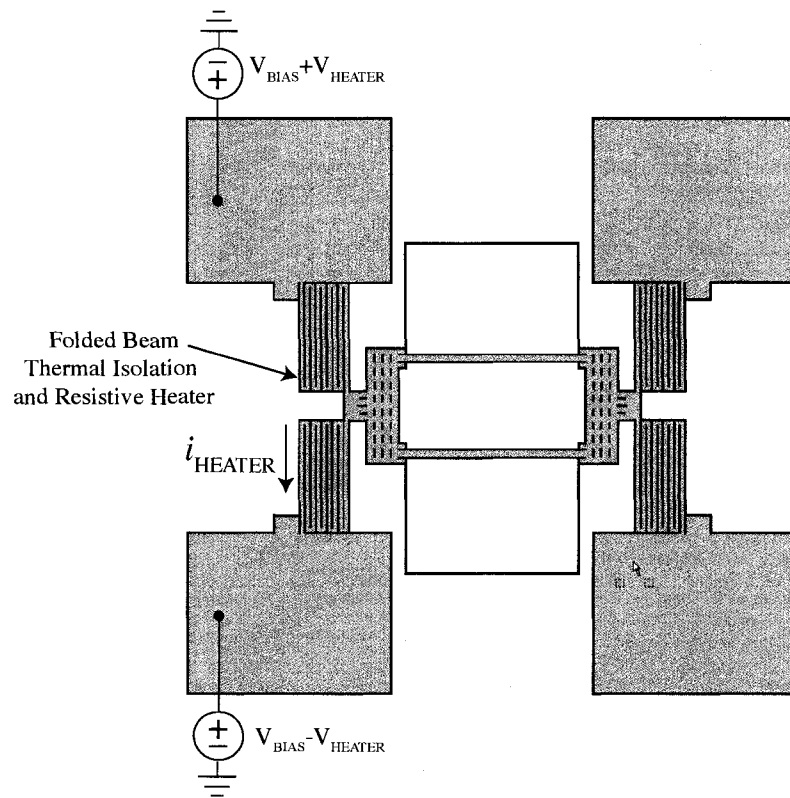


Figure 7.4: A DETF resonator is suspended using a folded beam structure which provides thermal isolation and can be used as a resistive heater. When a potential difference is applied across the folded beam, the resonator is resistively heated to a desired temperature.

fork resonators with different beam widths but the same silicon dioxide coatings were fabricated on the same die. The resonators were designed such that one was ideally compensated while the second had a TCf of -17 ppm/ $^{\circ}\text{C}$. Using the beat frequency technique, Jha demonstrated that the dual resonator system can be used as a temperature sensor with a resolution of better than 0.01 $^{\circ}\text{C}$.

Salvia et al. [77] recently demonstrated a system-level solution incorporating composite dual resonators suspended from a thermal isolation / resistive heater structure and temperature compensated using a real-time controller. The temperature compensation was implemented via a phase-lock loop controller which uses the beat frequency of the resonators as a temperature sensitive signal and locks the frequency

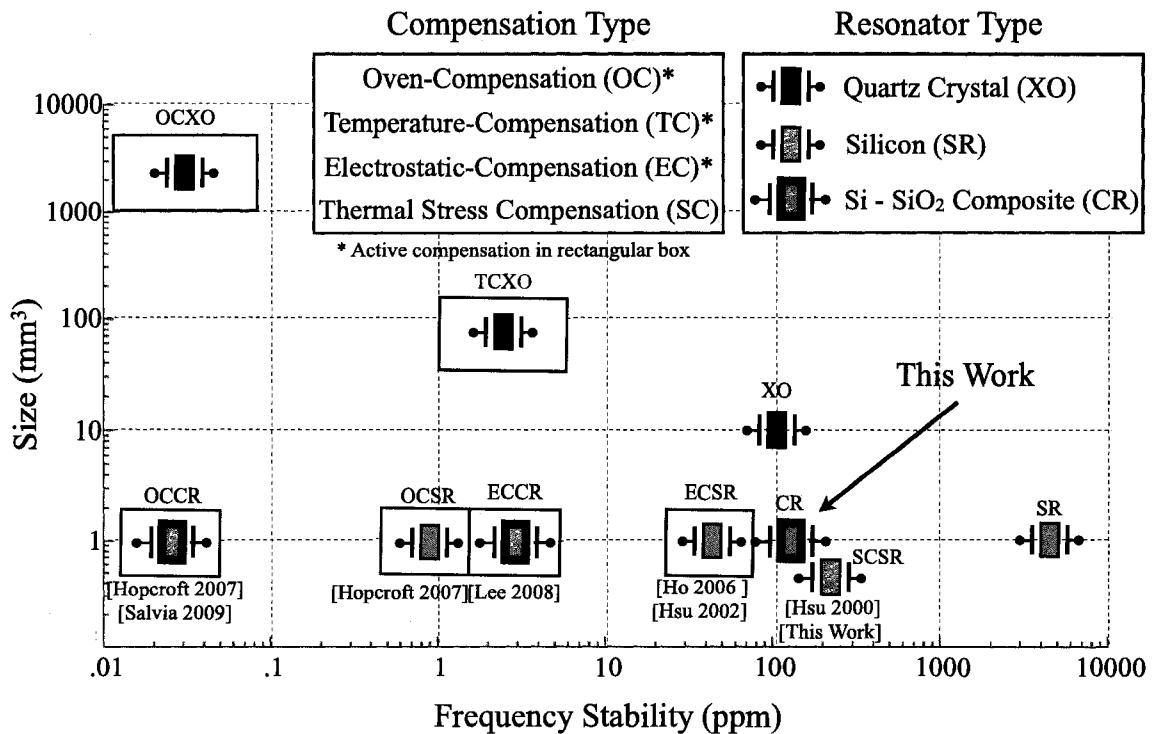


Figure 7.5: Progress in active and passive compensation of silicon resonators. Development of temperature-insensitive composite resonators allows a new starting point for achieving ultra-high frequency stability.

of one of the resonators by resistively heating the dual resonators. A total frequency variation of ± 0.05 ppm was achieved over a -20 °C to 80 °C temperature variation. The controller, which was implemented on a PCB, and the micro-oven consumed less than 150 mW. It is believed that an IC implementation of the controller and the micro-oven will limit power consumption to approximately 20 mW [77].

Figure 7.5 visually represents size and temperature stability of quartz, silicon, and composite resonators, actively compensated and not compensated.

Appendix A

Solution to Equation of Motion with Electrostatics

In Chapter 1, Section 1.2.2 the equation of motion for the vibration of a beam was derived. The nonlinear nature of the electrostatic forces results in a component of the force which is displacement dependent. This effect can be modeled as an electrostatic spring, k_e . Ignoring higher order terms, the homogeneous equation of motion was found to be:

$$\rho A \frac{\partial^2 v}{\partial t^2} + B \frac{\partial^4 v}{\partial x^4} - \frac{k_e}{L} v = 0 \quad (\text{A.1})$$

Using the method of separation of variables, the effective displacement of the beam, v , is separated into a displacement dependent equation, X , and time dependant equation, T .

$$v(x, t) = XT \quad (\text{A.2})$$

Substituting equation A.2 into A.1 and rewriting to obtain separable equations:

$$BX''''T - \frac{k_e}{L}XT = -\rho AXT'' \quad (\text{A.3})$$

$$\frac{B}{\rho A} \frac{X''''}{X} - \frac{k_e}{\rho AL} = -\frac{T''}{T} = \omega^2 \quad (\text{A.4})$$

Maintaining equality between the separable equations is only possible if both are equal to a constant. A convenient choice of a constant is ω^2 . Two ordinary differential equations are then obtained:

$$X'''' - \frac{\rho A}{B} \left(\omega^2 + \frac{k_e}{m} \right) X = 0 \quad (\text{A.5})$$

$$T'' + \omega^2 T = 0 \quad (\text{A.6})$$

Rewriting equation A.5 in terms of the eigenvalue λ :

$$\lambda^4 = \frac{\rho A}{B} \left(\omega^2 + \frac{k_e}{m} \right) \quad (\text{A.7})$$

$$X'''' - \lambda^4 X = 0 \quad (\text{A.8})$$

The solution to equation A.8 can be found in many books on vibration of continuous structures [76]. For boundary conditions consistent with a clamped-clamped beam, non-trivial solutions are found when:

$$\lambda L = \beta = 4.73 \quad (\text{A.9})$$

Rewriting equation A.7

$$\omega^2 = \lambda^4 \frac{B}{\rho A} - \frac{k_e}{m} \quad (\text{A.10})$$

$$\omega^2 = \frac{\beta^4}{L^4} \frac{B}{\rho A} - \frac{k_e}{m} \quad (\text{A.11})$$

The natural frequency without the addition of the electrostatic stiffness, ω_n , can also be found in most vibration books:

$$\omega_n^2 = \frac{\beta^4 B}{L^4 \rho A} \quad (\text{A.12})$$

Rewriting equation A.11 in terms of the natural frequency:

$$\omega^2 = \omega_n^2 - \frac{k_e}{m} \quad (\text{A.13})$$

$$\omega^2 = \omega_n^2 \left(1 - \frac{k_e}{m\omega_n^2} \right) \quad (\text{A.14})$$

$$(\text{A.15})$$

The resulting frequency of the resonator, including the linear effects of the electrostatic force is given in equation A.16. Since the electrostatic stiffness is a positive valued constant, the effect of the electrostatic force is to reduce the frequency of vibration.

$$f = f_n \sqrt{1 - \frac{k_e}{(2\pi)^2 m f_n^2}} \quad (\text{A.16})$$

Appendix B

Anisotropic Young's Modulus of Silicon

Silicon is an elastically anisotropic material. The Young's Modulus, which relates uniaxial stress and strain, will change depending on the direction relative to the crystal's material frame. For cubic materials, such as silicon, there exists a simple analytical expression for the direction dependent Young's Modulus [24]:

$$\frac{1}{E_{[hkl]}} = S_{11} - 2(S_{11} - S_{12} - \frac{1}{2}S_{44})(\alpha^2\beta^2 + \alpha^2\gamma^2 + \beta^2\gamma^2) \quad (\text{B.1})$$

In equation B.1, $E_{[hkl]}$ is the Young's Modulus in the direction given by the $[hkl]$ Miller indices which represent the direction through the crystal. S_{11} , S_{12} , and S_{44} are the compliance coefficients relating stresses to strains. α, β, γ are the direction cosines relative to the direction of interest through the crystal (Figure B.1):

$$\alpha = \cos(\theta_\alpha) \quad (\text{B.2})$$

$$\beta = \cos(\theta_\beta) \quad (\text{B.3})$$

$$\gamma = \cos(\theta_\gamma) \quad (\text{B.4})$$

For loads applied in the $\langle 100 \rangle$ group of directions, the Young's Modulus in

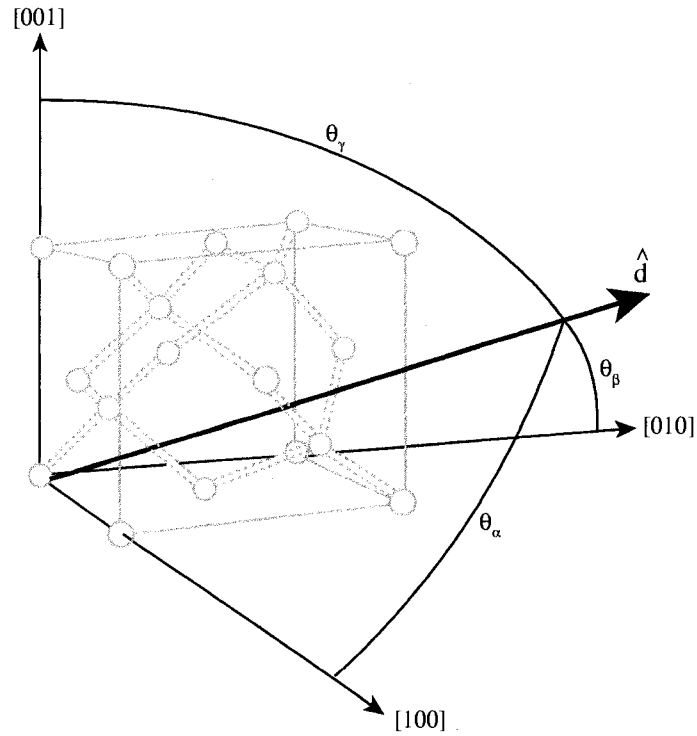


Figure B.1: For a given direction through the crystal, the direction cosines are defined relative to the material's frame of reference

equation B.1 simplifies to:

$$E_{\langle 100 \rangle} = \frac{1}{S_{11}} \quad (\text{B.5})$$

Taking the temperature derivative of equation B.1, the linear temperature coefficient of Young's Modulus is defined as:

$$TCE_{1,[hkl]} = E_{[hkl]} \left(TCS_{1,11} S_{11} - 2(TCS_{1,11} S_{11} - TCS_{1,12} S_{12} - \frac{1}{2} TCS_{1,44} S_{44}) (\alpha^2 \beta^2 + \alpha^2 \gamma^2 + \beta^2 \gamma^2) \right) \quad (\text{B.6})$$

The quadratic temperature coefficient of Young's Modulus, $TCE_{2,[hkl]}$, can also

Elastic		Temperature Coefficients			
Constants ($\times 10^{-12}$)		Linear (ppm/ $^{\circ}\text{C}$)		Quadratic (ppb/ $^{\circ}\text{C}^2$)	
S_{11}	7.69	$\text{TCS}_{1,11}$	63.6	$\text{TCS}_{2,11}$	60.51
S_{12}	-2.14	$\text{TCS}_{1,12}$	45.79	$\text{TCS}_{2,12}$	75.70
S_{44}	12.58	$\text{TCS}_{1,44}$	57.96	$\text{TCS}_{2,44}$	57.31

Table B.1: Compliance Coefficients of Single Crystal Silicon Bourgeois et al. [16]

Direction	E (GPa)	TCE_1 (ppm/ $^{\circ}\text{C}$)	TCE_2 (ppb/ $^{\circ}\text{C}^2$)
[100]	130.0	-63.60	-56.47
[110]	168.9	-63.82	-51.99

Table B.2: Young's Modulus and it's temperature coefficients in the [100] and [110] directions Bourgeois et al. [16]

be determined. However, it is analytically complex and is best determined computationally.

Silicon MEMS devices are predominately manufactured using single-crystal silicon wafers with a [001] normal. The directions of interest in the plane of the wafer have $\gamma = 0$. The Young's Modulus in the plane of the [100] wafer can be written by simplifying equation B.1 and rewriting in terms of a single angle dependence, θ_α :

$$\frac{1}{E_\theta} = S_{11} - 2(S_{11} - S_{12} - \frac{1}{2}S_{44}) \frac{\sin(2\theta_\alpha)}{4} \quad (\text{B.7})$$

Table B.1 shows the compliance coefficients and their linear and quadratic temperature coefficients taken from Bourgeois et al. [16]. Figure B.2 is a plot of the direction dependent Young's Modulus, linear temperature coefficient of Young's Modulus, and quadratic temperature coefficient of Young's Modulus normalized to their respective values in the [100] direction (Table B.2). The flexural mode double-ended tuning fork resonators demonstrated in this dissertation are predominately oriented in the [110] direction. These values are also given in Table B.2.

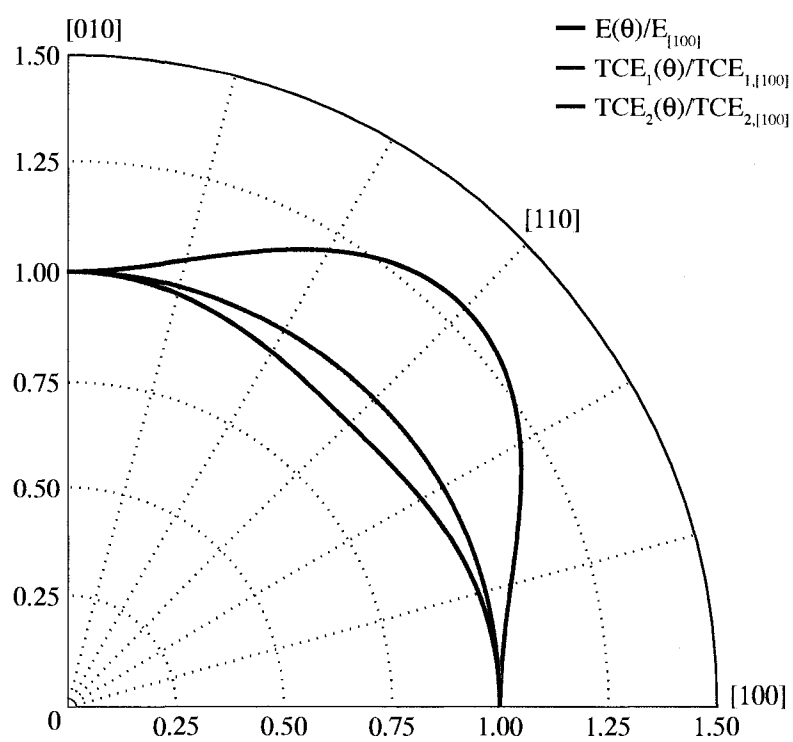


Figure B.2: Direction dependent Young's Modulus, TCE_1 , and TCE_2 of Silicon normalized to their respective [100] values found in Table B.2

Appendix C

Positive TCE of Silicon Dioxide

The earliest studies of the temperature dependent properties of amorphous silicon-dioxide were in 1890 when Threlfall [27] observed that that the shear modulus of a fused silica rod would increase as the rod was heated. A more accurate investigation into the Young's Modulus of fused quartz was performed by Drane [27] in 1929. Drane used the end displacement of a fused quartz cantilever under varying temperature conditions to extract the Young's Modulus. At 25 °C Drane measured the TCE of fused quartz to be approximately 163 ppm/°C. In 1953, McSkimin et al. [64] measured the Young's Modulus of a fused silica rod using ultrasonic wave propagation. Unfortunately, only plots of the data are published. Extraction of the data using software DataThief [86], indicates a TCE of 185 ppm/°C. In 1960, Spinner and Cleek [83] measured the flexural mode frequency of a fused silica bar to extract the TCE. The publication also indicates that the quadratic temperature coefficient of Young's Modulus is negative. Unfortunately values for the material properties are only provided in plot form. Extraction of the TCE from the plots indicates a TCE of 192 ppm/°C. More recently, Kushibiki et al. [53] reported on the effect of OH ion content on the temperature coefficient of longitudinal velocity of various bulk samples of glass. A higher temperature coefficient of velocity was attributed to a higher OH content. The temperature coefficient of Young's Modulus could not be extracted since only the temperature dependence of longitudinal velocity was reported.

One of the first measurements of the temperature dependent material properties

of thin film SiO₂ was reported by Faouzi et al. [29] in 1985 on sputtered SiO₂. The properties were extracted from the temperature coefficient of phase delay in a surface acoustic device. The extracted temperature coefficient of Young's Modulus is approximately 125 ppm/°C. One of the only measurements of the temperature coefficient of Young's Modulus of thermally grown SiO₂ was performed by Sandberg et al. [79]. A TCE of 195.8 ppm/°C was extracted from frequency measurements of a cantilever micromachined from a thermally grown layer of SiO₂.

Although the anomalous behaviour of silicon dioxide has been observed for over a century, determining the cause is an ongoing exploration. Anderson et al. [5] provides one of the earliest explanations, which links the positive temperature coefficient of Young's Modulus to having a extremely low coefficient of thermal expansion. Using the assumptions of a Born-von Karman solid to model a crystal, the temperature dependence of modulus is given as partial derivatives with regard to temperature, T , and volume, V :

$$\frac{\partial M}{\partial T} = \alpha V \left(\frac{\partial M}{\partial V} \right)_T + \left(\frac{\partial M}{\partial T} \right)_V \quad (\text{C.1})$$

For small coefficients of thermal expansion, α , the left term to the right side of the equal sign in equation C.1 becomes insignificant, and the temperature dependence of modulus is dominated by the the temperature dependence of modulus at constant volume [17]. For small coefficients of thermal expansion and moderate to high temperatures, Anderson et al. [5] showed that the temperature dependence of modulus is positive.

More recently, the anomaly has been studied using molecular dynamics simulations. Structural analogies between cristobalite, a crystalline form of SiO₂, and amorphous SiO₂ are made. Molecular dynamics simulations indicate that the rotation of the Si-O-Si planes could result in a stiffer structures [42, 43]. Cristobalite is known to be a structural polymorph exhibiting one form at low temperatures, α -cristobalite, and another form at high temperatures, β -cristobalite. Molecular dynamics simulations indicate that a sharp transition occurs between these two states and that the structure at high temperatures leads to a larger Young's Modulus. Unfortunately,

the Young's Modulus of β -cristobalite has not been measured as the structure becomes unstable at high temperatures where the transition occurs. Le Parc et al. [55] provides a good overview of the study of anomalous behavior in silicon dioxide.

In amorphous silicon dioxide, the transformation to a stiffer structures happens gradually over temperature. Researchers have begun to characterize amorphous silicon dioxide as a polyamorph - an amorphous material with different short order structures at low and high temperature [41]. Youngman et al. [96] argues that the rotation of the bond angles occurs without breaking of chemical bonds.

The rotation of the bond angle of the tetrahedral structure of silicon dioxide is also common to germanium dioxide. Measurements of the Young's Modulus of germanium dioxide show a positive temperature coefficient of Young's Modulus as well [83].

Bibliography

- [1] Abdelmoneum, M. A., Demirci, M. U., and Nguyen, C. T. C. (2003). “Stemless wine-glass-mode disk micromechanical resonators.” In “Micro Electro Mechanical Systems, 2003. MEMS-03 Kyoto. IEEE The Sixteenth Annual International Conference on,” pages 698–701.
- [2] Afanas’ev, V. V. and Stesmans, A. (1998). “Positive charging of thermal SiO₂/Si interface by hydrogen annealing.” *APPLIED PHYSICS LETTERS*, 72: 79–81.
- [3] Agarwal, M., Chandorkar, S. A., Candler, R. N., Kim, B., Hopcroft, M. A., Melamud, R., Jha, C. M., Kenny, T. W., and Murmann, B. (2006). “Optimal drive condition for nonlinearity reduction in electrostatic microresonators.” *Applied Physics Letters*, 89(21): 214105–7.
- [4] Agarwal, M., Park, K. K., Chandorkar, S. A., Candler, R. N., Kim, B., Hopcroft, M. A., Melamud, R., Kenny, T. W., and Murmann, B. (2007). “Acceleration sensitivity in beam-type electrostatic microresonators.” *Applied Physics Letters*, 90(1): 014103–3.
- [5] Anderson, O. L., Dienes, G. J., and Frechette, V. D. (1960). *Non-Crystalline Solids*. Wiley, New York.
- [6] Bahl, G., Melamud, R., Kim, B., Chandorkar, S., Salvia, J., Hopcroft, M., R.G., H., Yoneoka, S., Jha, C., Yama, G., Elata, D., Candler, R. N., Howe, R. T., and Kenny, T. W. (2008). “Observation of fixed and mobile charge in composite MEMS resonators.” In “Hilton Head 2008, the

- IEEE Solid-State Sensor, Actuator and Microsystems Workshop," Transducers Research Foundation, Hilton Head, SC USA.
- [7] **Bartek, M., Gennissen, P. T. J., French, P. J., Sarro, P. M., and Wolfenbuttel, R. F. (1997).** "Study of selective and non-selective deposition of single-and polycrystalline silicon layers in an epitaxial reactor." In "Solid State Sensors and Actuators, 1997. TRANSDUCERS '97 Chicago., 1997 International Conference on," volume 2, pages 1403–1406 vol.2.
- [8] **Bechmann, R., Ballato, A. D., and Lukaszek, T. J. (1962).** "Higher-Order Temperature Coefficients of the Elastic Stiffness and Compliances of Alpha-Quartz." *Proceedings of the IRE*, 50: 1812–1822.
- [9] **Bhave, S. A. and Howe, R. T. (2004).** "INTERNAL ELECTROSTATIC TRANSDUCTION FOR BULK-MODE MEMS RESONATORS." In "Proc. Solid State Sensor, Actuator Microsyst. Workshop," .
- [10] **Bhave, S. A. and Howe, R. T. (2005).** "Silicon nitride-on-silicon bar resonator using internal electrostatic transduction." In "Solid-State Sensors, Actuators and Microsystems, 2005. Digest of Technical Papers. TRANSDUCERS '05. The 13th International Conference on," volume 2, pages 2139–2142 Vol. 2.
- [11] **Binder, D. S., Quevy, E., Koyama, T., Govindjee, S., Demmel, J. W., and Howe, R. T. (2005).** "Anchor loss simulation in resonators." In "Micro Electro Mechanical Systems, 2005. MEMS 2005. 18th IEEE International Conference on," pages 133–136.
- [12] **Blevins, R. D. (1979).** *Formulas for natural frequency and mode shape.* Van Nostrand Reinhold, New York.
- [13] **Bochobza-Degani, O., Elata, D., and Nemirovsky, Y. (2002).** "An efficient DIPIE algorithm for CAD of electrostatically actuated MEMS devices." *Microelectromechanical Systems, Journal of*, 11(5): 612–620.

- [14] **Bouchaud, J. and Knoblich, B. (2006).** "Has the time come for MEMS oscillators?" Newsletter, Wicht Technologie Consulting.
- [15] **Bourgeois, C., Hermann, J., Blanc, N., de Rooij, N., and Rudolf, F. (1995).** "Determination Of The Elastic Temperature Coefficients Of Monocrystalline Silicon." In "TRANSDUCERS '95 / Eurosensors IX, Solid-State Sensors and Actuators, 1995. The 8th International Conference on," volume 2, pages 92-95.
- [16] **Bourgeois, C., Steinsland, E., Blanc, N., and de Rooij, N. (1997).** "Design of resonators for the determination of the temperature coefficients of elastic constants of monocrystalline silicon." In "FCS '97, The 1997 IEEE International Frequency Control Symposium," pages 791-799.
- [17] **Bruckner, R. (1970).** "Properties and structure of vitreous silica. I." *J. Non-Cryst. Solids*, 5(2): 123175.
- [18] **Cambon, G., Adler, E. L., Attal, J., and Shahab, W. (1979).** "Temperature Effects on Acoustic Surface Wave Devices on Silicon." In "Ultrasonics Symposium," pages 637-640.
- [19] **Campbell, S. A. (1996).** *The science and engineering of microelectronic fabrication.* Oxford University Press, New York.
- [20] **Candler, R. N. (2006).** *Thermoelastic Dissipation in Silicon Micromechanical Resonators.* Phd, Stanford University.
- [21] **Candler, R. N., Duwel, A., Varghese, M., Chandorkar, S. A., Hopcroft, M. A., Park, W.-T., Bongsang, K., Yama, G., Partridge, A., Lutz, M., and Kenny, T. W. (2006).** "Impact of geometry on thermoelastic dissipation in micromechanical resonant beams." *Journal of Microelectromechanical Systems*, 15(4): 927-934.
- [22] **Candler, R. N., Hopcroft, M. A., Kim, B., Park, W. T., Melamud, R., Agarwal, M., Yama, G., Partridge, A., Lutz, M., and Kenny, T. W.**

- (2006). "Long-Term and Accelerated Life Testing of a Novel Single-Wafer Vacuum Encapsulation for MEMS Resonators." *Journal of Microelectromechanical Systems*, 15(6): 1446–1456.
- [23] Chandorkar, S., Mehta, H., Agarwal, M., Hopcroft, M. A., Jha, C. M., Candler, R. N., Yama, G., Bahl, G., Kim, B., Melamud, R., Goodson, K. E., and Kenny, T. W. (2007). "Non-Isothermal Micromechanical Resonators." In "MEMS 2007, The 20th IEEE International Conference on Micro Electro Mechanical Systems," volume 1. IEEE, Kobe, Japan.
- [24] Courtney, T. H. and Hugh, T. (2000). *Mechanical behavior of materials*. McGraw-Hill New York.
- [25] Discera (2008). URL www.discera.com.
- [26] Doerner, M. F. and Nix, W. D. (1988). "Stresses and deformation processes in thin films on substrates." *Critical Reviews in Solid State and Materials Sciences*, 14(3): 225–268.
- [27] Drane, H. (1928). "Elastic constants of fused quartz - Change of Youngs modules with temperature." *Proceedings of the Royal Society of London. Series A*, 122(789): 274–282.
- [28] Epson (2007). "Epson Toyocom Develops World's Smallest Tuning-Fork Crystal Unit."
- [29] Faouzi, N., Saurel, J. M., Lassale, J., and Cambon, G. (1985). "Temperature Coefficients of the Elastic Constants of SiO₂ Layers." *Sonics and Ultrasonics, IEEE Transactions on*, 32(4): 596–599.
- [30] Flinn, P. A., Gardner, D. S., and Nix, W. D. (1987). "Measurement and Interpretation of stress in aluminum-based metallization as a function of thermal history." *Electron Devices, IEEE Transactions on*, 34(3): 689–699.

- [31] **Frerking, M. E. (1996)**. "Fifty years of progress in quartz crystal frequency standards." In "Frequency Control Symposium, 1996. 50th., Proceedings of the 1996 IEEE International.", pages 33–46.
- [32] **Freund, L. B. and Suresh, S. (2003)**. *Thin Film Materials: Stress, Defect Formation, and Surface Evolution*. Cambridge University Press.
- [33] **Ho, G. K., Sundaresan, K., Pourkamali, S., and Ayazi, F. (2006)**. "Temperature compensated IBAR reference oscillators." In "MEMS 2006, the 19th IEEE International Conference on Micro Electro Mechanical Systems," Istanbul, Turkey.
- [34] **Hopcroft, M. (2007)**. *Temperature-stabilized silicon resonators for frequency references*. Phd, Stanford University.
- [35] **Hopcroft, M. A., Agarwal, M., Park, K. K., Kim, B., Jha, C. M., Candler, R. N., Melamud, R., Yama, G., Murmann, B., and Kenny, T. W. (2006)**. "Temperature compensation of a MEMS resonator using Quality Factor as a thermometer." In "MEMS 2006, The 19th IEEE International Conference on Micro Electro Mechanical Systems," Istanbul, Turkey.
- [36] **Hopcroft, M. A., Kim, B., Chandorkar, S., Melamud, R., Agarwal, M., Jha, C. M., Bahl, G., Salvia, J., Mehta, H., Lee, H. K., Candler, R. N., and Kenny, T. W. (2007)**. "Using the temperature dependence of resonator quality factor as a thermometer." *Applied Physics Letters*, 91(1): 013505–3.
- [37] **Hopcroft, M. A., Melamud, R., Candler, R. N., Park, W.-T., Kim, B., Yama, G., Partridge, A., Lutz, M., and Kenny, T. W. (2004)**. "Active Temperature Compensation for Micromechanical Resonators." In "Hilton Head 2004, the IEEE Solid-State Sensor, Actuator and Microsystems Workshop," pages 364–367. Transducers Research Foundation, Hilton Head, SC USA.
- [38] **Howe, R. (1986)**. "POLYCRYSTALLINE SILICON MICROMACHINING - A NEW TECHNOLOGY FOR INTEGRATED SENSORS." *Annals of biomedical engineering*, 14(2): 187–197.

- [39] Hsu, W.-T., Clark, J., and Nguyen, C.-C. (2000). "Mechanically temperature-compensated flexural-mode micromechanical resonators." In "Electron Devices Meeting, 2000. IEDM Technical Digest. International," pages 399–402.
- [40] Hsu, W.-T. and Nguyen, C.-C. (2002). "Stiffness-compensated temperature-insensitive micromechanical resonators." In "MEMS 2002, The 15th IEEE International Conference on Micro Electro Mechanical Systems," pages 731–734. IEEE, Las Vegas, NV USA.
- [41] Huang, L., Duffrue, L., and Kieffer, J. (2004). "Structural transitions in silica glass: thermo-mechanical anomalies and polyamorphism." *Journal of Non-Crystalline Solids*, 349: 1–9.
- [42] Huang, L. and Kieffer, J. (2004). "Amorphous-amorphous transitions in silica glass. I. Reversible transitions and thermomechanical anomalies." *Physical Review B*, 69(22): 224 203.
- [43] Huang, L. and Kieffer, J. (2004). "Amorphous-amorphous transitions in silica glass. II. Irreversible transitions and densification limit." *Physical Review B*, 69(22): 224 204.
- [44] Jha, C. M., Bahl, G., Melamud, R., Chandorkar, S. A., Hopcroft, M. A., Kim, B., Agarwal, M., Salvia, J., Mehta, H., and Kenny, T. W. (2007). "High resolution microresonator-based digital temperature sensor." *Applied Physics Letters*, 91(7): 074 101–3.
- [45] Johnson, R. (2006). "MEMS best-practice definition varies by vendor."
- [46] Kaajakari, V., Kiihamaki, J., Oja, A., Pietikainen, S., Kokkala, V., and Kuisma, H. (2006). "Stability of wafer level vacuum encapsulated single-crystal silicon resonators." *Sensors and Actuators A: Physical*, 130-131: 42–47.
- [47] Kaajakari, V., Mattila, T., Oja, A., and Seppa, H. (2004). "Nonlinear limits for single-crystal silicon microresonators." *Journal of Microelectromechanical Systems*, 13(5): 715–724.

- [48] **Kamins, T. I. (1998).** *Polycrystalline Silicon for Integrated Circuits and Displays*. Kluwer Academic Publishers.
- [49] **Kim, B. (In Press).** “Hermeticity and Diffusion Investigation in Polysilicon Film Encapsulation for Microelectromechanical Systems (MEMS).” *Journal of Applied Physics*.
- [50] **Kim, B., Candler, R. N., Hopcroft, M. A., Agarwal, M., Park, W.-T., and Kenny, T. W. (2007).** “Frequency stability of wafer-scale film encapsulated silicon based MEMS resonators.” *Sensors and Actuators A: Physical*, 136: 125–131.
- [51] **Kim, B., Candler, R. N., Melamud, R., Yoneoka, S., Hyung Kyu, L., Yama, G., and Kenny, T. W. (2008).** “Identification and management of diffusion pathways in polysilicon encapsulation for MEMS devices.” In “Micro Electro Mechanical Systems, 2008. MEMS 2008. IEEE 21st International Conference on,” pages 104–107.
- [52] **Kim, B., Jha, C. M., White, T., Candler, R. N., Hopcroft, M. A., Agarwal, M., Park, K. K., Melamud, R., and Kenny, T. W. (2006).** “Temperature Dependence of Quality Factor in MEMS Resonators.” In “MEMS 2006, The 19th IEEE International Conference on Micro Electro Mechanical Systems,” Istanbul, Turkey.
- [53] **Kushibiki, J., Wei, T., Ohashi, Y., and Tada, A. (2000).** “Ultrasonic microspectroscopy characterization of silica glass.” *Journal of Applied Physics*, 87(6): 3113–21.
- [54] **Lawrence, R. K., Hughes, H. L., Stahlbush, R. E., Ma, D. I., Twigg, M. E., and Aracor, S. (1997).** “BOX quality as measured by hydrogen-anneal-induced positive charge transport.” In “IEEE International SOI Conference Proceedings 1997,” pages 142–143.
- [55] **Le Parc, R., Levelut, C., Pelous, J., Martinez, V., and Champagnon, B. (2006).** “Influence of fictive temperature and composition of silica glass on

- anomalous elastic behaviour." *Journal of Physics, Condensed Matter*, 18(32): 7507–7527.
- [56] Lee, H., Hopcroft, M., Melamud, R., Kim, B., Salvia, J., Chandorkar, S., and Kenny, T. W. (2008). "Electrostatic-Tuning of Hermetically Encapsulated Composite Resonator." In "Hilton Head 2008, the IEEE Solid-State Sensor, Actuator and Microsystems Workshop," Transducers Research Foundation, Hilton Head, SC USA.
- [57] Lee, J. S. and Lee, W. G. (2004). "Generation of Oxide Fixed Charge in Thin Gate Oxide Incorporated with Hydrogen/Deuterium during Negative-Bias Temperature Instability Stress." *JOURNAL-KOREAN PHYSICAL SOCIETY*, 45(2): 1224–1228.
- [58] Lee, S. and Nguyen, C. T. C. (2003). "Influence of automatic level control on micromechanical resonator oscillator phase noise." In "Frequency control symposium and pda exhibition jointly with the 17th european frequency and time forum, 2003. proceedings of the 2003 ieee international," pages 341–349.
- [59] Lee, T. H. (2004). *The Design of CMOS Radio-Frequency Integrated Circuits*. Cambridge University Press.
- [60] Li, S. S., Yu-Wei, L., Yuan, X., Zeying, R., and Nguyen, C. T. C. (2004). "Micromechanical "hollow-disk" ring resonators." In "Micro Electro Mechanical Systems, 2004. 17th IEEE International Conference on. (MEMS)," pages 821–824.
- [61] Lynun, B. and Torbin, C. (2000). "On temperature dependence of Young's Modulus of pure quartz glass."
- [62] Madou, M. J. (2001). *Fundamentals of Microfabrication*. CRC Press LLC, 2nd edition.
- [63] McSkimin, H. J. (1953). "Measurement of Elastic Constants at Low Temperatures by Means of Ultrasonic Waves—Data for Silicon and Germanium Single Crystals, and for Fused Silica." *Journal of Applied Physics*, 24(8): 988–997.

- [64] **McSkimin, H. J., Bond, W. L., Buehler, E., and Teal, G. K. (1951).** "Measurement of the Elastic Constants of Silicon Single Crystals and Their Thermal Coefficients." *Physical Review*, 83(5): 1080.
- [65] **Miyake, T. (2008).** "TSMC Announces Full-scale Entry into MEMS Market."
- [66] **NASA (2008).** "Tunable Environmental Laser Spectrometer."
- [67] **Newnham, R. (2006).** *Properties of Materials: Anisotropy, Symmetry, Structure*. Oxford University Press.
- [68] **Nguyen, C. (1994).** *Micromechanical Signal Processors*. Phd, University of California at Berkeley.
- [69] **Nguyen, C. T. C. (2007).** "MEMS technology for timing and frequency control." *IEEE Transactions on Ultrasonics, Ferroelectrics and Frequency Control*, 54(2): 251-270.
- [70] **Nix, W. D. (1989).** "Mechanical properties of thin films." *Metallurgical and Materials Transactions A*, 20(11): 2217-2245.
- [71] **Pang, W., Yu, H., Zhang, H., and Kim, E. S. (2005).** "Temperature-compensated film bulk acoustic resonator above 2 GHz." *Electron Device Letters*, 26(6): 369-371.
- [72] **Park, Y.-H. and Park, K. C. (2004).** "High-fidelity modeling of MEMS resonators. Part I. Anchor loss mechanisms through substrate." *Journal of Microelectromechanical Systems*, 13(2): 238-247.
- [73] **Parker, T. E. and Schulz, M. B. (1974).** "Temperature Stable Surface Acoustic Wave Delay Lines with SiO₂ Film Overlays." In "Ultrasonics Symposium 1974," pages 295-298.
- [74] **Petersen, K. (1982).** "Silicon as a Mechanical Material." *Proceedings of the IEEE*, 70(5): 420-457.

- [75] **Plummer, J., Deal, M., and Griffin, P. (2000).** *Silicon VLSI Technology: Fundamentals, Practice, and Modeling.* Prentice Hall.
- [76] **Rao, S. (2007).** *Vibration of Continuous Systems.* John Wiley and Sons, Inc., Hoboken, New Jersey.
- [77] **Salvia, J., Melamud, R., Chandorkar, S., Lee, H., Qu, Y., Lord, S., Murmann, B., and Kenny, T. W. (2009).** "A Phase Lock Loop Based Temperature Compensation System for MEMS Oscillators." In "MEMS 2009, The 20th IEEE International Conference on Micro Electro Mechanical Systems," Sorrento, Italy.
- [78] **Salvia, J., Messina, M., Ohline, M., Hopcroft, M. A., Melamud, R., Chandorkar, S., Lee, H., Murmann, B., and Kenny, T. W. (2008).** "Exploring the Limits and Practicality of Q-based Temperature Compensation for Silicon Resonators." In "IEEE International Electron Devices Meeting," IEEE.
- [79] **Sandberg, R., Svendsen, W., Mlhave, K., and Boisen, A. (2005).** "Temperature and pressure dependence of resonance in multi-layer microcantilevers." *Journal of Micromechanics and Microengineering*, 15(8): 1454–1458.
- [80] **Sassella, A., Borghesi, A., Corni, F., Monelli, A., Ottaviani, G., Tonini, R., Pivac, B., Bacchetta, M., and Zanotti, L. (1997).** "Infrared study of Si-rich silicon oxide films deposited by plasma-enhanced chemical vapor deposition." *Journal of Vacuum Science and Technology A: Vacuum, Surfaces, and Films*, 15: 377.
- [81] **Shen, F., Lu, P., O'Shea, S. J., Lee, K. H., and Ng, T. Y. (2001).** "Thermal effects on coated resonant microcantilevers." *Sensors and Actuators A: Physical*, 95(1): 17–23.
- [82] **SiTime (2008).** URL www.sitime.com.

- [83] **Spinner, S. and Cleek, G. W. (1960)**. "Temperature Dependence of Young's Modulus of Vitreous Germania and Silica." *Journal of Applied Physics*, 31(8): 1407-1410.
- [84] **Swisstime (2007)**. "Swisstime Trendline FO7."
- [85] **Thompson, C. V. and Carel, R. (1996)**. "Stress and grain growth in thin films." *Journal of the Mechanics and Physics of Solids*, 44(5): 657-673.
- [86] **Tummers, B. (2006)**. "DataThief III."
- [87] **Vig, J. R. (1977)**. "Resonator Aging." In "Ultrasonics Symposium," pages 848-850. IEEE.
- [88] **Vig, J. R. (2001)**. "Temperature-Insensitive Dual-Mode Resonant Sensors - a Review." *IEEE Sensors Journal*, 1(1): 62-68.
- [89] **Vig, J. R. (2005)**. "Quartz Crystal Resonators and Oscillators for Frequency Control and Timing Applications - A Tutorial." Powerpoint Presentation rev 8.5.3.0, US Army Communications-Electronics Research, Development and Engineering Center.
- [90] **Vig, J. R. and Ballato, A. (1999)**. "Frequency Control Devices." In E. P. Papadakis, editor, "Ultrasonic Instruments and Devices," pages 637-697. Academic Press.
- [91] **Vig, J. R., Command, U., and Monmouth, F. (1999)**. "Dual-mode oscillators for clocks and sensors." In "IEEE Proceedings of Ultrasonics Symposium," volume 2.
- [92] **Weinstein, D. and Bhave, S. A. (2007)**. "Internal dielectric transduction: optimal position and frequency scaling." *Ultrasonics, Ferroelectrics and Frequency Control, IEEE Transactions on*, 54(12): 2696-2698.
- [93] **Xie, Y., Li, S.-S., Lin, Z., Ren, Z., and Nguyen, C. T. C. (2008)**. "1.52-GHz Micromechanical Extensional Wine-Glass Mode Ring Resonators."

- Ultrasonics, Ferroelectrics and Frequency Control, IEEE Transactions on*, 55(4): 890–907.
- [94] Yasumura, K. Y., Stowe, T. D., Chow, E. M., Pfafman, T., Kenny, T. W., Stipe, B. C., and Rugar, D. (2000). “Quality factors in micron- and submicron-thick cantilevers.” *Journal of Microelectromechanical Systems*, 9(1): 117–125.
- [95] Young, W. C. (1989). *Roark’s Formulas for Stress and Strain*. McGraw-Hill, Inc., 6th edition.
- [96] Youngman, R. E., Kieffer, J., Bass, J. D., and Duffrene, L. (1997). “Extended structural integrity in network glasses and liquids.” *Journal of non-crystalline solids*, 222: 190–198.